FACULTY OF SCIENCE
UNIVERSITY OF COPENHAGEN

Master Thesis

Morten Ankersen Medici

Diffraction with ALFA and ATLAS at $\sqrt{s} = 8$ TeV

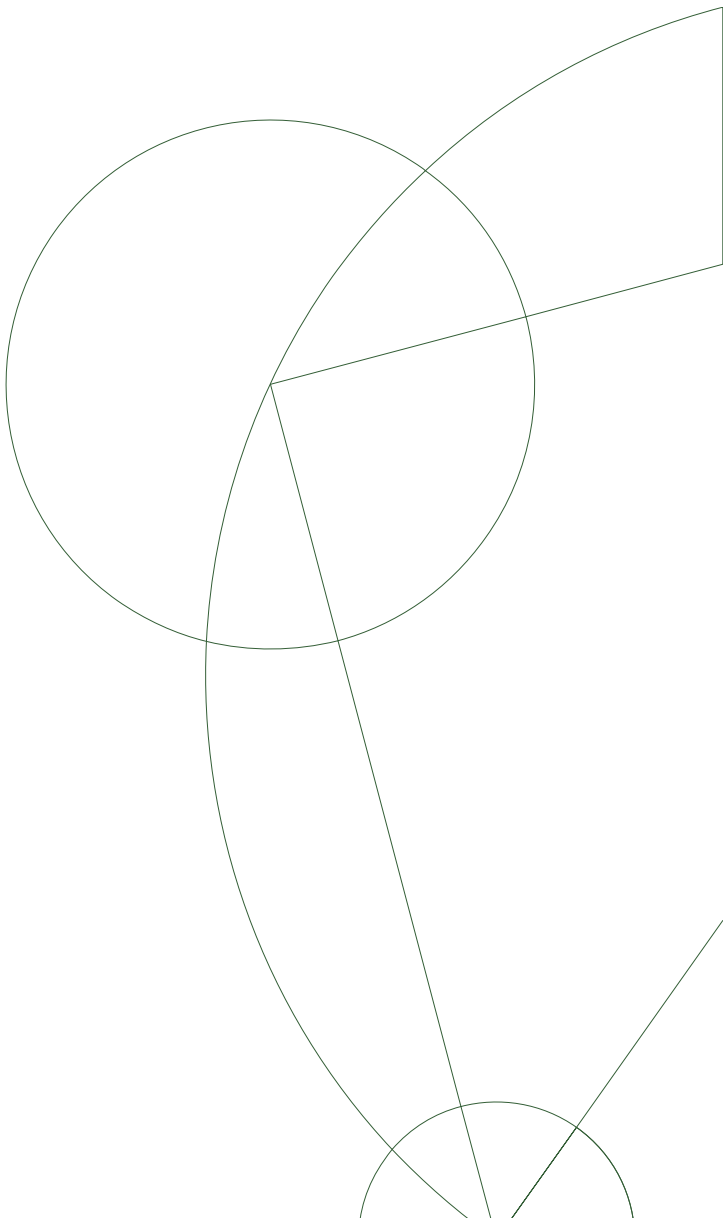

Academic supervision by Jørgen Beck Hansen

August 30th 2013

Abstract

In this thesis an investigation into diffractive scattering of high energy protons will be presented. A short review on the theoretical landscape describing diffraction in particle physics shall be introduced, before describing the experimental possibilities of ALFA, motivating the use of it for studies of diffractive processes. A thorough study of the trigger system of ALFA is performed, as well as a data driven investigation of the tracking of single diffractive scattered protons in ALFA. This serves as part of the initial steps for understanding the detector, in order to use the data produced by ALFA more confidently. The Minimum Bias Analysis at $\sqrt{s} = 8$ TeV in ATLAS is described, with emphasis on the author's contribution, as an introduction to the work done on soft processes. The charged track multiplicities discussed in minimum bias events shall serve as the reference for the initial studies on the general properties of single diffractive events considered at $\sqrt{s} = 8$ TeV. Steps are also taken towards determining the single diffractive cross section, investigating the difficulties which arise in such an analysis.

Resumé

I dette speciale er diffraktion af protoner i højenergiske collisioner blevet undersøgt. Den teoretiske beskrivelse af diffraktion i partikel fysik vil først blive gennemgået, hvorefter ATLAS og ALFA detektorene vil blive beskrevet. Herved skal brugen af disse detectorer til at undersøe diffraction motiveres. Et grundigt studie af trigger systemet i ALFA er foretaget, og sporingen af de diffraktivt spredte protoner i ALFA er undersøgt udelukkende ved brug af data. Dette er nødvendigt arbejde, der må udføres, for bedre at forstå det data som ALFA leverer. Minimum Bias Analysen ved $\sqrt{s} = 8$ TeV bliver gennemgået med fokus på forfatterens bidrag, og skal tjene som en introduktion til studier af de lav energiske processer. De studerede fordelinger af ladede spor i ATLAS giver en reference til lignende fordelinger i diffraktions processer, som vil blive diskuteret på et overordnet plan for begivenheder i $\sqrt{s} = 8$ TeV. Yderligere er en række skridt foretaget mod en bestemmelse af tværsnittet for single diffraktion.

Contents

Preface

Dear reader.

Thank you for picking up my thesis, turning the pages and taking your time to read this. When you are working on a project for a year, you tend to nurture it at a level you have not tried before, and it is difficult to determine when the project ends and where it begins.

As will soon be explained, only a few of the topics discussed in this thesis could be concluded within the scope of one year. As a new branch of the analysis of soft interactions in ATLAS, the diffractive analysis using ALFA involved a serious amount of testing, verification and validation of data and Monte Carlo samples, before even considering the approach to the analysis of diffraction. Combined with the work of Simon Stark Mortensen and Mikkel Skaarup, this thesis constitutes the initial steps of the diffractive analysis with ALFA. I am confident that we (with the help from many others) have laid the foundations for a lot of interesting future investigations.

This thesis has been written with a fellow master student of high energy physics in mind, and it should reflect the knowledge I have gained over the course of the last year. I have made an effort to explain everything clear enough to be understood by myself a year ago. However, when working with such a complicated experiment as the one going on at CERN, a lot of considerations and conclusions have been made prior to this study. They can not all be described in detail, but an explanation has been included when it helped more than hindered the understanding of a given point (otherwise a reference will be given, encouraging further reading).

It is no wonder that there is work for thousands of people, trying to build up the understanding of particle physics one step at a time. This thesis is my contribution. There is still a lot of work to be done.

Morten Ankersen Medici
Copenhagen, 2013.

Models of the particle world

> *"It is fashionable to carry the story all the way back to Democritus and the Greek atomists, but apart from a few suggestive words their metaphysical speculations have nothing in common with modern science, and although they may be of modest antiquarian interest, their genuine relevance is negligible"* [1]

We obtain all information about the elementary particles and their interactions from indirect sources like decays, scattering or in bound states. Needless to say, one can only

expect a model to be able to describe the characteristics and interactions of such processes. Ever since 1897, when it was observed that the ray in a cathode tube consists of small charged particles much lighter than hydrogen (the lightest bulk of matter known at that time), the modern description of elementary particles has developed. At present the Standard Model is our best 'guess' of what is going on at the level of elementary particles. Incorporating special relativity and quantum mechanics, it has been rather successful in describing the tiny world of elementary particles.

Naturally the Standard Model has some limitations, as it does not describe gravity nor dark matter, neither does it describe the observed neutrino oscillations (just to mention some obvious issues). However, it explains and predicts the processes on particle level very well in high energy collisions.

Motivation and scope of this thesis

When considering proton-proton collisions, the theoretical predictions of the strong interaction match the observation very well when the transferred momentum is large. When the transferred momenta is low this is no longer the case. At present no satisfactory description of these low energy events exists. The experimental focus has naturally been on the processes that can verify the Standard Model, obtained in high energy collisions. With the discovery of the Higgs boson [2], the search for particles predicted by the Standard Model is concluded. Unless additional particles are discovered when the collision energy is increased, the next step will be to understand the low energy interactions.

No matter what happens in the high energy sector, investigations in low energy interactions are of grave importance. Studies such as the Minimum Bias Analysis in ATLAS is one approach to help modeling these interactions, to catalyze the understanding. The analysis exactly shows that the majority of processes in ATLAS happen at low energies.

Elastic scattering of protons, described by low momentum transfers, are responsible for 20-30% of the interactions happening in the collisions of protons. The scattering of hadrons must be due to the exchange of gluons and quarks, bundled in a colorless object such as a meson. The exchange of any of the known mesons can be described in Regge theory. However, at high energy the elastic process is believed to be dominated by some unknown configuration of gluons, named pomerons. In order to investigate the properties of the pomeron, the diffractive events are examined. These are processes, with a low momentum transfer, where one or both protons dissociate due to the pomeron exchange. As will be discussed, the theoretical framework of Regge theory can not account for all observations, and thus the examination of diffraction is essential for a better understanding.

Using the ALFA detector it is possible to tag extremely forward flying protons from e.g. diffractive events, which otherwise escape detection. The ability to separate the diffractive events from non-diffractive events allows for a more detailed study. In this thesis the focus will be on the track multiplicities in ATLAS, and investigating the possibilities of determining the cross section for single and central diffraction.

The work presented is not conclusive, but an important first approach to the study of diffraction with ALFA. The studies have mostly been limited by the lack of a simulation of the corresponding processes. Diffractive events are heavily contaminated by other sources, and it is therefore difficult to create a clean sample, just from data driven methods. This is reflected in the various approaches presented in this thesis.

Outline

As an introduction to the terms and physical quantities discussed in the thesis, Chapter 1 introduces the Standard Model, with a short run through Quantum Field Theory. Chapter 2 is the authors attempt at presenting the dominant theoretical ideas on diffraction. In Chapter 3, 4 and 5 the experimental setup is presented, in terms of the LHC, ATLAS and the ALFA detector. The performance studies of ALFA carried out by the author is presented and discussed in Chapter 6. In Chapter 7 and 8 the Minimum Bias Analysis at 8 TeV is presented, with focus on the contributions made by the author. Finally the initial steps towards an analysis of diffractive events tagged by ALFA are presented and discussed in Chapter 9. Some concluding remarks on the work done, and an outlook to possible continuations of the project is rounding of the thesis in Chapter 10, followed by a few useful appendices and the bibliography.

Acknowledgments

My thanks goes first of all to Jørgen Beck Hansen for always having time for lengthy discussion about physics, programming, philosophy or the society. I would like to give a great thank you to Sune Jakobsen for several complete descriptions of the ALFA detector. Thanks to Matthieu Heller for keeping me entertained during summer, and every time we were in contact since. A great thanks shall go to the rest of the ALFA group Karl-Heinz, Patrick, Petr, Hasko, Kristof, Tom and everybody else doing a great job working with ALFA. Jorn Dines Hansen was our all-knowing wonder on Regge theory and together with delighted invitations from Gösta Gustafson to visit him at Lund University, a more complete insight was reached. Thanks to Oldrich Kepka, who kept accepting my questions every time I lost the overview, or had it with some data that did not do what it was supposed to do. I am grateful for the discussion and common frustrations on material response and physics in general with Wolfgang Lukas, even when we worked on something in the middle of the night, connected only on skype, it turned out good. Thanks for a fruitful collaboration on the minimum bias analysis, Simone, Andreas and Thorsten. Thank you Tomasz Stebel, you were a much valued office mate during the summer. A summer that would not have been the same without Olof Ahlen. For proof reading and many great discussions, thank you Christine Overgaard Rasmussen. Thanks to the rest of the people in building M: Alexandro, Almut, Anders, Ask, Bjorn, Craig, Dana, Gorm, James, Karina, Kristian, Lotte, Morten, Peter and Sascha for listening and taking time answering my questions even when I did not really know what I was asking. I would further like to thank Mikkel Skaarup and Simon Stark Mortensen for a great collaboration working with ALFA and ATLAS together for the first time, it has always been a pleasure to go to work with you guys. My beloved sister, thanks for the last minute grammatical corrections you provided. Dear Kristine, you have taken the best care of me, ensuring a good mood and my well being, in times when it was most needed, thanks for all the love you are giving me.

1

The Standard Model

The Standard Model (SM) of particle physics is very successful in describing the world of particle physics. It has passed all of the major tests and its predictions have been verified, latest with the discovery of a particle with the characteristics of the expected Higgs boson. The SM does not fail in predicting outcomes of experiments, but rather in the fact that it is lacking phenomenological descriptions of e.g. gravitation, dark matter and neutrino oscillations. It can be argued that the SM is too simplistic, but that shall not be discussed here. Here it will merely be viewed as a model, so far capable of describing the world of particle physics very well.

In this thesis natural units will be employed, i.e. $c = \hbar = 1$, such that mass, momentum and energy will all have units of electron volts, eV.

1.1 The elementary particles

The SM describes the world in terms of the smallest known constituents, and their mutual interactions, presented in Figure 1.1. The elementary particles come in two variants: Matter particles, the spin-$\frac{1}{2}$ *fermions*, and force carriers, the spin-1 *gauge bosons*, that mediate the possible interactions. The spin-0 *Higgs boson* is the resonance of the Higgs field, responsible of given masses to the weak gauge bosons, and to the fermions. The fermions are divided in two categories: the *quarks* and the *leptons*, each with three families, of similar characteristics. All the fermions have associated *anti-particles*, with the same mass, but opposite quantum numbers. These are denoted with a bar, such that $\bar{f}$ is the anti-particle of f.

The SM describes particle interactions in terms of three different forces of nature; the strong, weak and electromagnetic forces. Compared to the strength of these forces one can neglect the gravitational force at the scale of particles. Each force is mediated by corresponding gauge bosons, thus the SM is modeling all interactions as the exchange of said bosons. The gluons mediate the strong force, the photon mediates the electromagnetic force, and the Z^0 and $W^{\pm}$ bosons mediate the weak force.

Quarks are the only fermions with the strong *color* charge, and are with gluons the only particles that interacts strongly. Color charged particles do not exist freely, but are confined in bound states of *hadrons* with either two (*meson*) or three quarks (*baryons*). The electrically charged fermions can interact via the electromagnetic force. All known fermions can interact with the weak force.

1.2 Quantum Field Theory

The allowed interactions in the SM are described in the mathematical language of Quantum Field Theory (QFT), the unification of quantum mechanics and special relativity.

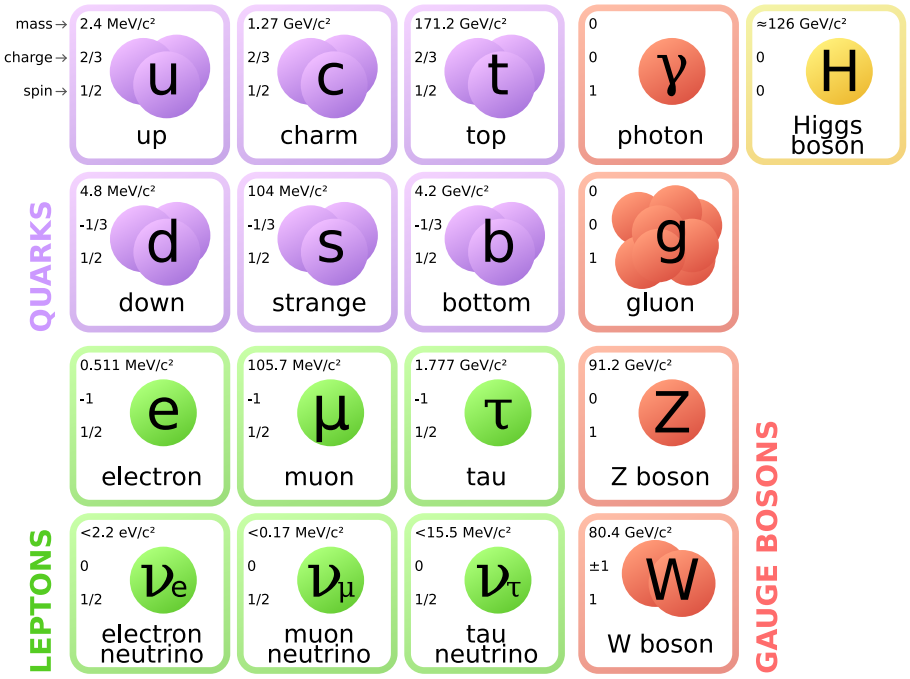

Figure 1.1: The elementary particles of the Standard Model, notice that some particles comes in multiple variants (as well as that antiparticles exist for all the particles) [3].

Taking from special relativity the possibility to violate mass (only energy and momentum are conserved), and from quantum mechanics the indeterminacy, it is formulated to describe interactions on small length, short times, at high energies. This is exactly the scale of particle interactions, and thus the suitable framework for SM. The ability of QFT to calculate a large range of observable quantities, and the experimental confirmation of these, is the natural reason for using QFT [4].

Lagrangian and symmetries

In classical field theory a physical system with a finite number of degrees of freedom can be characterized by a Lagrangian, $L(q_i, \dot{q}_i)$, of the generalized coordinates q_i, and the corresponding derivative $\dot{q}_i$. By minimizing the action one can determine the evolution of the physical system [5].

In QFT, one describes physical systems in terms of fields $\varphi(\vec{x}, t)$, that has a continuous number of degrees of freedom. This is necessary due to the relativistic possibility of creating matter particles from energy ($E = mc^2$), and the quantum mechanical Heisenberg relation, $\Delta E \Delta t = \hbar$, stating that matter can be created even though the necessary energy is not present [4].

Restricting ourselves to local theories, the Lagrangian for a continuous field can be written as the space integral of the Lagrangian density $\mathcal{L}$ [6]:

$$L = \int d^3x \mathcal{L}\left(\varphi(\vec{x}, t), \dot{\varphi}(\vec{x}, t), \vec{\nabla}\varphi(\vec{x}, t)\right) \tag{1.1}$$

By minimizing the action one can, as in classical field theory, find the Euler-Lagrange equations for $\mathcal{L}$ governing the dynamics of the field.

In this way the QFT framework can be used as follows: Given a Lagrangian, one quantize it (i.e. reinterprets the dynamical variables as operators) and from hereon one can calculate which interactions are possible for the fields considered in this given Lagrangian.

Symmetries of the Standard Model

The Lagrangian density of the SM is based on symmetries, i.e. transformations which leave the equations of motions unchanged. The importance of symmetries arises from Noethers theorem, which states that any differentiable symmetry of a physical system has a corresponding conserved quantity [4]. Conservation laws can be experimentally tested, and a it has been observed how a certain properties of the elementary particles are conserved in interactions. Following this line of thought, SM has been developed in terms of symmetries.

First of all the demand for symmetry under transformations by the Poincare group, is imposed in order to comply with special relativity [4]. This describes that translations, rotations and boosts are *global* symmetries, leading to the conservation of linear and angular momentum as well as the position of the mass center. Another global symmetry is time translation, leading to conservation of energy.

Secondly the principle of *local gauge invariance* is of huge importance to the SM. A gauge transformation can be understood as a rotation between different states of a field. Requiring that the Lagrangian density should be invariant under a certain gauge transformation, implies the introduction of a number of gauge fields (depending on its properties).

By demanding local gauge invariance in SM, the interactions get fixed, and the force carriers or *gauge bosons* emerge (hence the name). The classic textbook example is to employ gauge invariants of U(1) (the group of complex numbers of modulo 1), from which it is merely a matter of mathematics to produce Quantum Electrodynamics (QED) describing the electromagnetic force. In a similar way the weak and strong force is introduced to the theory by implying certain gauge invariants. Further the discrete symmetries of time-reversal T, parity P and charge conjugation C are of historical relevance, as they have been probed much in experiments. Currently, only the combination, CPT, seems to be a symmetry of SM, though this is anyway demanded for the model to be Lorentz invariant [4].

The explicit derivation of SM shall not be given here (a job more fit for a textbook than a thesis), though some aspects of the QFT framework need to be introduced.

Feynman diagrams

A clever way of managing the possible transition of the fields from one state to another, is by the use of Feynman diagrams. Each topologically different diagram with same initial state i and final state f contributes to the transition amplitude $A(i \to f)$, capable of describing the transition probability. From a given Lagrangian density describing a set of fields, one can basically describe all possible transitions in terms of two objects:

Propagators describing the movement of particles, determined by their momentum. Propagators going in or out of a diagram (*external* lines) must be *on mass shell*, while this is not the case for *internal* lines.

Vertices describing the possible interactions between particles, which are determined from the theory (given by the Lagrangian). For each type of vertex a *coupling constant* describes the strength of that interaction.

A particle with four momenta p and mass m is said to be on its mass shell if $p^2 = m^2$. An example of a Feynman diagram is shown in Figure 1.2, for the process of $e^- + e^+ \to e^- + e^+$. For time flowing to the right, an arrow pointing forward in time indicates a particle, and an arrow pointing backwards in time indicates an antiparticle. From the Lagrangian density it is calculated how each propagator and vertex contribute to the diagram, and

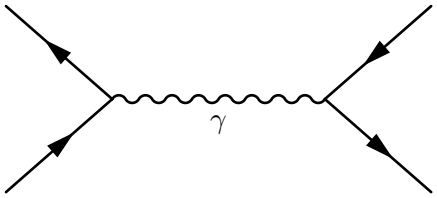

Figure 1.2: Feynman diagram for the process $e^- + e^+ \rightarrow e^- + e^+$.

thereby how that diagram contributes to the overall transition amplitude. Some Feynman diagrams will be employed in this thesis, as the full QFT machinery will not be needed for the description of the processes discussed.

Next to leading order The diagrams can be more and more complicated by adding more vertices or using more complex vertices. Though as more vertices are added the contributions become less and less significant (for coupling constants less than 1), and normally only the leading order (LO) terms of the amplitude are needed to make predictions within experimental precision. These are the diagrams with the fewest possible vertices needed to make the transition $i \rightarrow f$. The diagrams that can be combined to give a higher order of coupling strength for the squared amplitude constitutes the next-to leading order (NLO). This can naturally continue to higher orders of coupling strength, giving a more correct prediction of the transition amplitude. Denoting the degree of detail for the theoretical calculations in this way gives a rough measure of how many details are included in a given calculation. Simulations used in this thesis will only include LO.

Renormalization

For NLO diagrams and higher, the momentum of the internal lines can not be determined from the momenta of the external lines. Instead, one needs to integrate out that degree of freedom, and for diagrams with loops this can lead to divergent terms in the transition amplitude. For theories of four dimensions which do not include vertices with more than four lines (as is the case of SM), these can be *regularized* followed by *renormalized* resulting in finite integrals [7]. No details of this procedure shall be given here, though an important consequence of renormalization is that the coupling constant become *running*. Which simply means that the coupling constant of a given interaction is varying with momenta.

Some features of the coupling constant of the strong force, α_s, shall here by given due to its relevance for the study carried out in this thesis. It turns out that it goes to infinity as the momentum decreases. Thus explaining why quarks are not observed as free isolated particles, but only observed in bound states due to this *color confinement*. As the distance between two quarks increase, α_s grows, until it is more energetic favorable to create a quark anti-quark pair between the separating quarks. For increasing momenta, α_s goes to zero, implying that quarks move freely about inside the hadrons, known as *asymptotic freedom*. This is essential for using perturbation theory in high energy interactions.

Imposing renormalization imply that all the interactions have running coupling constants, though at LHC energies the three forces shall be characterized by relative strengths of 10^{-1}, 10^{-2} and 10^{-6} for the strong, electromagnetic and weak force respectively (at interaction energies around the mass of the Z) [8].

Cross section

Having determined the transition amplitude $A(i \to f)$, one can predict various physical quantities. Though most important is the calculation of the cross section σ. In the S-matrix formulation of QFT (discussed in Appendix A.2), the differential cross section is for a differential phase space element $d\Omega$ given by squaring the transition amplitude and normalizing to the incident flux Φ:

$$d\sigma = \frac{1}{\Phi}|A(i \to f)|^2 d\Omega. \tag{1.2}$$

Experimental significance of the cross section The cross section is of interest, as it serves as a measure for the probability of a given process to occur in collisions. The cross section, σ, of a process $|i\rangle \to |f\rangle$, relates the number of colliding particles per unit time per unit area, $\mathcal{L}$, in an accelerator, to the measured rate of occurrences with $|f\rangle$ as outcome, R [5]:

$$R = \sigma\mathcal{L}. \tag{1.3}$$

The *luminosity* $\mathcal{L}$ is determined by the accelerator providing the collisions, and will be discussed more thoroughly in Section 3.4.

Though no detector is perfect nor covers the entire solid angle, the efficiency ϵ and acceptance A of the detector must be accounted for when measuring R. A lot of the work presented in this thesis will be on understanding and estimating detector efficiencies, in order to calculate a reliable value for the cross section.

1.3 Hadron-hadron collisions

Using Feynman diagrams, one can access the possibilities and theoretical predictions of SM in a fairly simplistic way. However when one wants to probe protons, the situation becomes more complicated, as they are hadrons. Because of the asymptotic freedom, the quarks in the hadrons move freely around. They can radiate off gluons, which in turn can split into quark-anti quark pairs, thus a proton is expected to contain not just the *valence quarks* (two up and a down), but a sea of quarks and gluons.

Say one wants to calculate the theoretical cross section of $a+b \to X+Y$ in a high energy collision of protons, where a and b are *partons* of the proton. Such a calculation must take the composite nature of the proton into account. How to handle this complication depends on the characteristic energy Q^2 of the two interacting partons, and one normally one divides the processes into two different energy regimes.

Hard processes

In *hard processes* with a large momentum transfer, i.e. $Q^2 \gg 1$ GeV^2, the partons are taken out of the protons with high energy (resulting in possible high p_T jets). Thus the wave function of the interacting parton can be assumed not to interfere with the wave function of the proton. Hence the scattering process can be divided in two; (1) taking out the partons from the protons and (2) letting the partons interact.

Because of the high energy of the interacting parton, all interactions that occurs during (1) can to a good approximation be described by a probability density, or the parton distribution functions (PDF). The PDFs describe the probability for a certain parton to have momentum fraction x of the proton. The probability to take out a parton a with momentum fraction x_i of proton i, at a given Q^2 is denoted $f_{a/i}(x_i, Q^2)$, and the

usefulness of the PDFs lies in the fact that they have been observed to be universal across a large range of processes [9]. In (2) the cross section of the partonic interaction, σ_{hard}, can be calculated from QFT exploiting that the strong coupling is small at high energies. Thereby the calculations can be carried out using perturbation theory (*perturbative QCD*).

The theoretical differential cross section of a given process in proton-proton collisions can thus be found as [9]:

$$d\sigma(pp \to XY) = \sum_{a,b}^{\text{flavors}} \int dx_1 \int dx_2 f_{a/1}(x_1, Q^2) f_{b/2}(x_2, Q^2) d\sigma^{\text{hard}}(ab \to XY). \quad (1.4)$$

This *factorization theorem* is the essential assumption for describing high-p_T processes.

Soft processes

When the energy of the interacting parton is comparable to the initial state interactions, the factorization theorem is no longer a suitable approximation. At this energy level these processes are referred to as *soft processes* and are generally characterized by a relatively low transfered momenta, i.e. $Q^2 \sim$ few hundred MeV^2. For strong interactions this regime is inherently non perturbative, and thus a very difficult regime to describe theoretically in terms of QFT.

The factorization theorem is the basis of most experimental particle physics today, as perturbative QCD can provide some of the most precise predictions of QCD. Though as mentioned, its scope is limited to the high-p_T regime. The work of this thesis is focusing on processes which are outside the regime where QFT can be applied satisfactory. Thus, one needs to take another approach.

2

Low p_T processes in proton-proton collisions

When discussing proton-proton collisions it can be useful to divide all the possible processes into groups of processes characterized differently. Let σ_{tot} signify the total cross section, the sum of all possible processes that can happen in proton-proton collisions. Then the total cross section can first of all be divided into the contribution from *elastic* scattering, and other *inelastic* processes:

$$\sigma_{\text{tot}} = \sigma_{\text{elastic}} + \sigma_{\text{inelastic}}. \tag{2.1}$$

Elastic scattering signifies processes where both protons stay intact, whereas this is not the case for inelastic processes.

In this chapter the elastic scattering shall initially be discussed, and the Regge formalism and the accompanying pomeron shall be introduced, which is crucial for the subsequent definition of diffractive processes. From the definition it will become apparent that elastic scattering can be characterized as the low momentum transfer limit of a diffractive process. Unless otherwise noted this chapter is based on Ref. [10].

2.1 Two body scattering

Let the particles of the two-body process, $1+2 \to 3+4$, be denoted as presented in Figure 2.1, with the gray areas denoting any interaction. Elastic scattering is the special case of the two body process, where the same particles that collide come out of the process, without any energy transfer.

The two body process is usually described by the three Mandelstam variables

$$s = (p_1 + p_2)^2 = (p_3 + p_4)^2, \tag{2.2}$$
$$t = (p_1 - p_3)^2 = (p_2 - p_4)^2, \tag{2.3}$$
$$u = (p_1 - p_4)^2 = (p_2 - p_3)^2. \tag{2.4}$$

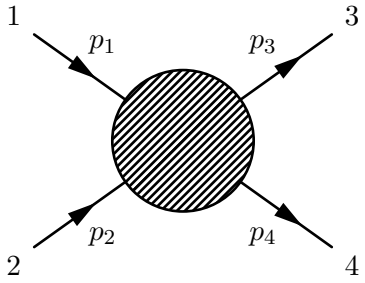

Figure 2.1: The two body process where the gray areas signifies any possible interaction. Elastic scattering is the special case where $1 = 3$ and $2 = 4$.

The Mandelstam variables correspond to the momentum transfer of the exchanged particle in the process, dependent on how the exchange occurs. One can also interpret (2.2-2.4) as the center of mass energies in the s, t and u channels defined by:

$$1 + 2 \to 3 + 4, \qquad (s\text{-channel}), \tag{2.5}$$
$$1 + \bar{3} \to \bar{2} + 4, \qquad (t\text{-channel}), \tag{2.6}$$
$$1 + \bar{4} \to 3 + \bar{2}, \qquad (u\text{-channel}), \tag{2.7}$$

when $\bar{3}$ is the anti particle of 3, with $p_{\bar{3}} = -p_3$. The Mandelstam variables obey

$$s + t + u = \sum_{i=1}^{4} m_i^2, \tag{2.8}$$

which can be derived from (2.2-2.4), using energy-momentum conservation. In the s-channel, t corresponds to the squared momentum transfer, which together with s will be used as classifiers for the process. Only two parameters are needed to describe the kinematics of the four particles, as the energy and momentum of the four particles are constrained by energy-momentum conservation (4 constraints), the mass shell condition on the four particles (4 constraints) and by fixing the Lorentz frame, e.g. to the center of mass frame (6 constraints).

2.2 The optical theorem

The significance of the elastic scattering lies in the fact that the elastic scattering amplitude can be related the total cross section. Assuming unitarity of the S-matrix, one can show that (see Appendix A.2):

$$\sigma_{\text{tot}} \sim \frac{1}{s}\text{Im}A_{\text{el}}(s, t = 0), \qquad s \to \infty, \tag{2.9}$$

where A_{el} is the elastic scattering amplitude.

Resembling the optical equivalent discovered many years before, the relation is known as the *optical theorem*. The optical theorem is essential for determining the total cross section, as it would naturally not be possible to measure the cross section for each and every process. This is basically the reason for installing the ALFA detector; it has the possibility to detect elastic scattered protons (as will be explained in Chapter 5), and thereby determine the total cross section.

Measuring the total cross section From the S-matrix formulation one can find the differential cross section for elastic scattering to be (see derivation of (A.28))

$$\begin{aligned} \left.\frac{d\sigma_{\text{el}}}{dt}\right|_{t=0} &\sim \frac{|A_{\text{el}}(s, t = 0)|^2}{16\pi s^2}, \qquad s \to \infty \\ &= \frac{1 + \rho^2}{16\pi}\sigma_{\text{tot}}^2. \end{aligned} \tag{2.10}$$

Where the second equal sign comes from using the optical theorem (2.9), and introducing

$$\rho = \frac{\text{Re}A_{\text{el}}(s, t = 0)}{\text{Im}A_{\text{el}}(s, t = 0)}, \tag{2.11}$$

which can be determined in the limit of very low t events, where the combination of the coulomb and hadronic scattering give rise to an interference term with ρ. Using (1.3) it is clear that

$$\frac{dR_{\text{el}}}{dt} = \frac{d\sigma_{\text{el}}}{dt}\mathcal{L}. \tag{2.12}$$

Combining (2.12) and (2.10) one finds that

$$\sigma_{\text{tot}}^2 = \frac{16\pi}{1+\rho^2}\frac{1}{\mathcal{L}}\left.\frac{dR_{\text{el}}}{dt}\right|_{t=0}. \tag{2.13}$$

It is not possible to measure the number of events at $t = 0$ directly, as they stay within the beam. Instead the elastics are measured as close to $t = 0$ as possible and then extrapolated to the point of $t = 0$, assuming an exponential fall off with t (expected from Regge formalism which shall be discussed in the following).

Having an independent measure on the rate of inelastic events R_{inel}, one can determine

$$R_{\text{el}} + R_{\text{inel}} = R_{\text{tot}} = \sigma_{\text{tot}}\mathcal{L}. \tag{2.14}$$

Combined with (2.13), a measure of the total cross section independent of the luminosity can be achieved.

In the present analysis of the total cross section in the ALFA group, the parameter ρ is determined from the phenomenological models of COMPETE [11], and the luminosity determined by ATLAS is used [12] (see Section 3.4).

The TOTEM collaboration, which is the corresponding forward physics program of CMS, has published its results on the total cross section, one of which includes an independent measure of N_{inel} [13, 14, 15].

2.3 Regge formalism

The dominant theoretical description of the elastic scattering amplitude, is the one from Regge formalism. As a result of how the scattering amplitude is characterized, the scattering shall be explained by the exchange of multiple particles. This leads to the notion of the pomeron, which is very important for the description of diffraction.

It should be apparent from this discussion that Regge theories are not able to fully predicts the behavior in proton-proton interactions. In this section only two body process of spin-less particles shall be considered (for more complicated processes, the reader is referred to [16]).

Scattering amplitude

As discussed in Section 2.1, the kinematics of the two body process can be described by just two variables; the Mandelstam s and t. Likewise they should suffice to characterize the scattering amplitude, $A(s,t)$.

Using Legendre polynomials $P_l(z)$, the scattering amplitude in the t-channel can be expanded in the partial wave series [17]

$$A(t, s(t, z_t)) = 16\pi\sum_{l=0}^{\infty}(2l+1)A_l(t)P_l(z_t), \qquad z_t = \cos\theta = 1 + \frac{2s}{t-4m^2} \tag{2.15}$$

where $A_l(t)$ are partial wave functions at angular momenta $l = 0, 1, 2, ...$, carrying the t singularities . The parameter z_t is usually introduced, and can safely be used as it varies

linearly with s. Eq. (2.15) works fine in the t-channel, corresponding to the region of $t \geq 4m^2$ and $s < 0$. Though it can not be continued into the s-channel, the region of $s \geq 4m^2$ and $t < 0$, as this corresponds to $|z_t| > 1$ for which the series of Legendre polynomials $P_l(t)$ does not converge [18].

In QFT *crossing symmetry* is postulated. It implies that the scattering amplitude should describe both the s-, the t- and the u-channel, (i.e. the different physical domains), with a function that can be analytically continued from one channel to the other. This is obviously not the case for (2.15).

Complex angular momentum

One way around this issue is by introducing a complex angular momentum. This means letting $A_l(t)$ be continued in to an interpolating function $A(l,t)$ (fulfilling certain criteria) for which it holds that

$$A(l,t) = A_l(t), \qquad \text{for } l = 0, 1, 2, ... \tag{2.16}$$

If one assumes that all the singularities of $A(l,t)$ are *poles* in the complex plane at integer l, one can employ the methods of complex contour integration to recast the scattering amplitude $A(t, s(t, z_t))$ in the *Watson-Sommerfeld representation*. From this representation the scattering amplitude can be evaluated in any of the regimes of the s, t and u-channel. The details of the derivation are outside the scope of this thesis, and the reader is referred to [10]. Hereby the demand for crossing symmetry has been fulfilled. Further this description entails a variety of phenomenology as shall be apparent in the following.

Exchange of resonances

From the Watson-Sommerfeld representation one can take the limit of $s \to \infty$, get the asymptotic scattering amplitude of the s-channel

$$A(s,t) \underset{s\to\infty}{\sim} -\beta(t)\frac{s^{\alpha(t)}}{\sin \pi\alpha(t)} \qquad \text{(leading pole only)} \tag{2.17}$$

where $\alpha(t)$ is the location of the leading pole with residue $\beta(t)$, i.e. the pole with the highest $\mathrm{Re}\alpha(t)$. The corresponding expressions for relativistic scattering shall not be discussed here, but can be found to exhibit the same structure of $A(s,t) \sim f(t)s^{\alpha(t)}$ for $s \to \infty$.

The partial wave amplitude must close to the pole behave like

$$A(l,t) \sim \frac{\beta(t)}{l - \alpha(t)}. \tag{2.18}$$

Suppose that for a certain t_0, $\alpha(t_0) = l + i\epsilon$. Expanding $\alpha(t)$ around t_0 to $\mathcal{O}(\epsilon)$, the partial amplitude can be written as

$$A(l,t) \sim \frac{\beta(t)}{t - t_0 + i\Gamma}, \qquad \Gamma = \frac{\epsilon}{\alpha'(t_0)}. \tag{2.19}$$

This corresponds to a Breit-Wigner for a resonance of mass $m = \sqrt{t_0}$, and thus for real positive t, each pole of $A(l,t)$ represents bound states of increasing angular momentum l. Looking at it this way, the scattering amplitude of the s-channel (2.17) dependents on all the resonances that can be exchanged in the t-channel (conserving quantum numbers). These resonances are found experimentally, and some of them are presented on Figure 2.2, where each color corresponds to a certain *family* of resonances, with equal quantum numbers.

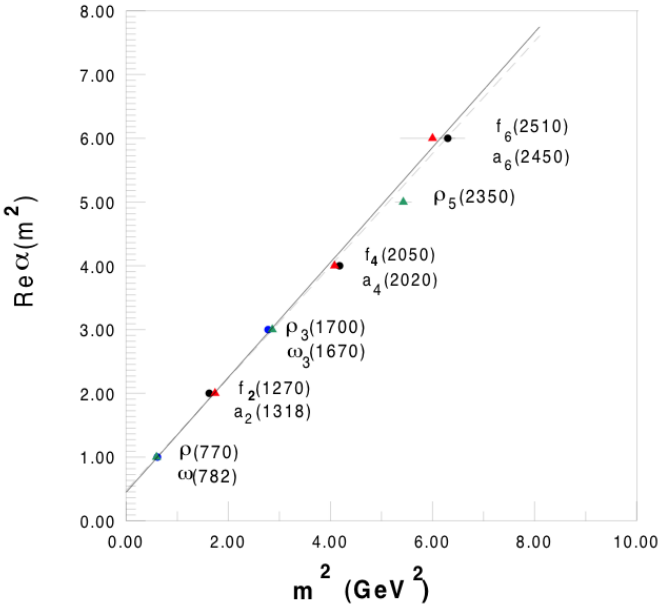

Figure 2.2: Some of the observed resonances in the t-channel of proton-proton collisions corresponding to the poles of the scattering amplitude in the s-channel, shown with the interpolating Regge trajectory [19].

Regge trajectories

The function $\alpha(t)$ interpolating the resonances is called a *Regge trajectory* (in the literature also called a *reggeon*). As seen on Figure 2.2, the families almost lie on top of each other. Moreover, it is seen that one can (at least in this range of t) approximate the Regge trajectory with a straight line

$$\alpha(t) = \alpha(0) + \alpha' t, \tag{2.20}$$

which for the leading mesonic trajectories presented in Figure 2.2 corresponds to $\alpha(0) \simeq 0.5$ and $\alpha' \simeq 1$ GeV^{-2}. More trajectories exist (e.g. higher mass resonances with strangeness) with the same slope but a lower intercept.

Using the optical theorem (2.9) and the scattering amplitude predicted by Regge theory (2.17), one would expect the total cross section to be

$$\sigma_{\text{tot}} \sim \frac{1}{s}\text{Im}A(s, t=0) \sim s^{\alpha(0)-1} \qquad \text{(leading pole only)}, \tag{2.21}$$

hence the exchange of mesons results in a cross section that should fall off as $\sim s^{-0.5}$ (or faster if more trajectories are included). On Figure 2.3 the measurements of the total cross section are presented, and σ_{tot} is seen first to decrease, then increase for higher CM energies. Thus the mesonic trajectories alone can not account for the behavior of the total cross section.

2.4 The pomeron

To account for the increase an additional Regge trajectory is introduced. It is known as the *pomeron* (denoted with $\mathbb{P}$) and with an $\alpha_{\mathbb{P}}(0) > 1$, it would describe the s dependence of σ_{tot}. The data can be quite well fitted with a sum of trajectories as [21]:

$$\sigma_{\text{tot}} = Xs^{0.5475-1} + Ys^{1.0808-1}, \tag{2.22}$$

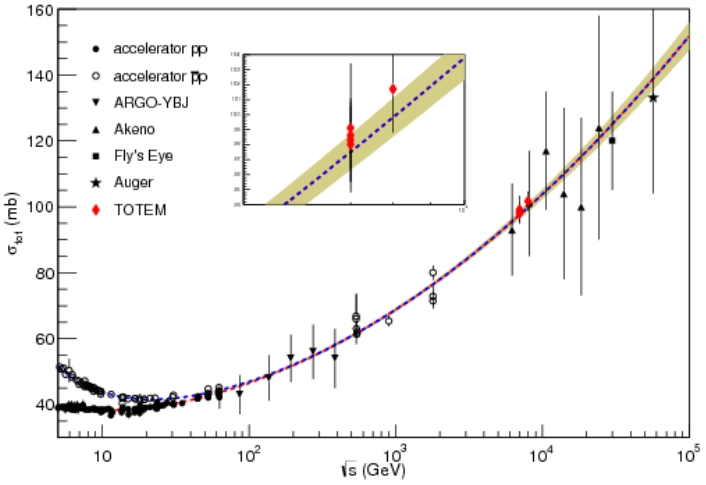

Figure 2.3: Total cross section of pp and $p\bar{p}$, for various CM energies, superimposed is a fit to $\ln^\gamma s$ functions (see text) [20].

where X and Y are reaction dependent free parameters. This corresponds to the leading mesonic trajectories presented on Figure 2.2, and the introduced pomeron trajectory. There has been proposed a long list of similar Regge inspired models for the total cross section, predicting pomeron intercepts of $1.08 < \alpha_{\mathbb{P}}(0) < 1.35$ dependent on the model [22, 23, 24, 25, 26].

Saturation effects of the pomeron trajectory

The power series of the type s^λ with $\lambda > 0$ used in (2.22) are expected from Regge theory, but these will eventually violate the *Froissart-Martin bound*. It states that

$$\sigma_{\text{tot}}(s) \leq C \ln^2 s, \qquad \text{as } s \to \infty, \tag{2.23}$$

with $C \geq \frac{\pi}{m_\pi^2}$. The Froissart-martin bound can be proved in various ways, but essentially follows from assuming unitarity and analyticity of the scattering amplitude. As the lower bound on C is much larger than the value measured for $\sigma_{texttot}$ at present energies, (2.23) is not really constraining the fits, though it must be taken into account for a full theoretical prediction.

The data for the total cross section can be fitted just as well with some $\ln^\gamma s$ dependence, which is the case for the fit presented on Figure 2.3. This has earlier been used, hoping for a $\gamma < 2$, though the most recent fits to the data at LHC energies favors a $2 < \gamma < 2.3$ [20], and is thus not satisfying the Froissart-Martin bound.

More advanced theoretical calculations includes the reasonable assumption of having multi pomeron exchanges, which might lower the energy dependence of σ_{tot}, though the effect depends on the model.

Interpretations of the pomeron

In order for Regge formalism to sustain its description of the total cross section, one has to accept the pomeron. Even so it is not clear how this trajectory should be interpreted.

It is known that the pomeron trajectory corresponds to the exchange of vacuum quantum numbers, and as it is not a baryonic or mesonic exchange, it could in terms of QCD correspond to some gluonic exchange. Describing the pomeron as a two gluon exchange

[27, 28] corresponds to $\alpha_{I\!P} \sim 1$, resulting in a constant contribution to the total cross section. The idea of a gluon ladder [29] predicts a $\alpha_{I\!P} \sim 1.5$, which would give a larger energy dependence of the total cross section than observed. At HERA (H1 and ZEUS) it was discovered that the energy dependence increases for increasing transferred momenta t [30]. It has been speculated that this might be due to contributions from two different pomerons, acting at different energy scales. However, there is to the author's knowledge no consensus on this topic.

The pomeron trajectory can be extrapolated to the physical region of the t-channel corresponding with a resonance of spin-2 and mass $\sim$ 2 GeV. Identifying the pomeron as some gluonic exchange, it could be ascribed to some kind of glueball resonance. It is striking to see how the glueball candidate found at spin-2 of mass 1.9 GeV [31, 17, 32] lies directly on the fitted pomeron trajectory in (2.22). There could be more information to be gained from the running experiment COMPASS, having presented preliminary estimates of the sensitivity of detecting glueballs [33]. Hopefully it will provide an update on the search for a glueball candidate, which at the moment is far from conclusive.

2.5 Diffractive scattering in hadronic collisions

The inelastic contribution to the total cross section introduced in (2.1), can in a simple way be subdivided into diffractive processes and non diffractive (ND) processes:

$$\sigma_{\text{inelastic}} = \sigma_{\text{diffraction}} + \sigma_{\text{non-diffractive}}. \tag{2.24}$$

Having introduced the pomeron as the dominant exchange of vacuum numbers in high energy scattering, it comes natural to introduce the notion of diffractive scattering as follows:

> An inelastic reaction where no quantum numbers are exchanged between high energetic colliding particles is a diffractive reaction.

The remaining processes shall thus be classified as non-diffractive events. The concept of this separation is visually depicted in Figure 2.4. One should notice that the definition of hadronic diffraction is not unanimous in the literature, but the definition above will be used in this thesis.

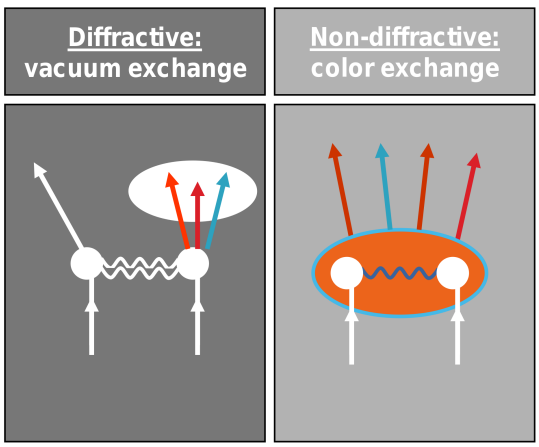

Figure 2.4: Classifying hadronic interactions as diffractive and non-diffractive processes Ref. [34].

Only defining diffraction at high energies is an experimental requirement needed to avoid contamination from non-diffractive contributions. Processes caused by the exchange of a π^0, i.e. diffractive, or by the exchange of a π^+, i.e. non-diffractive, are problematic if it is impossible to distinguish the final state of the two processes. However, since the mesonic exchanges are suppressed in high energy collisions (as discussed in Section 2.4), no types of pions will be exchanged. Instead the exchange will be dominated by the pomeron, hence be a diffractive process. Thus defining diffractive at high collision energies the ambiguities diminish.

The processes of interest in diffraction, are:

Single diffraction (SD): One of the incident particles comes out intact, while the other dissociates into a bunch of particles, with the same quantum numbers as the incoming particle (Figure 2.5(a)):

$$1 + 2 \rightarrow 1' + X$$

Double diffraction (DD): Both of the incident particles dissociate into bunches of particles, each with the same quantum numbers as the mother particle (Figure 2.5(b):

$$1 + 2 \rightarrow X_1 + X_2$$

Central diffraction (CD): Both of the incident particles continues intact, but an exchange happens between the two protons resulting in an additional particle shower (Figure 2.5(c)):

$$1 + 2 \rightarrow 1' + X + 2'$$

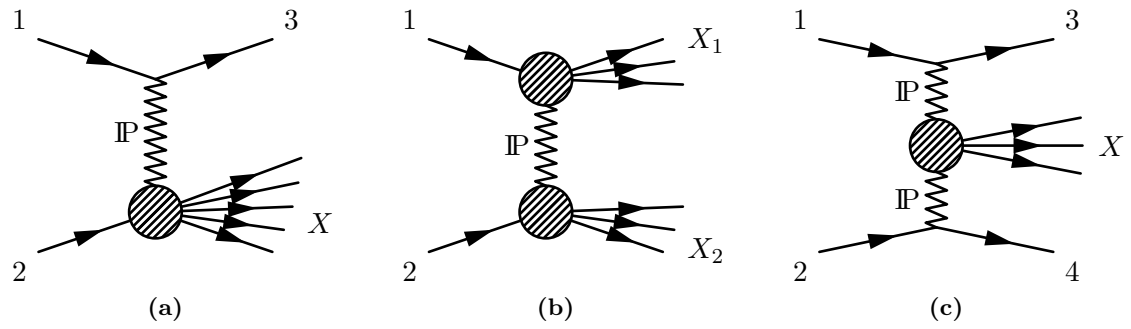

Figure 2.5: Diagrams depicting the most interesting process of diffraction: **(a)** Single diffraction **(b)** double diffraction and **(c)** central diffraction. The grayed blob signifies any reaction possible in that vertex.

2.6 Kinematics of diffraction

A lot of the steps taken in this thesis are based on an anticipation of a specific kinematic signature of the diffractive processes. Here the kinematics of single diffraction shall be considered, as the most simple diffractive process. Double diffractive processes are not of relevance to the work done with the ALFA, as will become clear when discussing the capabilities of the detector in Section 5.6. And even though the central diffractive events have very interesting possibilities (in terms of the particle production in the central system), only a limited analysis has been carried out.

Single particle inclusive processes

Single diffraction is a special case of the single-particle inclusive process:

$$1 + 2 \to 3 + X \tag{2.25}$$

Let the Mandelstam variables be defined as (2.2-2.4), with p_4 replaced by p_X. The X system is not a particle on mass shell, hence let the invariant mass of the X system be given by $M^2 = (p_1 + p_2 - p_3)^2$.

Let the energy and momentum of the 3 particles, be given as follows in the CM frame:

$$\begin{aligned} p_1 &= (E_1, \mathbf{p}) = (E_1, 0, 0, p_z) \\ p_2 &= (E_2, -\mathbf{p}) = (E_2, 0, 0, -p_z) \\ p_3 &= (E_3, \mathbf{p}') = (E_3, p_x, p_y, p'_z) \end{aligned} \tag{2.26}$$

Using this convention the scattering angle θ is introduced as

$$p'_z = |\mathbf{p}'| \cos\theta \tag{2.27}$$

Writing out s in terms of the energy, using that the particles are on mass shell, one finds that

$$\begin{aligned} E_1 &= \frac{1}{2\sqrt{s}}(s + m_1^2 - m_2^2), \\ E_2 &= \frac{1}{2\sqrt{s}}(s + m_2^2 - m_1^2), \\ E_3 &= \frac{1}{2\sqrt{s}}(s + m_3^2 - M^2). \end{aligned} \tag{2.28}$$

In the same way one can write out s in terms of the momenta to find

$$\begin{aligned} \mathbf{p}^2 &= \frac{1}{4s}\left[s - (m_1 + m_2)^2\right]\left[s - (m_1 - m_2)^2\right], \\ \mathbf{p}'^2 &= \frac{1}{4s}\left[s - (m_3 + M)^2\right]\left[s - (m_3 - M)^2\right] \end{aligned} \tag{2.29}$$

In the single diffractive process studied in this thesis, particles 1,2 and 3 are all protons with mass m. Hence in the limit of $s, M^2 \gg m^2$, one finds from (2.28) and (2.29) that

$$\begin{aligned} E_1, E_2 &= \frac{\sqrt{s}}{2}, \qquad E_3 \simeq \frac{s - M^2}{2\sqrt{s}}, \\ |\mathbf{p}| &\simeq \frac{\sqrt{s}}{2}, \qquad |\mathbf{p}'| \simeq \frac{s - M^2}{2\sqrt{s}}. \end{aligned} \tag{2.30}$$

Introducing the relative energy loss of the surviving proton (which will be used excessively in this thesis):

$$\xi = \frac{E_1 - E_3}{E_1} \simeq \frac{M^2}{s}. \tag{2.31}$$

Rapidity gaps

The frequently used variable *rapidity* is, for a particle with energy E, and z-momentum p_z, defined as

$$y = \frac{1}{2}\ln\frac{E + p_z}{E - p_z} \tag{2.32}$$

The usefulness of the rapidity is seen from the fact that it transforms additively under a Lorentz boost along z, which is particularly useful in particle collisions. This means that the difference in rapidity of particles in a collision can be considered in the CM system, as it is invariant under boosts. For a high energy proton ($p_z \to \infty$) the rapidity can be approximated by (see Appendix A):

$$y \simeq \ln \frac{2p_z}{\sqrt{p_T^2 + m^2}}, \tag{2.33}$$

where $p_T = \sqrt{p_x^2 + p_y^2}$ denotes the transverse momentum. For fixed M, one can in the limit of $s \to \infty$ use (2.30), and the maximal rapidity of particle 3 is then for $p_T = 0$

$$|y_3|_{\max} \sim \ln \frac{\sqrt{s}}{m}. \tag{2.34}$$

Let the X system consist of particles with the proton mass m. The largest value of the rapidity of the X system are achieved, when one particle carrying most of the momentum, i.e. it has $p_z \sim \sqrt{s}/2$, $p_T \sim 0$ and mass m:

$$|y_X|_{\max} \sim \ln \frac{\sqrt{s}}{m}. \tag{2.35}$$

The smallest value of the rapidity must be the case when all the particles in the X system share the momentum equally, such that the momentum is minimal, $p_z \sim (m/M)\sqrt{s}/2$, and the transverse momentum is maximal, $p_T^2 + m^2 \sim M^2$:

$$|y_X|_{\min} \sim \ln \frac{m\sqrt{s}}{M^2}. \tag{2.36}$$

Comparing (2.34) and (2.36) one find that the *rapidity gap* between particle 3 and the X system is given as

$$\Delta y \simeq (y_3)_{\max} - (y_X)_{\min} \simeq \ln \frac{s}{M^2}, \tag{2.37}$$

since the two systems fly in opposite directions.

In diffraction the transfer of z-momentum is $|\Delta p_z| \lesssim 1/R$, with R being the size of the target [35]. For a proton of size $R \sim 1$ fm [36], this reduces in terms of (2.30) to

$$1\text{GeV} \gtrsim |\Delta p_z| = |p_z - p_z'| \simeq \frac{M^2}{2\sqrt{s}}. \tag{2.38}$$

Thus at collider energies $M^2/s \ll 1$, which means that single diffraction will be dominated by low ξ, and using (2.37) it can be concluded that large rapidity gaps are to be expected in diffractive events.

Exploiting rapidity gaps

As it is not possible to detect all final state particles (due to inefficiencies and limited coverage, see Chapter 4), it is difficult to conclude whether there was any exchange of quantum numbers in the process, thus whether it was diffractive or not. Therefore it has been common to exploit the rapidity gaps, just shown to be a characteristic feature of diffractive processes.

Assuming that the final state particles of a non-diffractive event are evenly distributed in rapidity (exhibiting a *rapidity-plateau*), the number of tracks in a interval in rapidity,

Δy, will be given by a Poisson distribution. Thus the number of events having zero final state particles within this interval, i.e. exhibiting a rapidity gap of size Δy, will be exponentially suppressed

$$\frac{dN}{d\Delta y} \sim e^{-\Delta y}. \tag{2.39}$$

Thereby one will on average see more diffractive processes than non-diffractive processes in events with a large rapidity gap. As the size of the rapidity gap scales with energy per (2.37), the distinction between diffractive and non-diffractive events becomes more clear at higher energies. This complements the statement of defining diffraction only in high energy collisions.

Rapidity gap analysis To the author's knowledge, the only significant study of diffraction within ATLAS, has been the analysis of rapidity gaps [37]. A significant amount of events was indeed found showing non-exponentially suppressed rapidity gaps, as expected from earlier studies.

The rapidity gap analysis can be significantly improved by the use of ALFA detecting the surviving proton in a single diffractive processes. This characteristic shall in Chapter 9 be used for distinguishing SD and ND events.

2.7 Predictions of the diffractive cross section

Regge theory describing elastic scattering of hadrons, can also be able to describe diffraction.

At the energy scale of the LHC, the diffractive processes are as mentioned dominated by the exchange of pomerons, as the mesonic trajectories become insignificant at these energy scales. In the limit of $s \gg M^2 \gg t$ the differential cross section for single diffraction can be found to be given by Regge theory as [10]

$$s\frac{d\sigma_{\mathrm{SD}}}{dM^2dt} = f_{\mathbb{P}}(\xi, t)\sigma_{\mathbb{P}}(M^2), \tag{2.40}$$

where

$$f_{\mathbb{P}}(\xi, t) = \frac{1}{16\pi^2}|g_{\mathbb{P}}(t)|^2\,(\xi)^{1-2\alpha_{\mathbb{P}}(t)}$$
$$\sigma_{\mathbb{P}}(M^2) = g_{\mathbb{P}}(0)g_{3\mathbb{P}}(0)\left(M^2\right)^{\alpha_{\mathbb{P}}(0)-1},$$

with $g_{\mathbb{P}}$ and $g_{3\mathbb{P}}$ being coupling constants to be determined from experiments. Assuming a linear pomeron trajectory $\alpha_{\mathbb{P}}(t)$, the cross section is from (2.40) expected to fall of with t. At $t = 0$ for a given collision energy, the differential cross section has a ξ dependence of

$$\left.\frac{d\sigma_{\mathrm{SD}}}{d\xi dt}\right|_{t=0} \sim \frac{1}{\xi^{\alpha_{\mathbb{P}}(0)}}, \qquad (\text{fixed } s). \tag{2.41}$$

This has earlier been seen in to be approximately true for events with a low momentum transfer t [38].

Probing the dependence on the collision energy s, Regge theory predicts $\sigma_{\mathrm{SD}}/\sigma_{\mathrm{tot}} \sim s^{\alpha_{\mathbb{P}}(0)-1}$. Not only does this contradict experimental results showing a decreasing ratio as a function of energy [39, 40, 41], furthermore, with this description σ_{SD} alone would violate the Froissart-Martin bound.

One solution is to introduce a renormalization of $f_{\mathbb{P}}(M^2, t)$. Though not theoretically motivated, it works phenomenologically quite well in describing observations [42]. Indications of a quartic pomeron trajectory could point towards another solution [43]. However, at the moment there is no consensus in explaining the violation (to the author's knowledge)

Alternative approach Good and Walker introduced the notion of describing the incident protons in terms of eigenstates of the diffracted system [35]. Using this description, they predicted a steep distribution in momentum transfer, which was experimentally verified. In recent years a model based on the Good-Walker formalism has been developed in Lund. It describes the physics of diffraction using the approach of a so called *gluon dipole cascade*. In this description diffraction is modeled by fluctuations in the scattering process capable of reproducing (2.40). In this model fewer elements need to be fixed by experiments, compared to (2.40), and the saturation effects needed (for resembling data) can be incorporated by reducing the fluctuations, as the energy increases [25].

The currently available theoretical descriptions are clearly not conclusive. So far the diffractive cross section is in Pythia calculated from (2.40), though correcting functions are introduced to describe the behavior outside the asymptotic region [44, 45]. The idea is to use ALFA test the validity of the models.

Measuring the cross section of diffractive processes The cross section of diffractive processes is probed in different ways dependent on the equipment available. As will be discussed in Section 5.6, ALFA gives the possibility to look at single and central diffraction, by detection of the surviving proton(s). In combination with the detection of part of the dissociated proton, one has a large advantage in selecting diffractive events, compared to just having information on the dissociated proton. Determining the cross section of single and central diffraction is therefore a natural part of the ALFA program.

3

The Large Hadron Collider

In year 2000 the Large Electron Positron collider (LEP) was disassembled in order to make way for the Large Hadron Collider (LHC). The LHC uses the tunnel of LEP, a ring 27 km in circumference, 100 meter under the surface running under Lake Geneva and the Jura Mountains in Switzerland and France.

As the ALFA detectors are installed into the beampipe, knowledge of the LHC complex is necessary. This chapter shall serve as an introduction to only the most relevant parts of the accelerator. The information in this chapter is based on Ref. [46] when no other reference is given.

3.1 Layout

The LHC is a ring accelerator with two separate beam pipes for accelerating two beams of particles in opposite directions. The LHC is segmented into 8 straight segments 545 m long (connected by arcs), each signifying a sector of the ring, depicted on Figure 3.1 [47]. In four of the sectors the beams can be brought to collide at a designated interaction point (IP) of the straight segment. At each of these points a detector is installed in order to measure the outcome of the collisions. At point 1 the general purpose ATLAS detector is installed, which will be described in Chapter 4. The Compact Muon Solenoid (CMS) sits at point 5, and together with the TOTEM collaboration it constitutes the alternative experiment for studying diffraction (more details on CMS can be found in Ref. [48]). Other detectors sit at points 2 and 8 with focus on other types of physics.

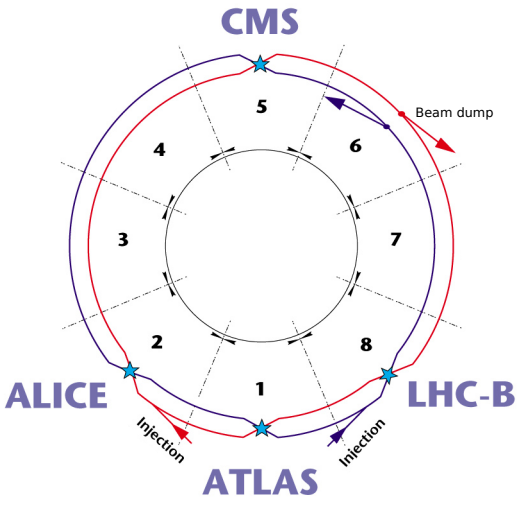

Figure 3.1: The division of LHC in 8 sectors, and the four interaction points [49].

3.2 Accelerating protons

The LHC is capable of accelerating protons and lead ions, though only protons shall be considered in this thesis. The protons are fed into the LHC via a chain of accelerators, depicted on Figure 3.2. In the LHC, each beam of protons are (in sector 4) accelerated to the design energy of 7 TeV, at a revolution frequency of $f_r = 11245$. The LHC has been running steadily with beams of energies up to 4 TeV so far.

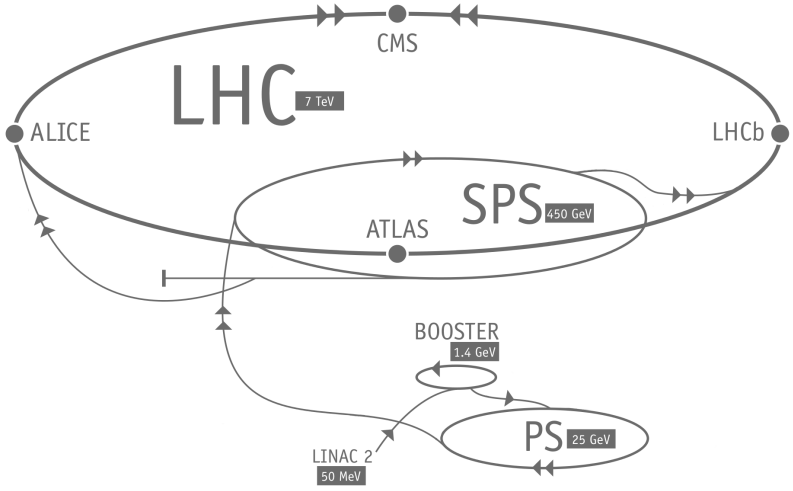

Figure 3.2: The chain of the protons in the LHC [50].

At each stage the acceleration is done using radio frequency (RF) cavities. For details on particle acceleration the reader is referred to Ref. [51], though one important consequence of using RF cavities is that it groups the protons into bunched structures.

LHC has room for 2808 particle bunches, which allows for proper injection and a time spacing called an *abort gap* (the time needed to turn on the magnet responsible for dumping the beam in sector 6). So far only up to half of these have been used simultaneously, and especially for the runs considered in this thesis, the numbers of filled bunches are much lower. Also the number of protons in each filled bunch varies for different runs, given the possibility for runs with higher or lower luminosity, to look for rare events or use more delicate instruments like the ALFA detector (this issue will be discussed more thoroughly in Section 5.4). Each possible position of a bunch is denoted by an ID and can be monitored.

3.3 Ensuring collision

The LHC uses 1232 dipole magnets to bend the beam around in the arcs. In the straight segments a number of magnets are used to steer the beams into a common beam pipe, and ensure a collision at the IP. The system of magnets can be set up into different configurations or *optics*, dependent on the how the collisions should proceed. This is of interest with regard to the measurements done with ALFA, as some of the magnets are installed in between ALFA and the IP. In the following the propagation of one beam shall be described, propagating along z and spreading out in the $(x - y)$ plane.

Let each particle in the beam be described by a vector (y, y'), with y being the position of the particle and y' is the slope of the particle path relative to the beam axis (with a

corresponding vector (x, x')). Then the evolution of the particle can be described by the multiplication of matrices onto the vector just introduced.

Assuming that there is no momentum dispersion, the transfer matrix describing the evolution of (y, y') through a system of magnets, can be reduced to a dependence upon the *β-function* [51]:

$$\begin{aligned} y(z) &\propto \sqrt{\beta(z)}, \\ y'(z) &\propto \sqrt{\frac{1}{\beta(z)}}. \end{aligned} \tag{3.1}$$

Thus the β-function is related to the transverse amplitude of the nominal beam at z, and (3.1) implies that the beam can not be extremely narrow and extremely focused at the same time.

The value of $\beta(z)$ at the IP is denoted β^*. To get high luminosity in the IP, the setup of the magnets is done such that a very low β^* of 0.65 m is achieved. This provides really narrow beams, ensuring as many interactions as possible. Thus it is preferable to introduce a small crossing angle to ensure that collisions only happen at the IP, avoiding beam-beam effects when the two beams share the same space in the beam pipe.

High β^* optics

As will be discussed in Section 5.4, the runs studied in this thesis use fewer bunches, and thus no crossing angle is needed, as only one bunch from each beam will be in the common beam pipe at the same time. Furthermore, the runs used for analysis in this thesis use a high β^* of 90 m. The reason for this is priority of measuring elastic scattered protons, as the protons will collide more head-on with increasing β^*. This gives more confidence that the measured scattering angles, correspond to the actual scattering angles. The specific optics is also used because it ensures *parallel to point focusing* in y, i.e. a proton at the beam energy will hit ALFA in the same point, regardless of the y position of the collision, reducing bias to the measurements.

For reconstructing the energy and momentum of the surviving proton in diffractive events, the low β^* optics is actually better suited as it allows for a more precise reconstruction of the kinematics of the proton [52]. A run with such optics has however not been prioritized in ATLAS.

3.4 Collision of bunches

Most analyses (including the present) are concerned with the details of the collisions. One needs to know the center of mass energy s of the collision which is determined by the acceleration. Then one needs to know the luminosity (introduced in Section 1.2) as a measure for the number of collisions per unit time per unit area.

Luminosity

By determining the number of particles in each beam N_A and N_B, and the width of the beam profile σ_x and σ_y, one can calculate the luminosity as [53]

$$\mathcal{L} = f_r \frac{N_A N_B}{4\pi\sigma_x\sigma_y}, \tag{3.2}$$

In ATLAS the luminosity can be inferred with a precision of $\sigma_{\mathcal{L}}/\mathcal{L} \pm 1.8\%$ (for 7 TeV data) [54].

Determining the number of particles revolving The number of particles revolving is determined by measuring the current induced by each beam. As all particles contribute to the current, not just those in the nominal bunches delivering luminosity, there is some ambiguity in this measurement [53]. This is however still the most precise measure, and in ATLAS it is possible to determine the circulating current to a precision of $< 1\%$ [55].

Determining the beam width The method used to determine the bunch width giving the cited precision is the *van der Meer* scan. It measures the cross sectional area of the two beams by sweeping them past each other. By preparing the beams as symmetric and Gaussian as possible one can assume that $\sigma_x \approx \sigma_y$, and the width of the beam profile, can be determined from the correlation between the activity in the detector and the relative position of the two beams [56]. The van der Meer scan is done in specific runs, and the measurements are used to calibrate the detector such that a given activity can be related to a given luminosity.

Pile-Up

In normal runs there are on average 9(20) interactions per bunch crossing (BC) at 7(8) TeV. This is perfect when looking for rare interactions, though the *pile-up* (the multiple collision in one BC) makes it more difficult to identify from which interaction a given signal came. A lot of work is naturally put into this, though the pile-up is very low in the runs considered in this thesis, as the number of interactions per BC is reduced a lot.

Collision probability The probability to observe a collision at the IP at each BC is indicated with the parameter μ. It is calculated from the beam setup parameters as [57]

$$\mu = \frac{\mathcal{L}\sigma_{\text{vis}}}{n_b f_r}, \tag{3.3}$$

when n_b bunches are crossing and assuming certain values for the cross section of visible processes σ_{vis} [58]. For the low $\langle\mu\rangle$ runs considered in this thesis, it is a good measure for the probability of pile up, which poses a problem for the ALFA detector (see Section 5.4).

3.5 Cleaning the beams

A number of beam scraping devices, called collimators, are installed in sector 3 and 7 of the LHC in order to clean the beams, such that they remain as localized as possible. Because ALFA is operating inside the beam pipe, it is necessary to understand that a signal can come from something else than the expected beam.

Beam background

Machine induced beam background (or simply beam background) refers to interactions not arising from the beam-beam crossing, but instead from interactions with the machine aperture or beam gas. Understanding the beam background is naturally important when measuring particles in the beam pipe.

Beam halo The beam is accompanied by a halo of particles deviating significantly from the beam orbit, though still accelerated to full beam energy. Even though collimation systems are installed along LHC, the beam halo can not be removed completely.

Beam gas In order to let the protons move around the LHC freely, nearly all atmospheric air is pumped out of the beam pipes, leaving a nearly perfect vacuum (about 10^{-10}bar[46]). As the vacuum can never get completely perfect, interactions of the beam with a gas molecule can happen. These collision will normally create forwardly boosted particles, since the gas molecules will be at rest.

Beam Loss Monitors

Beam loss monitors (BLMs) are installed as part of the system preventing magnet quenches. Their intended use is to check for instabilities in the beam which are resulting in particles hitting the wall of the beam pipe, creating particle showers that are hitting the BLMs, which, at a given threshold, initiate a beam dump. The relevance of the BLMs for this thesis shall be their use as guides for aligning the ALFA Roman Pots to the beam (see Section 5.2).

4

The ATLAS detector

At point 1 of the LHC accelerator ring A Toroidal LHC AparatuS (ATLAS) is located, as mentioned in the proceeding chapter. ATLAS is a general purpose particle detector, built to discover new physics. The data studied in the thesis is collected by ATLAS, and therefore the different parts of detector shall here be presented. Furthermore, a large part of the Minimum Bias Analysis focuses on the performance of ATLAS, and as such more details shall be given on the parts relevant to this study. This chapter is based on Ref. [59], unless explicitly noted.

As seen on Figure 4.1, ATLAS is built as a conventional layered detector. Non-destructive detectors are installed at the innermost layers, taking care of tracking the particles, and measuring the momentum using the applied magnetic field in the detector. Further out calorimeters are installed to measure the total energy of the particles. The outer most layer is a muon spectrometer, discriminating muons from other particles (as they most probably go right through the calorimeters), and serves as a second tracking for the muons. ATLAS is built to be forward-backward symmetric with respect to the interaction point.

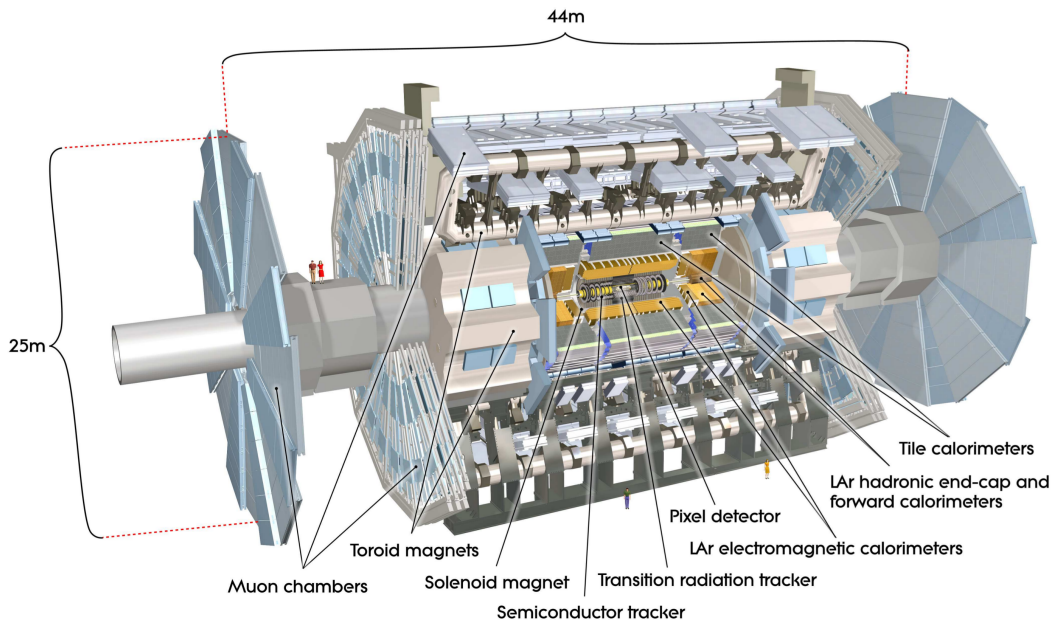

Figure 4.1: The ATLAS detector and its components. The detector measures 25 m in height and 44 m in length. The overall weight of the detector is $\sim$ 7000 ton [59].

4.1 Geometry and definitions

Before going into details with the different sub detector systems, a run through the geometry and definitions is necessary. Unless otherwise noted, the coordinate system used in this thesis will be that of the ATLAS detector. The ATLAS coordinate system uses the nominal interaction point (i.e. the center of the detector) as the origin. The z-axis is set along the beam pipe in the direction of beam 2. The $(x-y)$ plane lies perpendicular to the beam pipe, with x pointing towards the center of the LHC, and y pointing upwards. The radial coordinate $R = \sqrt{x^2 + y^2}$ is introduced and used as well. The ATLAS A-side is the positive z side, and the C-side is accordingly on the negative z side. The azimuthal angle ϕ is measured around z, from the x-axis towards the y-axis, and the polar angle θ is the angle from the z-axis towards the y-axis. Often it will be assessed by the pseudo-rapidity defined as:

$$\eta = -\ln\tan\left(\frac{\theta}{2}\right). \tag{4.1}$$

In terms of the momentum of the particle, one can write the pseudo-rapidity as:

$$\eta = \frac{1}{2}\ln\tan\left(\frac{|\mathbf{p}| + p_z}{|\mathbf{p}| - p_z}\right). \tag{4.2}$$

For approximately massless particles (i.e. light or moving with the speed of light), the pseudo-rapidity is approximately the rapidity y introduced in Section 2.6. The (pseudo) rapidity is favored over θ as particles tend to be produced uniformly with respect to the rapidity [60], and as it is additive independent on boosts, as discussed previously.

It is customary to work with the momentum and energy transverse to the beam pipe, such that we define

$$p_T = \sqrt{p_x^2 + p_y^2} = p\sin(\theta), \tag{4.3}$$

$$E_T = \sqrt{m^2 + p_T^2}. \tag{4.4}$$

4.2 Magnetic system

Ensuring the bending of the particle trajectories through the detector, the tracking detectors are surrounded by a solenoid magnet, providing a 2 T magnet field parallel to the beam pipe, while providing a minimal field in the calorimeters. The solenoid is a superconducting magnet in order to be as thin as possible (to interfere the least with the particles flying through) and in order to provide as strong a field as possible (to deflect the particles enough that the curvature of their trajectories will be visible in the inner detector). The strong field makes particle with $p_T \lesssim 400$ MeV loop around the beam pipe, thus not leaving as clear a signal in the calorimeters.

Further out the toroidal magnet system, consisting of 8 superconducting coils in the barrel and the end cap, both applies average fields of 4 T, both in the ϕ direction. This deflects the high momentum muons in the η direction, to be measured by the muon system.

4.3 Inner detector

The Inner Detector (ID) is capable of tracking charged particles going through the detector within $|\eta| < 2.5$. First of all the tracking makes it possible to extrapolate the particle

trajectories back to the vertex they originate from, and thereby see which particles were part of the process. Secondly, the p_T and the charge of the particles can be determined from measuring the radius and direction of curvature of the trajectory in the magnetic field, knowing the particle mass from subsequent particle identification.

As seen on Figure 4.2, the ID is composed of 3 different sub detectors. The first two detectors are silicon detectors, whereas the third system is a straw-tube detector with transition radiation capabilities for electron identification.

The ID is kept as light a possible (in terms of material) to interfere the least with the particles before they arrive at the calorimeters. However, besides the sensitive detector components, electrical services and cooling structures also constitute sources of potential signal losses. These services are all contained in *patch panels* each covering a quarter of the required services at each end of the pixel detector (see Figure 4.2). The loss of particles in the inactive material is among others studied by the Minimum Bias Analysis, as will be apparent from the discussion in Section 7.4.

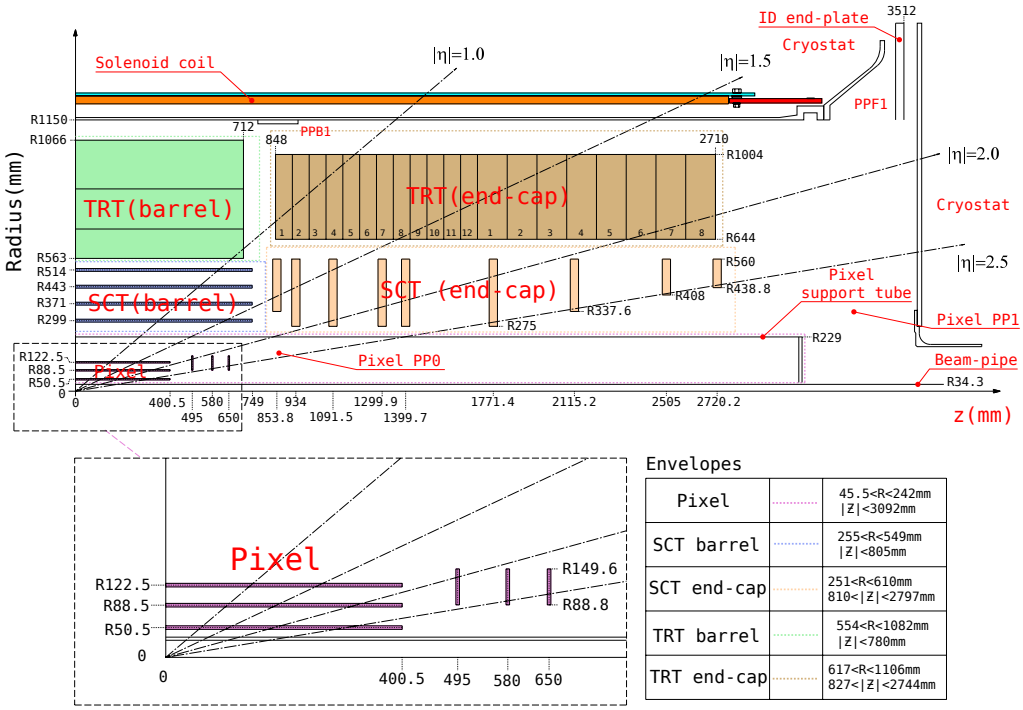

Figure 4.2: The detailed description of a quarter of inner detectors in ATLAS, showing the details of the major detector elements. The labels PPX indicates the patch-panels for the inner detector services (modified from Ref. [59] to include the patch panel PP0 as presented in Ref. [61]).

Pixel

Closest to the beam pipe, the silicon pixel detector is placed, named so for its fine granularity. It is arranged in 3 cylindrical layers in the barrel region ($0 < |\eta| < 1.7$), and three vertical disks in the end cap ($1.7 < |\eta| < 2.5$). Each pixel has a minimum size of $50 \times 400\mu$m in $(R - \phi) \times z$, leading to a resolution of 10 μm in $(R - \phi)$ and 115 μm in z. The silicon is doped with a material such that a depletion zone is created, which is enlarged by applying a voltage over the cell. A charged particle traversing the pixel sensor loses energy due to ionization and creates multiple electron-hole pairs, which drift towards the electrodes, giving a current which signals a *hit* [62].

B-layer The innermost layer of the pixel detector shall also be referred to as the *B-layer*, as it is the crucial layer for reconstructing the vertices of the decays of b quarks and other short lived particles. The B-layer is so close to the collisions that these particles are detected before they decay. Thus the decay products can be distinguished from the mother particles, using the secondary vertex.

SCT

In the SemiConductor Tracker (SCT), silicon strips are detecting particles using the same principle as in the silicon pixel detector. In the barrel region ($0 < |\eta| < 1.7$) there are four layers of stereo strips crossing with 40 mrad. In the end cap ($1.7 < |\eta| < 2.5$) 9 vertical disks with radial strips, also crossed at 40 mrad, are placed. For the entire SCT detector the resolution is 17 μm in $R - \phi$ and 580 μm in z.

TRT

In the Transition Radiation Tracker (TRT) a large number of gas filled straws (with radii of 2 mm) ensures tracking out to $|\eta| < 2$. The straws are filled with a gas mixture of 70% Xe, 27% CO_2 and 3% O_2 (from 2015 the Xe will be replaced by Ar) and a thin gold plated tungsten wire in the middle. A voltage drop from the straw to the wire means that gas particles, ionized from the passage of a charged particle, drifts to the wire, delivering a current, signaling a hit. Typically a track will have $\sim$ 36 hits in the TRT, each giving information on the $R - \phi$ position with a resolution of 130μm. The straws are directed parallel to the beam pipe in the barrel region and radially in the end caps. Furthermore, the TRT exploits that transition radiation can occur when a charged particle passes through adjacent material layers of different refractive index. The probability for transition radiation increases with the relativistic γ factor of the particle [63]. An ultra-relativistic particle traversing the TRT emits transition radiation, in the form of x-rays, which is very well absorbed by Xe. This results in a much larger readout from the straws, whereby a distinction between electrons and heavier particles can be made.

4.4 Calorimetry

The calorimeters can measure the energy of a particle by completely absorbing it. As can be seen on Figure 4.3, ATLAS uses two different calorimeter systems, for particles producing either electromagnetic or hadronic showers, but they are both built as sampling calorimeters with alternating layers of high density absorbers and layers with active detection. The dense material will cause the particles to lose energy and shower, and the sampling layers record the signal from the resulting particle shower, from which the energy of the particle can be inferred. The calorimeters in ATLAS cover the range of $|\eta| < 4.9$. Furthermore, the calorimeters have been shown to be sufficiently thick (in terms of interactions lengths) to significantly suppress *punch through*, i.e. primary particles for which the hadronic showers are not fully contained in the calorimeter.

Electromagnetic calorimeter

The innermost calorimeter is the electromagnetic (EM) calorimeter, mainly responsible for measuring the energy of electrons, positrons and photons, as these interact electromagnetically with the material. The most dominant effect of energy loss of electrons

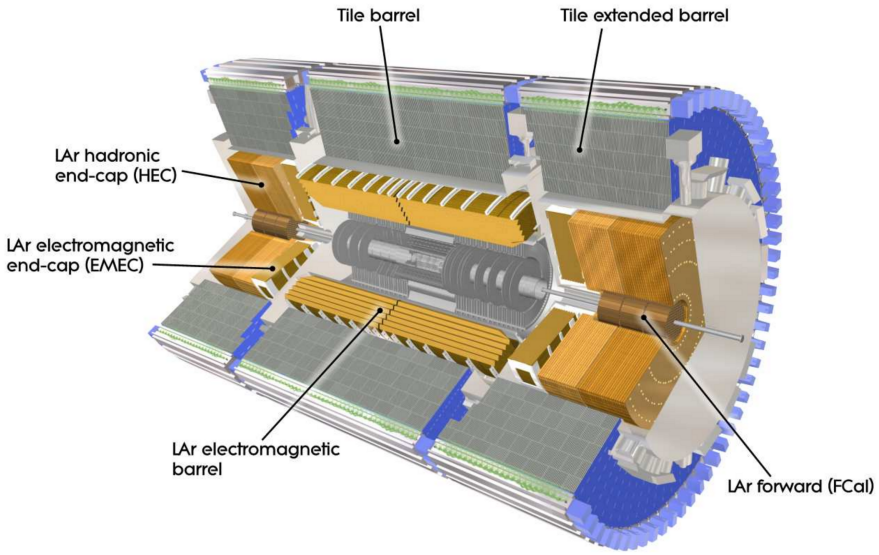

Figure 4.3: The ATLAS Calorimeters [59].

traversing through matter is bremsstrahlung: The acceleration of the electron by the nucleus results in it radiating off a photon (an effect only important for electrons as the effect is $\propto 1/M_{incident}$)[63]. The most dominant effects for photons with $E_\gamma \gtrsim 1$ MeV is production of electron-positron pairs [64]. The combined effect of bremsstrahlung and pair production results in the formation of an electromagnetic shower. One can assume that the number of particles increase until the particles reach a critical energy E_c, when the energy is too low for pair production, where the development of the shower will stop [65]. At this point the initial energy E_0 can be inferred from number of particles produced as $N_{\max} = E_0/E_c$ [63]. In the EM calorimeter of ATLAS, accordion shaped lead absorbers are interleaved with liquid argon (LAr) drift chambers. Lead is used for faster shower development, as cross section for bremsstrahlung increases with density [63]. Using liquid argon makes the detector very radiation resilient, as the LAr can be changed when too ionized. The accordion geometry gives the detector full and symmetric coverage in ϕ, whereas in η the detector is divided in cells. The energy deposit is read out for one $(\phi - \eta)$ segment and up to 4 segments in R, and related to the number of particles in that segment (estimated from calibration). The EM calorimeter consists of two cylinders in the barrel ($0.1 < |\eta| < 1.475$) and a wheel in each end cap ($1.375 < |\eta| < 3.2$). Details of the granularity is given in Ref. [59], but is in general decreasing for higher R. For $|\eta| < 1.8$ a presampler in front of the sampling layers is used to correct for energy lost in the inner systems. The energy resolution has been found to be $\sigma(E)/E = (10.1\%/\sqrt{E}) \oplus 0.17\%$ for $|\eta| < 3.2$, where the first term is the sampling uncertainty and the second term is due to non-uniformities in the detector.

Hadron calorimeters

A tile calorimeter is used as hadron calorimeter in the barrel ($|\eta| < 1$) and in the extended barrel ($0.8 < |\eta| < 1.7$), and a LAr calorimeter is used in the Hadronic Endcap Calorimeter (HEC) ($1.5 < |\eta| < 3.2$) as well as in the Forward Calorimeter (FCAL) ($3.1 < |\eta| < 4.9$). The tile calorimeter uses a steel absorber and plastic scintillating tiles as active detectors. Hadronic interactions are more complex than electromagnetic showers, as the energy is lost via secondary proton ionization, electromagnetic cascades from secondary π^0 particles

or by breaking up nuclei producing neutrinos and secondary $\pi^{\pm}$ (constituting $\sim 80\%$ of the most common ways a hadron loses its energy) [66]. The secondary particles created in the steel layers are subsequently measured when they pass through the plastic scintillators, where the charged particles produce light, which is collected, read out and used as a measure of the energy deposit (by correlating to calibration). The tile calorimeter is segmented in 64 parts in ϕ, and grouped in η such that one group occupies one part of the solid angle.

The HEC consists of two wheels on each side of ATLAS, placed directly behind the EM calorimeter end caps. Each wheel is built from 32 wedge shaped modules in ϕ and in two parts in z, using parallel copper plates as the absorber and LAr as the active sampling material. The copper plates are better suited to ensure mechanical stability, and for better cooling in this region of higher activity. The energy resolution on hadronic jets is found in the barrel and end cap to be $\sigma(E)/E = (50\%/\sqrt{E}) \oplus 3\%$ for $|\eta| < 3.2$.

The FCAL is divided into 3 parts, the first is using copper optimized for electromagnetic showers, and the next two use tungsten, as this has good thermo conductive properties, as well as making sure to absorb all the energy, protecting the magnets behind the FCAL. In all 3 parts, LAr drift tubes are used as the sampling layer, in order to cope with the extreme radiation. The energy resolution on hadronic jets in the FCAL is found to be $\sigma(E)/E = 100\%/\sqrt{E} \oplus 10\%$ for $3.1 < |\eta| < 4.9$.

4.5 Muon system

The muon spectrometer covers a combination of triggering and an additional momentum measurements of the muons going all the way through the detector. The Monitored Drift Tubes (MDT) are drift tubes using aluminum tubes and an Ar gas mixture. The tubes are oriented orthogonal to the beam pipe, since the field from the toroidal magnet system is running along ϕ. The use of tubes enables flexible designs and redundancy in number of elements, since one missing tube has little effect on the overall efficiency. Each straw has a resolution of 60μm. The MDTs are limited by a restitution time close to 750 ns (due to radii of 15 mm). Therefore Cathode Strip Chambers (CSCs) are used in areas with high counting rates, i.e. extreme radiation. The CSCs are multi wire proportional chambers with the cathode segmented in strips, since this gives a better spatial resolution [63]. The Resistive Plate Chambers (RPC) used in the barrel and Thin Gap Chambers (TGC) in the end cap region serve as triggers for the muon system by BCID, and provide p_T thresholds. Further they supply the second coordinate orthogonal to that of the tracking elements.

4.6 Forward detectors - high η

ATLAS has different sub detectors with focus on the extreme forward region.

LUCID

Positioned at ± 17 m from the interaction point sits the LUminosity measurement using Cherenkov Integrating Detector (LUCID). Built to measure the luminosity, it exploits the Cherenkov radiation delivered by particles going through the detector. Since 2011 it only uses the glass of the photo multipliers for Cherenkov radiation [67].

ZDC

The Zero-Degree Calorimeter (ZDC) is responsible for measuring the centrality in heavy ion collisions. It is located at ±140 m from the interaction point just behind the point where the single straight segment beam pipe from the interaction point splits in two. The magnets bending the beam into the separate beam pipe, makes the ZDC a detector for neutral particles. It spans the very forward region ($|\eta| > 8.2$), and is a sampling calorimeter with tungsten as absorber and quartz rods as active sampling material.

ALFA

As the ALFA detector is used extensively in the work covered this thesis, Chapter 5 is dedicated to the description of this sub detector.

4.7 Triggering and data acquisition

At nominal intensity, the LHC is expected to deliver BCs at a frequency of 40 MHz. With an expected 25 collisions at every crossing, a lot of raw data is produced.

The ATLAS detector has a maximal read out frequency of 75 kHz, though the storage systems can only handle data at 400 Hz, so a fast and efficient selection is needed. This is handled by the Trigger and Data Acquisition (TDAQ) system.

Luminosity block Since the conditions for the TDAQ and the instantaneous luminosity vary with time, ATLAS uses *luminosity blocks*, time intervals of $\sim$ 60 s, where the conditions can be assumed to be approximately equal. The luminosity blocks (LBs) are also useful for indicating which parts of the data have been determined to have good data quality and can be used for analysis, and which parts of the data are of bad quality and should be excluded.

Trigger system

Not every event is of interest for a given analysis. In order to collect datasets containing mostly interesting events, ATLAS uses a trigger system. The trigger system in ATLAS is divided in three levels with each level being more specific than the previous.

The first level (L1) trigger is implemented in the hardware as it is fed information from specific trigger units on the sub detectors (e.g. the MBTS or the trigger tiles of ALFA), or reduced granularity calorimeter information (usually based on signatures like high p_T muons, electrons, etc.). The L1 trigger also defines a number of "Region of Interest" (RoI), a geographical region that might be interesting. The L1 trigger reduces the rate of events to $\sim$ 75 kHz. At the second level (L2) trigger, the RoIs are analyzed with the full detector information available, typically reducing the rate to $\sim$ 3.5 kHz. The last level, the Event Filter (EF), uses the entire event topology to further select events, reducing the rate to $\sim$ 400 Hz in normal runs. However, a rate of up to 1kHz has been achieved in special runs with ALFA, where the events size is reduced [68].

The trigger information is processed by the Central Trigger Processor (CTP). For each a *trigger menu* with different combinations of trigger selections is implemented. To use the readout bandwidth optimally, one uses *prescales* on trigger menu items with too high rate or lower priority. A prescale of a means that only every a-th event fulfilling that trigger menu item will be saved. An event fulfilling one trigger menu item can also be recorded because it fulfills a second trigger menu item. In order to account correctly for

prescaling, it is important to distinguish between whether a trigger item was just fulfilled, or it was making the decision to read out the event.

Bunch groups Besides the specific combination of triggers, the CTP trigger items are also set, only to trigger on bunches in specific bunch groups (BGRP), defined as follows:

BGRP 0 BCRVeto: Every bunch except 3540-3560 (abort gap), when the bunch counter reset signal is sent.

BGRP 1 Paired: Paired (colliding) bunches, used for physics.

BGRP 2 CalReq: Calibration request for bunches in the abort gap.

BGRP 3 Empty: Empty bunches separated by 5 bunches from filled bunch.

BGRP 4 Isolated unpaired: Unpaired bunches separated by at least 3 bunches from a filled bunch in the other beam.

BGRP 5 Nonisolated unpaired: Unpaired bunches not categorized in BGRP 4.

BGRP 6 Empty after paired: Empty bunches not categorized in BGRP 3.

BGRP 7 Special: To be set manually for special runs.

The bunch group configuration, specifying which bunches are put in which BGRP, is normally fixed, but it can be changed throughout the run.

MBTS Most sub detectors have dedicated trigger systems, though the Minimum Bias Trigger Scintillator (MBTS) is not associated to a specific sub system, but was installed in order to check and refine the dead, noisy and faulty channel maps of ATLAS in the commissioning phase of LHC. The MBTS consists of an outer ring ($2.09 < |\eta| < 2.83$) and an inner ring ($2.83 < |\eta| < 3.84$), situated between the inner detectors and the LAr End cap, at a distance of 3.6 m from the IP, on either side [69]. Each ring is divided into 8 trapezoidal plastic scintillators with a thickness of 2 cm each. Light emitted by the passage of charged particles through the scintillators is collected by wavelength shifting optical fibers to individual PMTs. Energy deposits above threshold (50 mV/0.23 pC [70]) results in the trigger item `L1_MBTS_1` being true.

As the MBTS is a very inclusive trigger, the data sample that fulfills the MBTS trigger is called minimum bias data, as it is the least biased data sample in ATLAS. As will be presented in Chapter 7, the analysis of these data still helps in detecting inconsistencies in the geometry of the detector, as well as keeping the MC simulations updated to match data.

Data handling

If an event passes the L1 trigger, each detector sends information from their front end electronic to ReadOut Drivers (ROD). The data is sent from there into the data acquisition (DAQ) system, firstly to be used in the L2 trigger decision, and if accepted it is transferred to event building systems for use in the EF. Events selected by the EF are moved to the permanent storage at the CERN computer center, in the *RAW* format (the file format containing most detailed information of the events).

In order to handle the enormous amount of data produced, a network structure called Worldwide LHC Computing Grid (or simply The Grid) connects physics sites all over the

world for processing and storage of files. The Grid has a tiered structure, with CERN being Tier 0, handling the raw data. At the 13 Tier 1 sites subsets of the raw data is stored, and calibration and processing of data is done. At around 140 Tier 2 sites physics and simulations tasks are done. Most physics institutes use a computing farm, that can constitute a Tier 3.

The data can be processed into increasingly abstract objects, facilitating further analysis. For the work done in this thesis, most data has been prepared in the format of *NTuples*. NTuples have a tree structure with the abstract information of each track for each event on position, energy etc., instead of the raw information of hits and energy deposits in the detector. The intermediate formats have not been used.

Underlying event In an event with some process of interest, only one parton from each hadron interacts to produce the given final state. Everything else than the signature from this process is named the *underlying event*. The hadron remnants can also subsequently scatter on each other, producing *multiple parton interactions* (MPI), which complicates the tracking even further. The underlying event consist of both hard and soft processes, and at least the soft processes might be better modeled using the results of the Minimum Bias Analysis discussed in Chapter 7.

4.8 Simulating the experiment

In order to look for deviations between expectations and actual behavior of the experiment, computer simulations are used. Also some investigations, such as some systematic uncertainties, are only possible using simulations. The author has not been working with simulating the experiments, and as such no details of the simulation infrastructure shall here be given.

Monte Carlo event generators

The expected behavior is modeled by running Monte Carlo (MC) simulations of proton-proton collisions, using various methods to produce the events of interest, from very inclusive to specific exclusive processes. In the work on Minimum Bias data, comparisons have been done to Pythia 6 [44] (AMBT2BCTEQ6L1 tune), Pythia 8 [45] (A2MSTW2008LO tune) and Epos [71] (standard tune) event generators. The tuning of these MC generators, in order for the MC samples to match data obtained from the experiment, plays a crucial role.

For the work on diffraction, Pythia 8 (A2MSTW2008LO tune) has been used to generate the MC samples available.

Detector simulation

The particles resulting from the MC generator are subsequently propagated through a model of the detector, including the magnetic fields, simulating the physics interactions as well as the detector response. To simulate the passage of the particles through ATLAS, GEANT4 [72] is currently used. GEANT4 simulates the effects of particle-matter interactions, which occur when the particles traverse the materials of the detector, in great detail. The ATLAS detector is described in GEANT4 by a *GEO model* which is periodically updated by the ATLAS Material Working Group. The important role of an accurate detector description, exemplified by the discovery and implications of discrepancies between MC and data, will be discussed in Chapter 7.

5

ALFA

Absolute Luminosity For ATLAS (ALFA) consists of eight identical tracking detectors, installed 237 m and 241 m from IP on either side of ATLAS in the LHC tunnel, pairwise above and below the beam pipe. In Figure 5.1 the position of the eight ALFA detectors is presented with the numbering convention of this thesis (used as a more simplistic alternative to the ATLAS naming convention used elsewhere). In this chapter a description of ALFA shall be given, going into more detail with the parts needed for understanding the work presented later in the thesis. Unless otherwise mentioned, the information is based on [73].

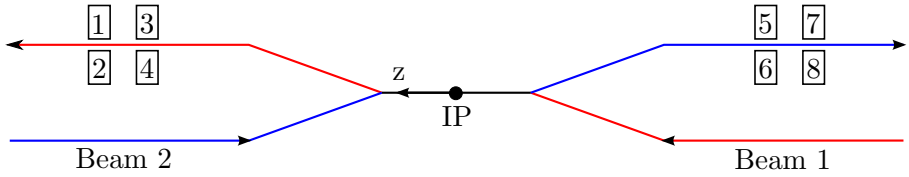

Figure 5.1: Position of the ALFA detector stations relative to the beams, presented with the numbering scheme applied in this thesis.

5.1 Detector

The ALFA detector is using scintillating fibers to detect charged particles. The main detector (MD) is constructed with 10 pairs of 64 fibers oriented in two projections (named U and V) perpendicular to each other, in order to be able to determine a spacial coordinate. The fibers are installed with a 45 degree angle to the horizontal line such that the detector can go as close as possible to the beam. On Figure 5.2 the concept of the MD layering is shown for four pairs, indicating the diamond shape of the active detector area.

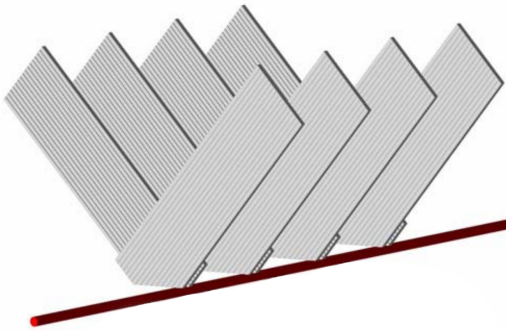

Figure 5.2: Schematic view of the perpendicular layering of the main detector, exemplified with four pairs of fibers [73].

The scintillating fibers are squared, measuring 0.5×0.5 mm with a trapping efficiency of 4.2% and are coated with a thin layer of aluminum to prevent optical cross talk of the scintillator light [74]. Each layer of fibers are glued onto a thin titanium plate for stability, though in the active detector area the fibers are glued onto 170 μm of G10 substrate, as this material has a rather low density and thus interferes less with the protons.

In addition, 3 layers of 30 fibers constitutes each of the overlap detectors (OD) situated on either side of the MD. The fibers for the OD and 24 of the fibers of the MD are coated on the ends that do not connect to a PMT to increase light yield. The 40 fibers of the MD which are cut in a 45 degree angle do not have a coating, as it was found not to be needed for those [73].

In order to obtain a better resolution, the 10 layers are shifted by 1/10 of the fiber diameter with respect to each other. The resolution on the x-position of a particle was in principle expected to be 14.4μm (see Appendix A.3), though after various test beam runs, it was found that the MD could ensure a spacial resolution of $\sim 30\mu$m [75, 76, 77, 12].

The fibers are read out by Multi Anode Photo Multiplier Tubes (MAPMT), with 64 channels each. In order to avoid the inevitable cross talk, the fibers are matched such that neighboring fibers on the MAPMT are not neighbors on the detector. On Figure 5.4 the ALFA detector is depicted installed in a Roman Pot (see Section 5.2).

Track reconstruction

The tracking algorithm requires ≥ 3 accepted layers of both the U and V projection to have enough points to track the particle. Each layer can only be used if ≤ 3 fibers are hit, otherwise the layer is ignored. The layer efficiency has from tests been found to be $\sim 92\%$ [12].

Knowing the position of the fibers in the detector (the *metrology*), the fibers with signal are projected onto a one dimensional array as shown in Figure 5.3. This is done for both the U and V projection, and by combining the two projections, the position of the track in the 2D plane of the MD can be inferred. If more than one particle traverse the detector,

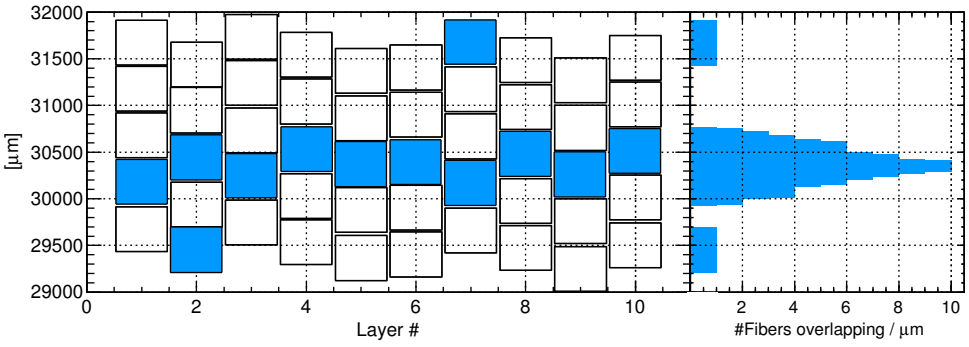

Figure 5.3: The fiber hits are translated into a one dimensional histogram for the position of the path for each projection [12].

more paths will be detected on each projections, giving multiple combinations, leading to more candidates, than there were actually particles going through. This can however not be avoided when only two coordinates are measured. Unfortunately there has been introduced a limitation of 10 track candidates in the track reconstruction algorithm [12], which can be problematic for events with multiple particles going through the detector.

In the rest of the thesis the following convention shall be used to characterize tracks. The x-coordinate of a track in a given armlet, in the ALFA station closest or furthest from the IP, is denoted by x_{inner} and x_{outer} respectively. The angle of the track to the beam axis, θ_x shall be approximated by the slope between the two consecutive ALFA detectors, such that

$$\theta_x = \frac{x_{\text{outer}} - x_{\text{inner}}}{d_{\text{RP}}}, \tag{5.1}$$

where $d_{\text{RP}} = 4160$ mm is the distance between two consecutive ALFA detectors. Similarly for the y-coordinate.

Electronics

The signals from the fiber channels in the MAPMT are sent to the MultiAnode Read-Out Chip (MAROC), where they are amplified (normalizing the difference in the signal strengths), then they are shaped, and discriminated at a preset fixed threshold, sending out a 0 or 1, depending on whether the signal was under or over the threshold [78].

The MAROCS are part of the Photo Multiplier Frontends (PMF) sitting on each MAPMT. The output from the 23 PMFs is handled by a motherboard. The motherboard is the gateway between the MAROCs and the DAQ, as the motherboard is responsible for sending the fiber hit information through the RODs to the DAQ if it receives a trigger from CTP. Moreover, it is used to change or monitor values (thresholds, gain factors, voltages, etc.) for the MAROCs. More detail on the propagation of the signals between ALFA and ATLAS can be found in [79].

5.2 Mechanics

The main purpose of the ALFA detectors is to detect particles flying close to the beam, therefore the detectors must be able to move into the beam pipe.

Roman Pots

Because of the ultra high vacuum in the LHC, only equipment that does not pollute the vacuum can be used. As the glue in the ALFA detectors might evaporate, each detector is installed in a *Roman Pot* [80, 81, 30]. The ALFA Roman Pot is shown on Figure 5.4, with the ALFA detector installed. Inside the Roman Pot there will be applied a secondary vacuum, ensuring the use of a 200(500) μm thin wall under(in front of) the MD, for minimal interference with the incoming protons.

Movement

The Roman Pots are installed in separate bellows, that allow them to move towards the beam independently of each other. To compensate for gravity and the suction from the vacuum, compensating bellows and springs are installed to ensure retraction in case of a power failure. The motors moving the roman pots have a minimum movement of 5 μm [78].

Alignment

Online the position of the roman pots are monitored with Linear Variable Displacement Transducers (LVDT), radiation hard detectors that can determine the coarse position of the roman pots relative to the station, i.e. the beam pipe. The roman pots are positioned

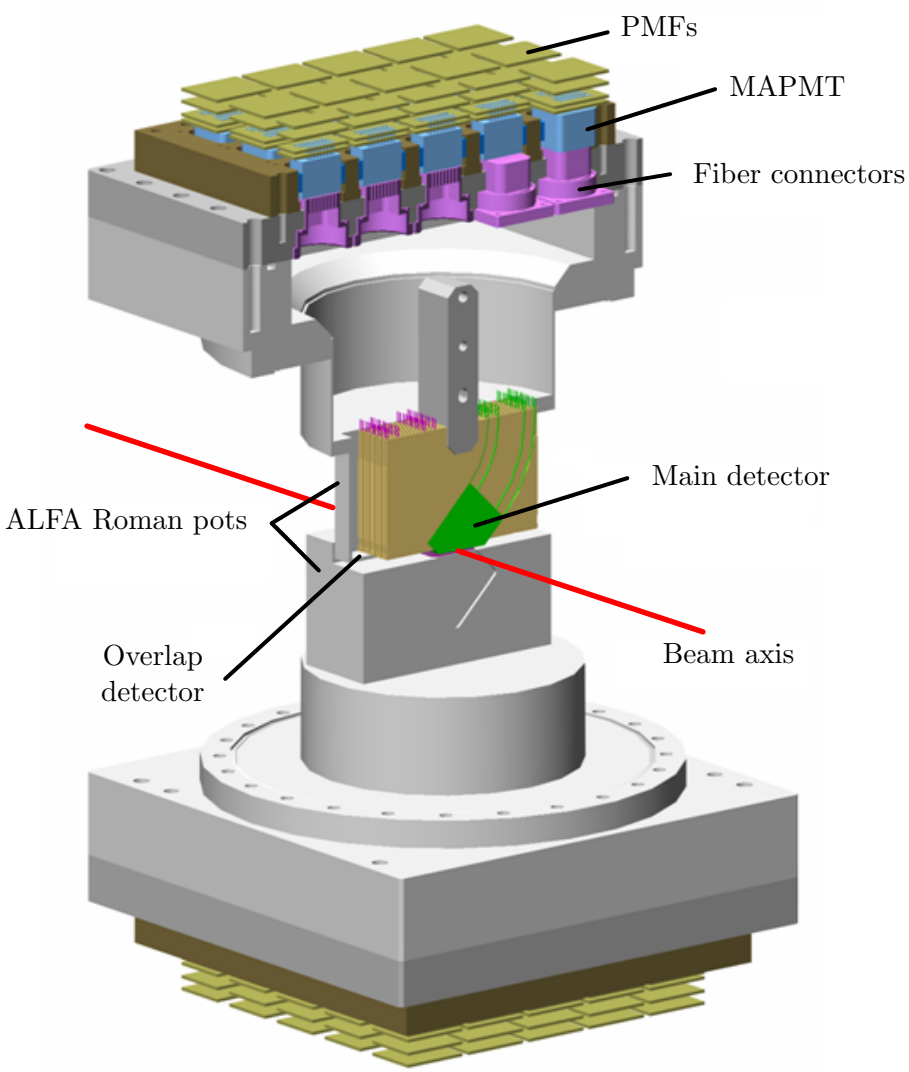

Figure 5.4: A cut through the ALFA detector [77].

relative to the beam by using the BLMs. One at a time, a detector is moved towards the beam, resulting in a certain count in the BLMs. Noting the position that for each detector give similar counts, each Roman Pot is coarsely aligned to the beam.

Offline the tracks in the OD is used to measure the distance of the upper detector to the lower detector with a resolution of $< 10\mu$m [82]. This first vertical alignment of the detector has to be refined. First the horizontal alignment, and possible rotation of the detector coordinate system is done in various steps using the signature of elastic events in the detector. Then the vertical alignment is fine tuned to one of the ALFA stations using again a sample of elastic events (the details of the alignment can be found in [12]).

5.3 Triggering

For the MD, two dedicated 3mm thick plastic scintillator tiles are used, in order to make local coincidence. They are covering the overlapping area of the MD fibers, and painted white to maximize the light yield [83]. For the OD, only one trigger tile per side is used, covering the intended active area of the OD. In the remainder of the thesis the trigger in ALFA shall refer only to the trigger tiles by the MD.

All the ALFA detectors are constructed the same, but the ODs of the upper and the lower detector must to be able to pass each other. The only possible configuration results in a different order of the MD and the trigger tiles relative to the IP in the eight ALFA detectors. Thus in ALFA detectors 1, 3, 6 and 8 a particle pass through the MD *before* the trigger tiles, and vice versa in ALFA detectors 2, 4, 5 and 7. The effect of this shall be apparent from the performance studies of ALFA discussed in the following chapter.

The signals from the trigger tiles are carried to round PMTs by round multicladded clear fibers functioning as lightguides [78]. The *trigger mezzanine* is handling the trigger signals. It houses PMFs that shapes and discriminate the signal from the trigger PMTs [84]. After the discrimination, the trigger signals from the two MD trigger tiles are send through a logic, sending out 1 only if both trigger tiles fired. At USA15 the signals are reshaped and discriminated and split into two outputs, with one of them going to the CTP unit for integration in the ATLAS combined triggering, and the other goes into the ALFA standalone trigger system (this will not be relevant in this thesis, see Ref. [84] for details).

The latency for the ALFA trigger signals is 2157 ns (mainly due to the flight time of the protons from IP to ALFA, and the following transport of the trigger signal in the opposite direction) [85]. This is longer than in ordinary *pp*-runs where the ATLAS trigger latency is 1575 ns, and the longer latency means that the muon trigger can not be exploited in the runs with ALFA trigger.

Trigger items of interest

Throughout the thesis, there will be referred to trigger menu items, which shall be described here. The item `L1_ALFA_ANY` fires every time both trigger tiles on any detector fire, i.e. the most inclusive trigger item possible. The item `L1_ALFA_ELAST15/18` fires whenever the triggers at positions 1&3&6&8/2&4&5&7 fire, corresponding to the expected elastic signature. The item `L1_ALFA_SDIFF5/6/7/8` fires whenever the triggers at positions 1&3/2&4/5&7/6&8 fire, corresponding to the track expected from a single diffractive event. The item `L1_MBTS_1(2)` fires whenever there is at least one(two) hits in the MBTS above threshold (as mentioned in Section 4.7). The item `L1_MBTS_1(2)_C/A` fires whenever the MBTS on the A/C side records at least 1(2) hits. The item `L1_ALFA_A(C)_MBTS_2_C(A)` fires whenever the MBTS for A(C) side fires simultaneous with the trigger of armlet 57 or 68(13 or 24), corresponding to the track and activity expected from a single diffractive event. Each of the mentioned items are only triggering for bunches in BGRP1.

ALFA data streams

At the L2 trigger, ALFA has a calibration stream and a physics stream. The ALFA calibration stream contains only ALFA data, and can, as mentioned, handle a rather high rate of events alongside other ATLAS partitions [84]. This means that it is possible to read out the ALFA events whenever the `L1\_ALFA\_ANY` fires, which means it is the most inclusive stream possible for ALFA. The ALFA physics stream has higher prescales on the trigger items, as triggered events request a full read out of the ATLAS detector.

When reading out ALFA the analog trigger signal for the current and 3 previous BCs are read out. This shall be exploited in the analysis of the trigger efficiency in Chapter 6.

5.4 Timing and specific runs

ALFA does not have an absolute timing of the detections, instead the electronics are read out after each BC. This means that it is not possible to timely correlate a proton track in ALFA with a specific vertex in ATLAS. Especially for this reason only runs with a very low average number of interaction per BC, $\langle\mu\rangle < 0.08$ are used for the studies discussed in this thesis.

As mentioned in Section 3.3 a high β^* optics is often adopted for studying elastic events. In general ALFA can only be used reliably in runs with luminosity lower than in normal runs due to disturbance of the electronics and too much activity in the PMTs [68]. A full list of the data sets used for the work in this thesis can be found in Appendix C.

5.5 Acceptance of ALFA

In the perfect world the ALFA detector would cover the entire solid angle. Since this is not the case, only a fraction of events will be detected by ALFA, namely that within the fiducial region of ALFA. This fraction constitutes the *acceptance* A of the detector. The anticipated distribution of the events of interest have naturally been taken into account when designing the detector, such that most events will be detected. Also it is found that it is in the gap between the upper and lower detector that the majority of events are lost [52]. However it is simply not possible to measure scattered protons here due to the beam. The acceptance regions relevant for the different processes of interest shall be discussed in the following section.

5.6 Signature in ALFA

Elastic like events

From the theory one can expect to detect elastic events by hits in the upper ALFA detectors on one side and the lower ALFA detectors on the other side, or vice versa. Corresponding to the two protons flying symmetrically away from the IP. This results in signals in either ALFA detectors 1&3&6&8 (referred to as arm 1368) or 2&4&5&7 (arm 2457) The elastic like events in arm 1368 can be depicted schematically as in Figure 5.5, ignoring the beam pipe.

The acceptance for elastic events is heavily dependent on the transferred energy squared t [12]. In the elastic analysis of the ALFA data, this dependence must be taken into account. In this thesis the acceptance of elastic cuts will not be exploited, and is thus not discussed further.

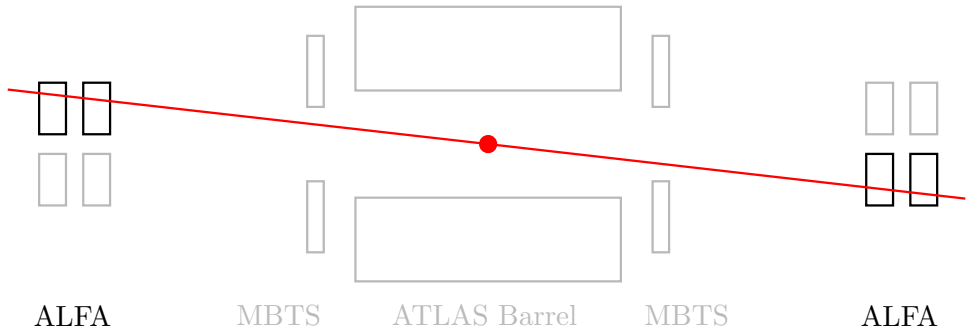

Figure 5.5: Simplified drawing of an elastic event happening at interaction point 1.

Diffractive like events

Single diffractive events are detected by the intact proton flying through two consecutive ALFA detectors, above or below, on either side. This means signals in either ALFA detectors 1&3 (armlet 13), 2&4 (armlet 24), 5&7 (armlet 57) or 6&8 (armlet 68). In Figure 5.6(a) the schematic depiction of the detection of a single diffractive event is presented. Correspondingly, the central diffractive events can be detected by hits in the ALFA detectors 1&3&5&7 (CD 1357), 1&3&6&8 (CD 1368), 2&4&5&7 (CD 2457) or 2&4&6&8 (CD 2468). Which would correspond to a detection like that in Figure 5.6(b). For both single and central diffraction it is necessary to put some constraints on the activity in ATLAS, in order to distinguish them from background events of beam halo going through the detector. The double diffractive events will not be discussed in this thesis, as the selection can not be enhanced by the use of the ALFA detector, as seen from Figure 5.6(c).

A full MC of diffractive events was not yet available by the deadline of this thesis, though using Pythia 8 (default settings), it was found that the geometrical acceptance of ALFA for single diffractive events is of the order $\sim$ 40(50)%, for the ALFA detector sitting 8(6) mm from the beam center [52].

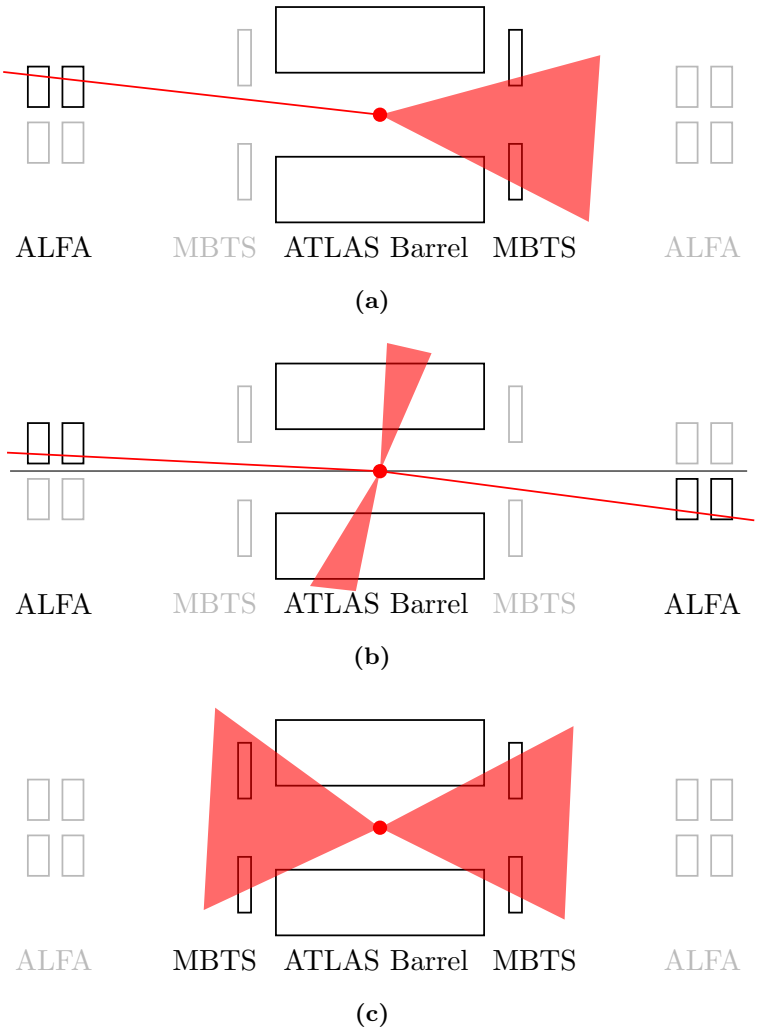

Figure 5.6: Simplified drawing of a **(a)** single diffractive event **(b)** central diffractive event **(c)** double diffractive event, happening at interaction point 1.

6

ALFA performance studies

If an event has a proton in the acceptance region of the ALFA detector, it should leave a track in the detector, that can be reconstructed and is read out by having the corresponding trigger fire. Unfortunately, this is not always the case. In this chapter the work done on determining the detector efficiency of ALFA will be presented.

6.1 Data sample

For studying the performance of ALFA, the good luminosity blocks of the dedicated ALFA run 191373, with $\beta^* = 90$ m and $\sqrt{s} = 7$ TeV, will be used. The sample is the one used in the ALFA total cross section analysis, and thus a natural choice for the performance studies. As a dedicated ALFA run, the average number of interactions is $\langle\mu\rangle < 0.004$ [86]. The ALFA calibration stream containing $\sim 54 \cdot 10^6$ events will (as the most inclusive sample) be used for the studies. In the run, one large (main) and several smaller (probe) bunches were circulating. In this analysis only the main bunch will be used. Only events with single tracks in the individual ALFA detectors will be used, unless otherwise stated.

6.2 Trigger performance study

In order to understand the number of diffractive events detected, the first step is to understand what fraction of the real events is actually recorded. Thus the performance of the trigger in ALFA shall be determined.

Event classification

Two types of events will be distinguished: elastic and single diffractive like events. As discussed in Section 5.6, the events are characterized by the pattern of tracks they are expected to leave in the ALFA detectors. Thus events with tracks in arm 1368 or 2457 shall characterize elastic events, and likewise, events with tracks in armlet 13, 24, 57 or 68 shall characterize single diffractive like events (simply referred to as diffractive events). In diffractive events, debris of the diffracted proton are expected to hit the MBTS. The trigger menu items `L1_MBTS_1` (MBTS1) and `L1_MBTS_2` (MBTS2), will be used to make a sub selection of two additional event types.

Cuts and cutflow

As mentioned, only events with at most one track per detector are used (Number of tracks cut). The events where a detector have more than one track are problematic, because it is not possible to say which track made the trigger fire. This is a rather strong cut and reduces the number of elastic like events with (29.52 ± 0.12) %, and diffractive like events with no MBTS selection cut are reduced with (18.09 ± 0.05) %. When only one type

of uncertainty it shall denote the statistical uncertainty. A cut is made to prevent edge effects (Edge cut) by removing tracks hitting the detectors $< 60\mu$m away from the edge of the detectors. The crucial point of this cut is to be sure that the fibers and the trigger plates will both be hit by the particle in question. For elastic event candidates, it reduces the total number of events by (1.36 ± 0.18) %. For the diffractive event candidates, it reduces the total number of events with (7.80 ± 0.07) %. For the elastic event candidates a requirement, making sure that two protons measured are leaving the interaction point back to back (B-to-b), will be applied. This requirement constitutes an elliptical cut in the $(x_{\text{inner}} - \theta_x)$ plane for each side, an elliptical cut in the $(x_{\text{inner}} - x_{\text{outer}})$ plane, as well as a cut outside linear cuts in $(y_{\text{inner}} - y_{\text{outer}})$ plane. The considerations on those cuts shall not be given here, as it is discussed in [12]. The back-to-back requirement reduces the number of events with (3.67 ± 0.18) %. The cutflow can be seen in Table 6.1.

Table 6.1: Number of events in the run, and the cutflow, presented for the selection of elastics and diffractive like events.

	Elastic like events	Diffractive like events		
		No MBTS sel.	MBTS1	MBTS2
All selected events	885455	5112985	562165	424173
+ Number of tracks cut	624083	4188196	462859	349692
+ Edge cut	615640	3861579	443435	338260
+ B-to-b (elastic only)	593025	-		-

Wrong triggering

Both of the main trigger tiles are supposed to trigger if there is a track in the main detector. If not, it will for this study be regarded as wrong triggering. The triggering will also be considered incorrect if the trigger fired for an earlier BC (information of the 3 previous BCs is read out, as mentioned in Section 5.3.

Possible problems in the trigger

Previous to this study, some cases have been observed, where the analog trigger signal exhibit some jitter, meaning that it might fire erroneously in the previous or following BC compared to the BC for the tracked particle [84], i.e. the triggering will be wrong. This effect could ultimately bias the number of events recorded if it happens for all the detectors the events are selected from, since the event will then not be recorded. In Section 6.3 it is shown not to be a problem for at least the elastic events.

As seen from Figure 6.1 the fraction of events with wrong triggering is below 0.1%, though for completeness it shall here be covered in some depth. The figure is showing the analog trigger information from the ALFA calibration stream, presented when demanding a logic 'and' or an 'or' between the two main trigger tiles. In the following the focus will be on triggering with a logic 'and' between the triggers, as this is what is needed for a signal to be send to the CTP. From Figure 6.1 an additional effect becomes apparent: It has previously been seen that the analog trigger signal after the MAROC2 chip is on for 500-600 ns (i.e 10-12 BCs in the runs studied), but there is only send a signal to CTP for the BC corresponding to the leading edge of the analog signal [84]. First of all, this means that it will not be possible to have new triggering in the consecutive 500-600 ns, which might prevent the triggering for an event of interest. Furthermore, a trigger in a previous BC would have send a trigger to CTP in that BC, but would still give an analog signal visible on Figure 6.1. This explains the relatively flat equal fraction of trigger in the BC

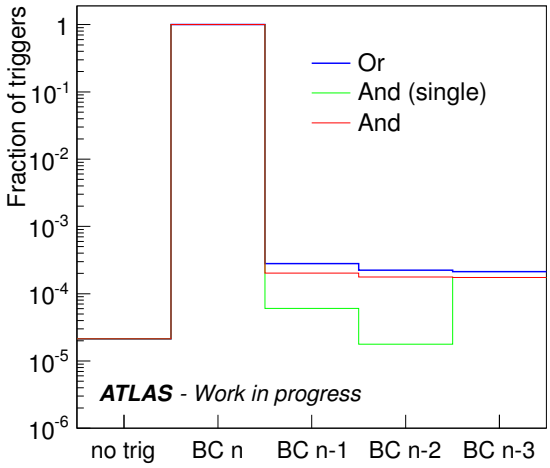

Figure 6.1: In blue (red) labeled 'Or' ('And') the fraction of elastic events where one (both) of the main trigger tiles of ALFA detector 3 fired in the correct bunch crossing n, an earlier, or not fired at all. The entry named '(single)' indicates only when the first triggering happened (No cuts applied).

n-1,2,3 bins. The "And (single)" entry shows only the earliest triggering, and the expected discrepancy is observed. Since only the previous 3 BCs are saved, the "BC n-3" entry will hold all the events with earlier triggering, explaining the significantly higher fraction in that bin. Introducing the cuts on the elastics, the same pattern is seen, only with an order of magnitude lower fraction of events with no triggering (see Appendix B.1).

Geometrical effects

In order to rule out any geometrical effect causing the wrong triggering, the hitmaps for tracks in events with wrong triggering are compared to the hitmap for the tracks in events with correct triggering. In Figure 6.2 the hitmaps for the events with good triggering are put next to the fraction of events with wrong triggering per bin. It is shown for detector 1, but similar distributions is seen for the remaining detectors (see Appendix B.2), as well as for different cuts.

For the elastic like events (Figure 6.2(a) and Figure 6.2(b)), no obvious geometrical effect seems to cause the trigger to fail. For the diffractive like events a significant amount of events with bad triggering sit either at the area with most events (to be expected), or on the edge of the detector (especially in the lower right side of the detector where the density of tracks is higher). These are most likely caused by edge effects, i.e. when the trigger tiles are not fully covering the detector.

Systematic uncertainties

A stability test of the cuts were done by calculating the efficiencies with and without the cuts. It was found that the resulting efficiencies are stable within 0.01-0.02%. The error on the alignment introduces an error on the edge position of the ALFA stations. This is of relevance to this study due to the edge cut applied. Here the full propagation of the possible alignment errors on the detectors are taken into account (as stated in [12]), and the efficiencies are calculated when all detectors are moved upwards and downwards by the

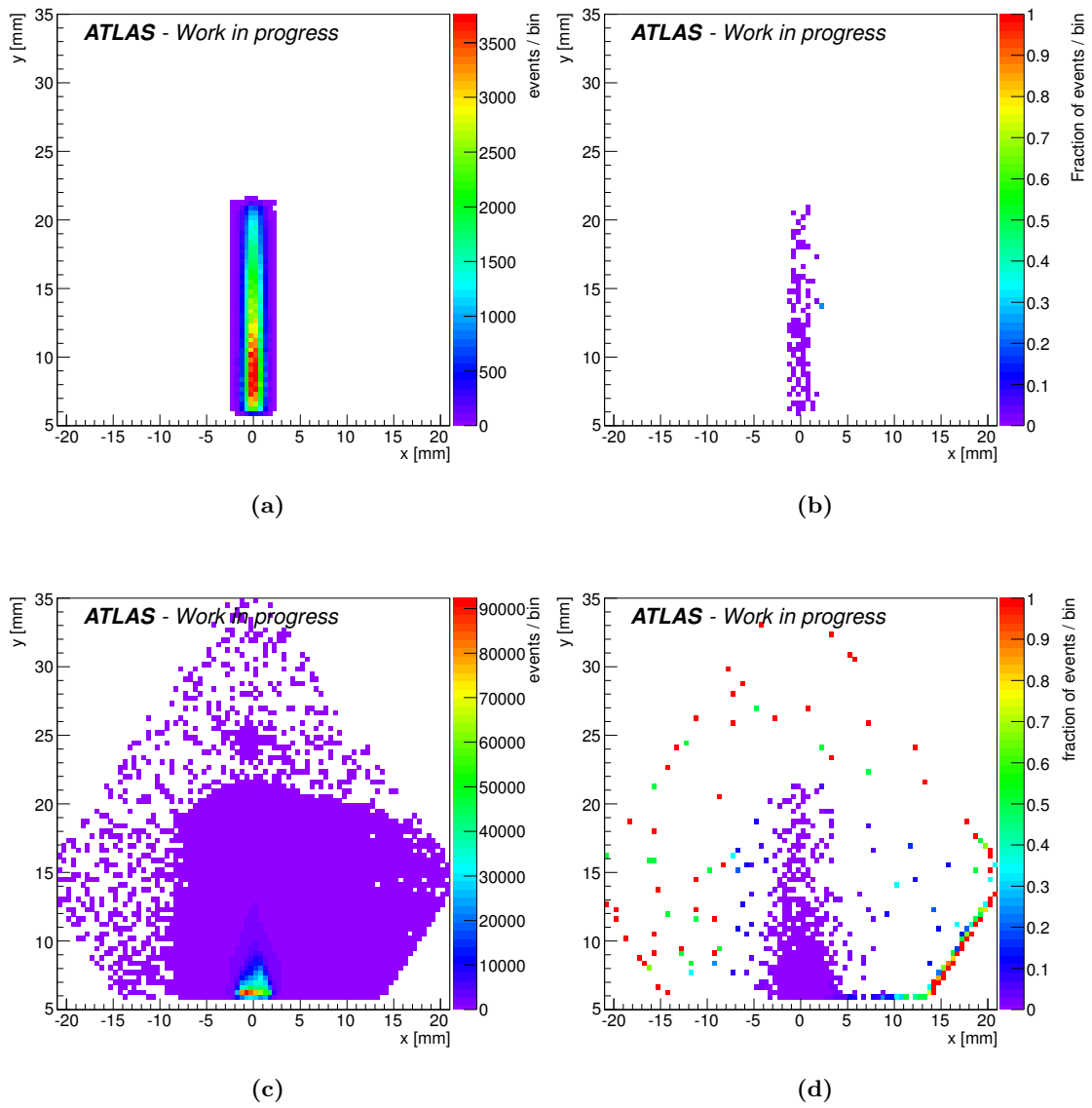

Figure 6.2: Hitmap showing the geometrical distribution of events on the ALFA detector 1, respectively the distribution of all events, and the fraction of events in a given bin with wrong triggering for **(a)**-**(b)** elastics like events and for **(c)**-**(d)** diffractive like events (no MBTS selection).

alignment uncertainty. However, the effect turns out to be negligible, and the systematic uncertainties, due to changing the alignment up or down, are added in quadrature.

6.3 Normalizing the ALFA calibration stream

Even though the ALFA calibration stream is the most inclusive, it can not be taken to include all events within the acceptance of ALFA. For elastic like events, a real event will be missing from the ALFA calibration stream, if the triggers of all 4 detectors fail. Investigating how often 1, 2, and 3 detectors have incorrect triggering, an estimate can be made on how often 4 detectors have incorrect triggering. For diffractive like events, just 2 detectors can have incorrect triggering before the event is missed in the ALFA

calibration stream. No random triggers were available in this stream, and thus could not be employed for an analysis less correlated to the ALFA triggering system. Let f^i_{true} denote the fraction of true events of type i in the ALFA calibration stream, indicating the needed normalization of the ALFA calibration stream.

Elastic like events

Investigating the elastic like events, it is found that after edge and b-to-b cut, one trigger fails to trigger in $(0.047 \pm 0.003$ (stat.) ± 0.027 (cuts)) % of the elastic like events, while two triggers fail in $(0.032 \pm 0.002$ (stat.) ± 0.011 (cuts)) % of the events. For all the events where two triggers fail, the two triggers are on the same side of the IP, and furthermore, (79.2 ± 8.6) % of those cases are for arm 1368. This indicates a correlation between one and two triggers failing on the same side. Moreover, it is found that practically no elastic like events have wrong triggering in 3 out of the 4 detectors, i.e 0(1) instances in 593025(624083) events with (without) edge and b-to-b cut.

From these observations it can not be concluded whether there is a correlation between having wrong triggering in 3 and 4 detectors, though all elastic like events can be assumed to be saved in the ALFA calibration stream, i.e. $1 - f^{\text{elastic}}_{\text{true}} < 10^{-5}$ at a 99.7 % confidence level. The comparison between the two elastic arms can be seen in Figure 6.3(a).

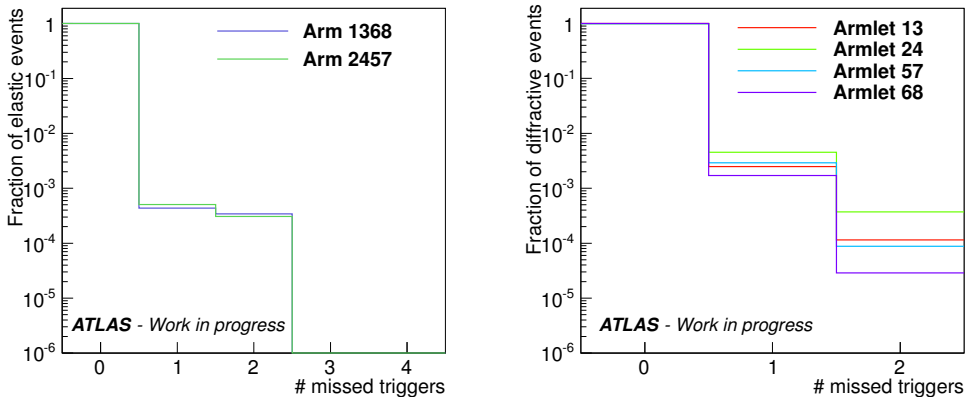

(a) **(b)**

Figure 6.3: Distributions showing the fraction of missed triggers per events **(a)** in elastic like events and **(b)** in diffractive like events.

Diffractive like events

For the diffractive like events, it is found that after the edge cut (0.278 ± 0.003) % of the events have one triggering failing. Combining this with the knowledge of the correlation of two triggers, one could expect that 0.189% of diffractive like events have two triggers failing. So a conservative estimate would be that $f^{\text{diff.}}_{\text{true}} \sim (99.8 \pm 0.1)$ %.

From Figure 6.3(b) a small amount of events with 2 missing triggers are found in diffractive like events (the same pattern is seen for diffractive like events with MBTS selection, see Appendix B.3). These are in the stream due to triggering in other ALFA detectors than the ones considered. The events can however be neglected as they constitute < 0.1 % of the events, which is within the error estimated for $f^{\text{diff.}}_{\text{true}}$.

Furthermore, a systematic effect of the composition of the ALFA detector is seen on Figure 6.3(b). Arms 13 and 68 are performing better than arms 24 and 57 respectively.

This can be explained by the fact that on ALFA detector 1, 3, 6 and 8 the trigger tiles are after the MD, and vice versa in ALFA detectors 2, 4, 5 and 7 (described in Section 5.3). Such that if there is a track in two consecutive detectors, it is more probable to miss the trigger tiles in armlets 24 and 57 than in armlets 13 and 68. Moreover, it hints at a slightly higher efficiency of ALFA detectors 5-8, compared to 1-4. These effects will also be apparent when looking at the trigger efficiencies in the individual ALFA detectors in Section 6.5.

6.4 Normalizing ALFA physics stream

For the analysis using the ALFA physics stream, the normalization to the ALFA calibration stream is needed to refer further back to the real events. This is simply done by calculating the following normalization

$$N_{\text{Phys/Cal}} = \frac{\#\text{ events of interest in ALFA physics stream}}{\#\text{ events of interest in ALFA calibration stream}} \tag{6.1}$$

In Table 6.2 the normalization to the ALFA calibration stream is shown without cuts. For this run the trigger items `L1_ALFA_ELAST15/18` were not prescaled for the physics stream, thus a normalization close to 1 for elastic like events. The trigger items `L1_ALFA_ANY` and `L1_ALFA_SDIFF5/6/7/8` were prescaled with 10 and 20 respectively, thus the normalization is supposed to be around $0.1 - 0.15$, for the diffractive like events. This matches well with the observed normalization.

Table 6.2: The proper normalization between the ALFA calibration stream and the ALFA physics stream after the number of tracks cut.

	Elastic-like events	Diffractive-like events		
		No MBTS sel.	MBTS1	MBTS2
Calibration stream	624083	4188196	462859	349692
Physics stream	623970	465443	50279	37890
$N_{\text{Phys/Cal}}$	0.9998 ± 0.0018	0.1111 ± 0.0002	0.1086 ± 0.0005	0.1084 ± 0.0006

This study led to the discovery of an inconsistency in the data sample. It was observed that in two LBs there were more elastic like events in the ALFA physics stream than in the ALFA calibration stream, which does of course not make sense. The problem turned out to be related to the data handling, as discussed in Ref. [87].

6.5 Trigger efficiency

In the following the trigger performance will be quantified. All the numbers are calculated for the elastic or diffractive like events in the calibration stream, with varying additional cuts.

Let the efficiency of the triggers be defined as

$$\epsilon_{\text{trig}} = \frac{\#\text{ events of interest with perfect triggering in ALFA}}{\#\text{ events of interest}}, \tag{6.2}$$

where *events* refer to either elastic like or diffractive like events in the calibration stream, while *perfect triggering* refers to all four detectors in elastic like events, or both detectors in diffractive like events, triggering correctly.

The efficiency for the individual detectors are shown for elastic and diffractive like events after all cuts in Figure 6.4, with similar behavior of diffractive like with and without

MBTS (see Figure B.7 in the appendix). The effect from the different order of the MD and trigger tiles, discussed in Section 6.3, is clearly seen for diffractive like events (Figure 6.4(b)), but is also visible for elastic like events (Figure 6.4(a)). It is also confirmed that on average the ALFA detectors 5-8 are slightly more effective than 1-4.

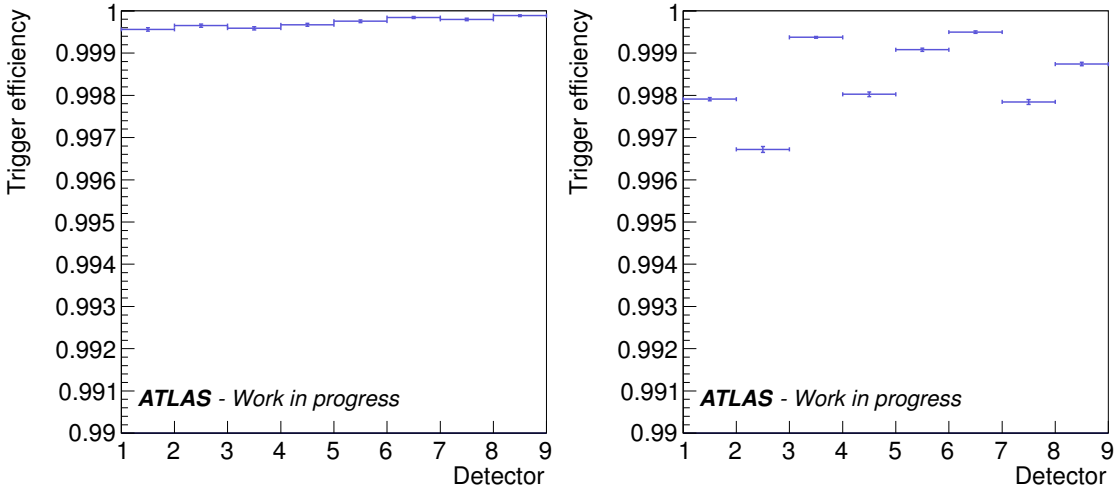

Figure 6.4: Efficiency of the triggering with binomial errors for all ALFA detectors **(a)** in elastic like events and **(b)** in diffractive like events (everything after all applied cuts).

In Table 6.3 the averages of the eight ALFA detectors are presented for the different selections, with and without the additional cuts. A higher efficiency is expected for the more tightly selected events, assuming that there are more particles passing straight through the detectors in that sample.

Table 6.3: The resulting efficiency when relying on trigger bits in ALFA, with the standard deviation on the mean.

	Elastic-like events (%)	Diffractive-like events		
		No MBTS sel. (%)	MBTS1 (%)	MBTS2 (%)
$\langle \epsilon_{\text{trig}}^{\text{no cuts}} \rangle$	99.96±0.01	99.74±0.17	99.70±0.17	99.69±0.18
$\langle \epsilon_{\text{trig}}^{\text{all cuts}} \rangle$	99.97±0.01	99.84±0.09	99.80±0.12	99.78±0.12

CTP signal efficiency

It is also investigated whether there is a degrading of the efficiency of the signal going to the CTP:

$$\epsilon_{\text{CTP}} = \frac{\#\text{ events with CTP bit reflecting the event type}}{\#\text{ events of interest with perfect triggering in ALFA}}, \tag{6.3}$$

where events refer to the either elastic like or diffractive like events in the calibration stream. An event with correct triggering, that has the corresponding trigger item in the CTP true, is an event with correctly reflecting CTP bit. Hereby is not meant a measure of the efficiency of the CTP itself, but rather an estimate of how likely it is that a signal that should go to CTP actually arrives at CTP. In order to make a proper measure of just the CTP signal efficiency, care is taken only to compare the events which are correctly

triggered in ALFA, and hence should be correctly described at CTP. It turns out that the efficiency for the CTP is independent of cuts, and found for the four selections to be:

$$\begin{aligned}
\epsilon_{\text{CTP}}^{\text{Elastic}} &= (99.997 \pm 0.001\ (\text{stat}))\ \% \\
\epsilon_{\text{CTP}}^{\text{SD, no MBTS}} &= (99.986 \pm 0.001\ (\text{stat}))\ \% \\
\epsilon_{\text{CTP}}^{\text{SD, MBTS1}} &= (99.994 \pm 0.001\ (\text{stat}))\ \% \\
\epsilon_{\text{CTP}}^{\text{SD, MBTS2}} &= (99.996 \pm 0.001\ (\text{stat}))\ \%
\end{aligned} \tag{6.4}$$

Efficiency of CTP trigger item

Most analyses use the trigger items in the CTP as selection criteria. Therefore it is relevant to calculate the efficiency of selecting in that way.

$$\epsilon_{\text{trigger item}} = \frac{\#\text{ events of interest fulfilling trigger item}}{\#\text{ events of interest}}, \tag{6.5}$$

where events refer to the either elastic like or diffractive like events in the calibration stream. This is essentially the combination of ϵ_{trig} and ϵ_{CTP}, though now it shall be subdivided into the different arm(let)s. For the study of elastic events the trigger items `L1_ALFA_ELAST15/18` are used, corresponding to triggering in arm 1368/2457. For the analysis on single diffractive events the trigger items `L1_ALFA_SDIFF5/6/7/8` are used, corresponding to triggering in armlet 13/24/57/68.

Single track analysis For the event selection mentioned in Section 6.2, the efficiencies of the trigger menu items in question are found to be:

$$\begin{aligned}
\epsilon_{\text{L1_ELAST15}} &= (99.9633 \pm 0.0034\ (\text{stat}) \pm 0.0001\ (\text{cuts})\ \pm 0.0002\ (\text{alignment}))\ \% \\
\epsilon_{\text{L1_ELAST18}} &= (99.9642 \pm 0.0036\ (\text{stat}) \pm 0.0002\ (\text{cuts})\ \pm 0.0003\ (\text{alignment}))\ \% \\
\epsilon_{\text{L1_SDIFF5}} &= (99.7592 \pm 0.0038\ (\text{stat}) \pm 0.0046\ (\text{cuts})\ \pm 0.0001\ (\text{alignment}))\ \% \\
\epsilon_{\text{L1_SDIFF6}} &= (99.4930 \pm 0.0084\ (\text{stat}) \pm 0.0014\ (\text{cuts})\ \pm 0.0001\ (\text{alignment}))\ \% \\
\epsilon_{\text{L1_SDIFF7}} &= (99.7440 \pm 0.0062\ (\text{stat}) \pm 0.0006\ (\text{cuts}))\ \% \\
\epsilon_{\text{L1_SDIFF8}} &= (99.8485 \pm 0.0044\ (\text{stat}) \pm 0.0009\ (\text{cuts}))\ \%
\end{aligned} \tag{6.6}$$

The systematic uncertainty due to the alignment is only indicated when it was not compatible with 0 at a confidence level of 95%.

Multiple track analysis The efficiency of the CTP trigger items for elastic events is also investigated when allowing for events with more than one track. This adds $\sim 40\%$ more events to the sample. In the events with multiple tracks, at least one of the tracks is required to fulfill all the cuts. The efficiencies for elastic trigger items in this setup are found to be:

$$\begin{aligned}
\epsilon_{\text{L1_ELAST15}}^{\text{multi}} &= (99.9613 \pm 0.0030\ (\text{stat}) \pm 0.0152\ (\text{cuts})\ \pm 0.0002\ (\text{alignment}))\ \% \\
\epsilon_{\text{L1_ELAST18}}^{\text{multi}} &= (99.9599 \pm 0.0031\ (\text{stat}) \pm 0.0265\ (\text{cuts}))\ \%
\end{aligned} \tag{6.7}$$

It shows that the cuts are more important for the multitrack events. Furthermore, a comparison can be done to see the effect of including events with multiple tracks. Though since the samples are correlated, one can not use the errors on (6.7) and (6.6) independently. Instead the sample of only events with ≥ 2 tracks can be used, to get an uncorrelated sample, and simple error propagation can be applied. It is found that

$\epsilon^{\text{tracks}\geq 2} = 99.9553/99.9500 \pm 0.0064/0.0064$ for trigger items `L1_ALFA_ELAST15/18`. From this it can be concluded that the trigger item efficiency is consistent within the errors, thus the result of the multi track analysis is consistent with that determined for single tracks only.

The two calculations are expected to result in the same efficiency, and based on the observed consistency in elastic like events one cannot reject this assumption.

6.6 Investigating tracks in ALFA

If a particle flies through the ALFA detector, and the triggering results in reading out the event, the next big issue is the tracking of the particle. There are a number of effects such as noise, crosstalk, ineffective layers and showers, that makes the matter more complex. Unless otherwise mentioned, the following discussion will be on single diffractive like events.

In order to investigate the efficiency of the ALFA tracking algorithm, it is necessary to look into the activity of the detector.

Noise in detector

To understand the detector response, one can look at the hit multiplicity in the fibers for a detector pair, when there only is a trigger in the detector closest to the IP (inner detector). On Figure 6.5(a) the number of fibers in the ALFA detectors with a signal (the *fiber hit multiplicity*) is shown for events with a trigger in the inner detector.

A clear peak can be seen around ≈ 24 fibers hits, corresponding to a track through the 20 fiber layers (modulo noise and inefficient layers). In the low end there are events that just scraped the detector, and towards the high end there is a decreasing structure, assumed to come from noise in the detector. In comparison, the outer detector, which did not trigger, shows the same shape of scraping particles, but except for that, only an exponentially decreasing distribution is visible, expected from noisy channels. A channel has a signal due to noise with some probability, and from Poisson statistics the probability of more channels sending out noisy signals falls off exponentially with multiplicity. This is exactly the shape observed. Figure 6.5(b) shows the same level of noise in the inner detector, in the opposite case, with a trigger in the outer and no trigger in the inner detector. A crude fit to the distribution towards high multiplicity gives a slope of order 10^{-2}.

One can note the effect of the trigger inefficiency, responsible for the bump in the distribution of the outer detector around a fiber hit multiplicity of ~ 20 on Figure 6.5(a).

The same conclusions can be drawn for the other armlets (distributions presented in Appendix B.5).

Tracking

In order to understand the performance of the tracking algorithm, an investigation of the fiber hit multiplicities in detector 1 is presented on Figure 6.6(a) against the number of tracks that were reconstructed in that detector. As anticipated the main contributors are events with 1-2 tracks. The events with no reconstructed tracks are dominated by events with low or high fiber hit multiplicities. There are also some events with no reconstructed tracks, even though the fiber hit multiplicities are 10-60, which usually yields a reconstructed track.

In order to investigate the events with no reconstructed tracks, the requirement for actually reconstructing a track must be understood. On Figure 6.6(b), the layers of fibers

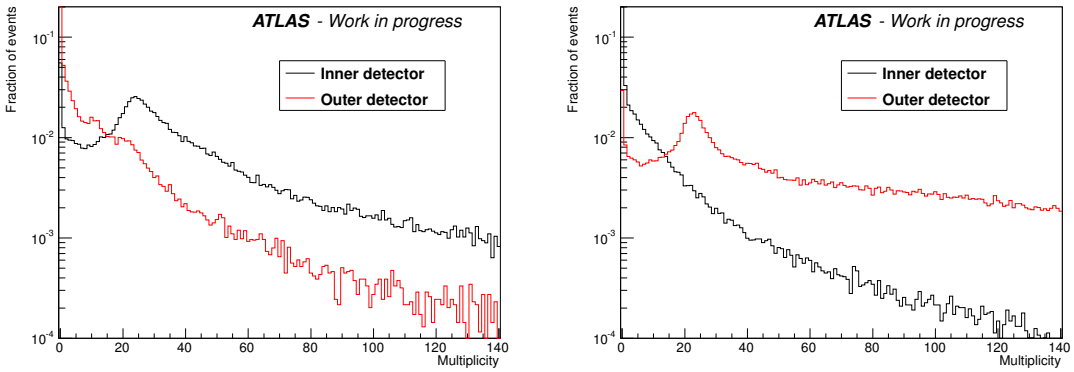

(a) **(b)**

Figure 6.5: Fiber hit multiplicities presented for the inner and outer detector of armlet 13 for events with **(a)** trigger in inner, and no trigger in outer detector and **(b)** vice versa.

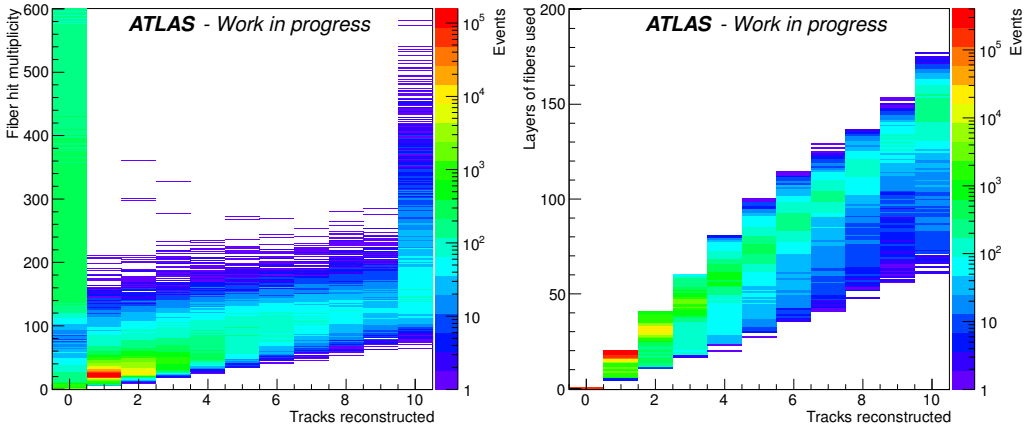

(a) **(b)**

Figure 6.6: The number of tracks reconstructed in events with triggering in both detectors plotted against **(a)** fiber hit multiplicity **(b)** layers used in the reconstruction.

used in the reconstruction is plotted versus the number of tracks reconstructed. It is seen, that most often, more than 15 layers are used when only 1 track is reconstructed. This can be used as a constraint, to look at the reason for not reconstructing an event in a detector, when there is a well reconstructed track in the companion detector.

Two different issues

Let a good track be one where $\geq$ 15 layers have been used in the reconstruction. In Figure 6.7, the spectrum of the fiber hit multiplicity in the outer detector is presented, when there was a well reconstructed track in the inner detector, and vice versa.

Both the inner and the outer detector have a large number of events in the low end. These originate from tracks outside the fiducial region of the detector, i.e. just scraping the detector, and noise (the exponential slope is of order 10^{-2}, like the one found from noise on Figure 6.5(a)).

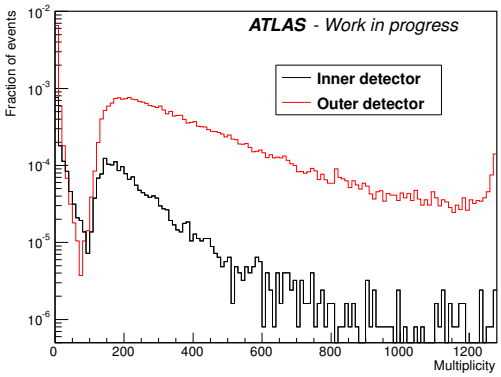

Figure 6.7: Fiber hit multiplicity distribution in the outer detector, for events with one well reconstructed track in the inner, and no reconstructed track in the outer, as a fraction of all the events with a well reconstructed track in the inner detector, and vice versa.

In the high end at a fiber hit multiplicity of $\sim$ 200 and higher are the other events, which are likely to originate from showers saturating the detector. These effects are also seen in the other armlets (see Appendix B.6), and it shall be investigated in the following.

Showering effects

The spectrum of the inner and outer detector differs with an order of magnitude in the high hit multiplicity end. This shows that the high hit multiplicity events can not be caused by a random effect. The difference indicates a physics effect and one obvious idea is showering: One must expect that a particle going through the inner detector can interact with the material passing through the detector, most probably resulting in a shower of particles in the outer detector, saturating the tracking algorithm.

On the other hand, if the track of a proton is well reconstructed in the outer detector, it must also have been passing nicely through the inner detector. Thus only some interaction effect, which does not destroy the proton, can cause the high multiplicity events observed in the inner detector.

A typical event with a good reconstructed track in the inner detector and none in the outer detector, but a high multiplicity, is shown in Figure 6.8. The ALFA detector 6 and 8 is shown, corresponding to the proton flying from the left to the right, and the expected showering is clearly visible.

The fraction of events with a well reconstructed track in one detector that has no reconstructed track in the companion detector is presented in Table 6.4 for all four armlets. As the ALFA detectors in armlet 24 and 57 have the trigger before the MD, these are expected to have a slightly higher rate of showers, because of the higher amount of material before the tracking.

However, this can not be confirmed in data. The largest fraction of events with a shower in the outer detector is found in armlet 68. Furthermore, the fraction of events with no reconstructed tracks in the inner detector (when expected) is twice as high in armlet 13 than in the other armlets. This has to be investigated before the final diffractive analysis can be completed.

Comparing to the independent study on elastic like events [88], the origin for the problem could not be found. However, the expected difference due to the order of the trigger and the MD is actually observed in the analysis of elastic like events, which can also be inferred from combining armlet 13 with 68 and armlet 24 with 57 in Table 6.4.

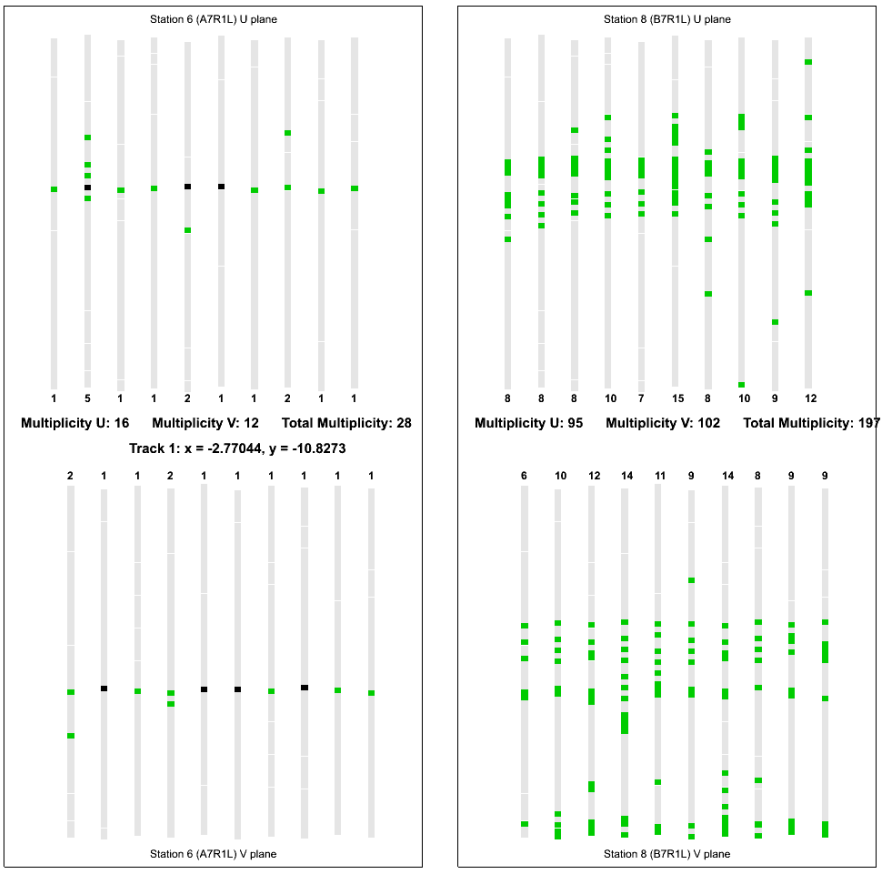

Figure 6.8: Event display for event with the proton flying from left to right, leaving a good track in one detector, and no track reconstructed in the outer detector because of the showering, visible from the high fiber hit multiplicity.

Table 6.4: Fraction of events that have no reconstructed track when there is a good track in the companion detector (the error is of the order 1%).

	Armlet 13	Armlet 24	Armlet 57	Armlet 68
f(0 in outer|good in inner)	0.0203	0.0283	0.0278	0.0312
f(0 in inner|good in outer)	0.0053	0.0026	0.0020	0.0022

Interaction probabilities

Assuming that the events with a well reconstructed track in the inner detector, and no tracks reconstructed in the outer detector (but a high multiplicity), are due to showers caused by material interaction, it is worth investigating the interaction probability when going through an ALFA detector.

In Table 6.5 the interaction lengths for materials in the ALFA detector are presented along with the probability of having an interaction. The interaction probability is given as $P = L/\lambda_I$, with L being the material thickness, and $\lambda_I = 1/(\sigma_{\text{inel}} n_a)$ the interaction length, where n_a is the atoms per unit volume, and σ_{inel} is the inelastic cross section. The values for λ_I are listed in Ref. [36] for a proton with an energy of 200 GeV. Scaling λ_I to 3500 GeV corresponds to scaling σ_{inel} from 200 to 3500 GeV. The scaling is done using the expectations for the total and elastic cross section presented in Ref. [10]. This carries

some uncertainty, which is reflected by the uncertainty on the interaction length listed in Table 6.5. The result is a probability of $(3.67 \pm 0.18)\%$ for interacting with the material when traversing one ALFA station.

Comparing with Table 6.4, the numbers found in data are 20-70% lower than expected from the material budget. A similar trend was seen in a study of MC simulated events, where it was found that 30% fewer events were not reconstructed in MC compared to the material budget [89]. The theoretically calculated loss from material might be bigger than the fraction determined in data, as an interaction does not imply that the track cannot be reconstructed. Due to time constraints further investigations in this matter were not done, as it would necessitate an entirely separate study of the simulation.

Table 6.5: Individual material contributions to the interaction probability with the matter in the detector by a traversing particle with energy 3.5 GeV (calculated from material information from Ref. [90, 91], and energy scaling estimate using Ref. [10])

Material	Fe	Scintillator	G10
Thickness / mm	$2 \cdot 0.5$	$2 \cdot 3 + 2 \cdot 10 \cdot 0.5$	$2 \cdot 10 \cdot 0.17$
Interaction length / mm	0.15 ± 0.01	0.70 ± 0.03	0.48 ± 0.02
Resulting interaction probability / %	0.67 ± 0.04	2.29 ± 0.11	0.71 ± 0.03

Medium multiplicity losses

The events presented on Figure 6.7 with fiber hit multiplicity within the region 10-60, are as mentioned a bit odd. If they stem from showering, then the low number of fiber hits should allow for successful reconstruction. If they stem from a slightly higher scraping, one would no longer characterize it as scraping as they should be reconstructed.

It turns out to be caused by a strange coincidence, with no possibility to reconstruct the track, even though a particle is nicely passing through the companion detector. One typical example in this group is shown in Figure 6.9. Even though there is a well reconstructed track in the outer detector, the signal in the inner detector is not resembling a particle passing through the detector. This type of events can be explained by a particle going through the region where the fibers are led towards the MAPMTs, outside the acceptance of the main detector. This explains the complete lack of signal in one projection.

Another example can be seen in Figure 6.10, again there is a well reconstructed track in one detector, but in the outer detector it seems like there are lots of failing layers combined with a shower. One possible explanation is some kind of showering in the inner detector, which does not reach the outer detector. An example of this is a *delta-ray*. Electrons escape a nucleus due to ionization by the passing proton, which produces a shower of secondary electrons. This would make it possible for the energy of the shower to diffuse before hitting the outer station.

6.7 Tracking efficiency

No matter the reason for not being able to reconstruct the track, it is problematic if the analysis relies on track information. The result is a loss of events that needs to be

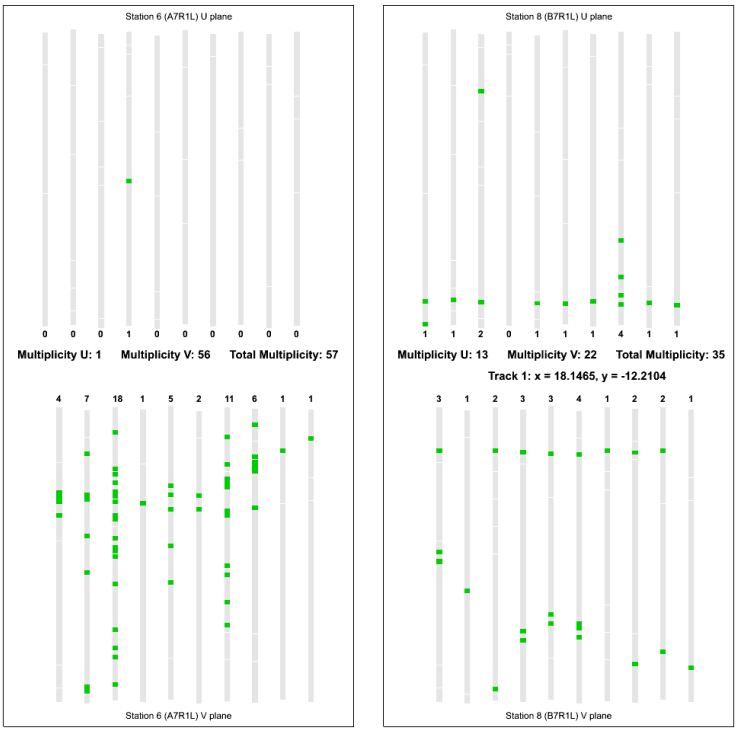

Figure 6.9: Event display for event with a good track in one detector, and no track reconstructed in the companion detector. This can be explained by a proton passing through the region of the detector where the fibers from the MD are led towards the MAPMTs (see text)

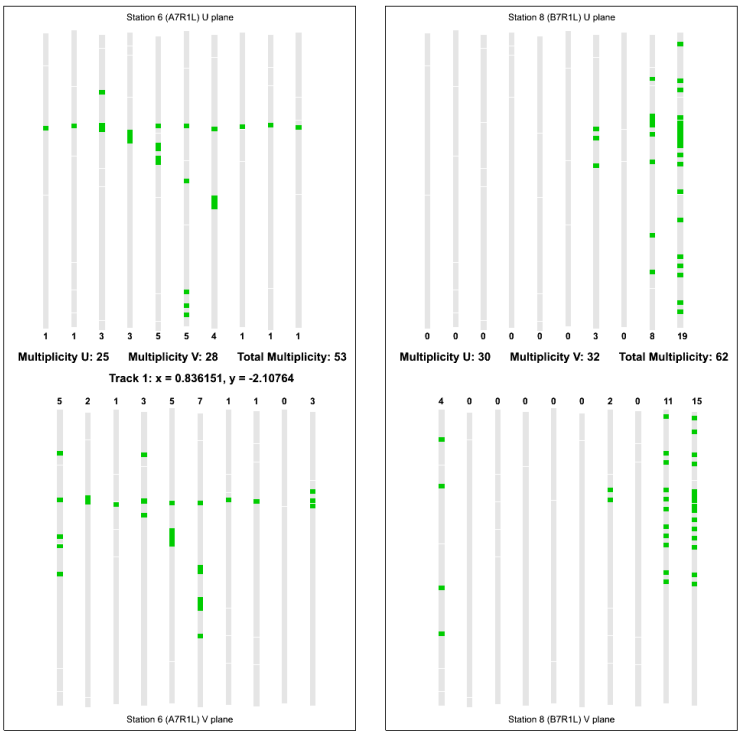

Figure 6.10: Event display for event with a good track in one detector, and no track reconstructed in the companion detector. This can be caused by delta rays not hitting the outer detector (see text for discussion).

corrected for by the tracking efficiency, defined as

$$\epsilon_{\text{trk}} = \frac{\#\text{ events of interest with at least 1 reconstructed track in relevant detectors}}{\#\text{ events of interest}}, \tag{6.8}$$

where the events of interest in this part will be elastic or single diffractive like events in the calibration stream.

Elastic tracking efficiency

Since the cuts on elastic like events, introduced in Section 6.2, are heavily dependent on the reconstructed tracks, the tracking efficiency for elastic like events was studied carefully for events with a combination of having four detectors triggering and zero to four detectors with reconstructed tracks. This analysis was presented in Ref. [88] and it was found that

$$\epsilon^{\text{El.,1368}}_{\text{tracking}} = (90.5347 \pm 0.0433\ (\text{stat.}) \pm 0.3337\ (\text{syst.}))\ \% \tag{6.9}$$

$$\epsilon^{\text{El.,2457}}_{\text{tracking}} = (88.9356 \pm 0.0476\ (\text{stat.}) \pm 0.3798\ (\text{syst.}))\ \% \tag{6.10}$$

Again the different order of the MD and the trigger tiles in the ALFA detectors results in slightly different tracking efficiencies for the two elastic arms. Moreover, it was found that the tracking efficiency is independent of the squared transferred momenta t.

Diffractive tracking efficiency

For the single diffractive like events no previous study was made, thus the efficiency of tracking single diffractive events has been determined by the author. The diffractive tracking efficiency shall be assumed to be constant over t as well.

Compared to the tracking efficiency of elastic events there are fewer ways of constraining the diffractive events. This makes it more difficult to cover only the diffractive events. Thus this study has initially been focused on the selection used in the analysis of diffractive events presented in Chapter 9. Events with triggers and tracks in the detectors of one armlet are selected. In order to get a cleaner sample of single diffraction, the MBTS is required to have triggered, indicating some activity in ATLAS, removing some of the elastic events with one proton outside the acceptance. This results in the following tracking efficiency for the 4 armlets:

$$\begin{aligned}
\epsilon^{\text{SD.,13}}_{\text{tracking}} &= (87.8059 \pm 0.0631\ (\text{stat.}))\ \% \\
\epsilon^{\text{SD.,24}}_{\text{tracking}} &= (86.1066 \pm 0.0808\ (\text{stat.}))\ \% \\
\epsilon^{\text{SD.,57}}_{\text{tracking}} &= (86.0183 \pm 0.0816\ (\text{stat.}))\ \% \\
\epsilon^{\text{SD.,68}}_{\text{tracking}} &= (85.4282 \pm 0.0803\ (\text{stat.}))\ \%
\end{aligned} \tag{6.11}$$

Which agrees with the observed fraction of events lost to showering (presented in Table 6.4).

Furthermore, a veto on the other arms will be used, as it gives a more restricted sample, and might exclude more beam background events. For the more restricted sample the tracking efficiency is significantly higher:

$$\begin{aligned}
\epsilon^{\text{SD.,13}}_{\text{tracking}} &= (98.1466 \pm 0.0307\ (\text{stat.}))\ \% \\
\epsilon^{\text{SD.,24}}_{\text{tracking}} &= (98.0555 \pm 0.0403\ (\text{stat.}))\ \% \\
\epsilon^{\text{SD.,57}}_{\text{tracking}} &= (98.0235 \pm 0.0409\ (\text{stat.}))\ \% \\
\epsilon^{\text{SD.,68}}_{\text{tracking}} &= (97.5262 \pm 0.0439\ (\text{stat.}))\ \%
\end{aligned} \tag{6.12}$$

In order to understand the tracking efficiency for single diffractive event, one must use MC in order to get a more controlled sample. This would also allow for the distinction of when a track is reconstructed despite a shower, and when it is not. Furthermore, it would give a better handle on the systematic uncertainties which were not looked into. The author did not have access to a MC sample usable for this study, thus it must be postponed until such a MC sample is available.

6.8 Combined efficiency

In this chapter the efficiency of the ALFA detector has been determined, signifying the first part of the understanding needed in order to estimate the cross section of single diffractive events.

The efficiencies discussed can for each armlet be combined into a weight, such that one can relate the number of events passing certain cuts that are measured, N_{measured}, to the true number of events, N_{true}, one would measure if the detector were perfect.

$$N_{\text{true}} \approx w_{\text{ALFA}} \cdot N_{\text{measured}}, \tag{6.13}$$

Thus w_{ALFA} is the estimate of the combined loss due to inefficiencies in ALFA. The weight has, in this chapter, been estimated for the most obvious effects of trigger and tracking efficiency, such that

$$w_{\text{ALFA}} = \frac{1}{\epsilon_{\text{trk}}} \cdot \frac{1}{\epsilon_{\text{trigger}}} \cdot \frac{1}{f^{\text{true}}} \tag{6.14}$$

For the selection used in Chapter 9, the weight can, based on the results in this chapter, be estimated to

$$\begin{aligned} w_{\text{ALFA}}(\text{armlet } 13) &= 1.023 \pm 0.001, \\ w_{\text{ALFA}}(\text{armlet } 24) &= 1.027 \pm 0.001, \\ w_{\text{ALFA}}(\text{armlet } 57) &= 1.025 \pm 0.001, \\ w_{\text{ALFA}}(\text{armlet } 68) &= 1.029 \pm 0.001. \end{aligned} \tag{6.15}$$

7

The Minimum Bias Analysis

The Minimum Bias Analysis presents the inclusive distributions of charged particles in ATLAS. These have been measured in pp and $p\bar{p}$ collisions at a range of energies, and are used in constraining models of soft processes and to predict properties at higher center of mass energies [92]. The author has contributed to the analysis at 8 TeV, using the data collected in run 200805 with an integrated luminosity of $\approx 160\mu b^{-1}$. Moreover, the comparison to MC is done using the Pythia 6, Pythia 8 and Epos MC event generators. A full list of the used datasets can be found in Appendix C.

7.1 Motivation and strategy

As has been seen in earlier studies [70, 92] and will be apparent from the results discussed here, soft processes dominate the proton-proton collisions at LHC. The scope of the Minimum Bias Analysis is to study the general properties of these processes. Different models have been developed to understand the soft processes better, and the minimum bias distributions are a way to constrain these models. This has a huge impact on the measurements of hard processes, due to the better understanding of underlying events and pile-up for the high p_T events [92].

The properties of the soft inelastic proton-proton collisions that provide the easiest comparison with MC are the kinematic observables of charged particles, i.e the distributions

$$\frac{1}{N_{\text{ev}}}\frac{dN_{\text{ch}}}{d\eta}, \quad \frac{1}{N_{\text{ev}}}\frac{dN_{\text{ev}}}{dn_{\text{ch}}}, \quad \frac{1}{N_{\text{ev}}}\frac{dN_{\text{ch}}}{dp_T}, \tag{7.1}$$

where N_{ev} and N_{ch} are the number of events and number of charged tracks in the sample, n_{ch} is the number of charged tracks in one event, and η and p_T are the pseudorapidity and transverse momentum of each track. Also the $\langle p_T \rangle$ vs. N_{ch} distribution is studied, though the work on this was not part of the author's contribution. The study is done for charged primary particles, defined as charged particles with a mean lifetime $\tau > 0.3 \cdot 10^{-10}$ s produced either directly in the pp collision or from decays of particles with shorter lifetime. Particles produced subsequently shall be denoted secondary particles (or simply *secondaries*).

These distributions have been measured in the past, and each measurement helps to restrict the model of soft processes. The distributions are measured on minimum bias samples to obtain the most inclusive representation. The corrections of detector effects are then done on data, to obtain results with the lowest possible model dependence.

Relevance for diffractive study

As mentioned in the preface, diffractive processes contribute with a non-negligible fraction of events. These processes are (as discussed in Section 2.7) difficult to model, and they

are constrained very little by previous data [92]. A diffractive enhanced sample would make it possible to significantly improve the modeling of diffraction.

An understanding of the track distribution in the inclusive samples is needed for concluding on the track distribution for diffraction. Most corrections used on the inclusive sample are also relevant for the diffractive sample, as the same detector effects influence the track multiplicity distribution considered in the analysis on diffraction.

7.2 Event selection

Only events with the MBTS triggered on either side of the interaction point and fully functioning inner detector are used in the analysis. Only the LBs 215-395 of run 200805 are used, as in this part of the run $\langle\mu\rangle < 0.004$, i.e. less than 0.001% probability to have more than one interaction per bunch crossing. In the analysis, various kinematic regions of the phase space are considered, with varying amount of diffraction, though the author only participated in preparing the kinematic region of:

- $n_{\text{ch}} \geq 2$,
- $p_T \geq 100$ MeV,
- $|\eta| \leq 2.5$.

This is the most inclusive charged-particle spectrum, which allows for study of theoretical models in the extrapolation down to $p_T = 0$.

In order to reduce contributions from background events and secondarily produced particles, events are only used if there is a primary vertex with at least two tracks with $p_T > 100$ MeV, and transverse and longitudinal distance of closest approach with respect to the primary vertex $|d_0^{\text{PV}}| < 1.5$ mm and $|z_0^{\text{PV}}| \sin\theta < 1.5$ mm respectively. Events with a secondary vertex with ≥ 4 tracks are rejected as pile-up events with more than one interaction per bunch crossing. The remaining cases of events with secondary vertices with < 4 tracks were found mainly to be due to *split vertices*, where the vertexing algorithm wrongly reconstructs one vertex as two [93].

Furthermore, the following cuts are applied to tighten the quality of the tracks:

- require tracks to have a hit in the B-layer if they pass a module expected to be active,
- ≥ 1 hit in the pixel detector,
- $\geq 2/4/6$ hits in the SCT for tracks in the interval $100 < p_T \leq 200$, $200 < p_T \leq 300$ and $p_T > 300$ MeV,
- χ^2 probability > 0.01 on the reconstruction of tracks with $p_T > 10$ GeV.

Track reconstruction algorithms

Normally two tracking algorithms are used in the given order, *InsideOut* and *LowPt*, where the subsequent algorithm is only using the hits not tracked by the previous method. The LowPt algorithm has simpler hit requirements and looser cuts on d_0 [94]. It reconstructs about 60 % of the tracks with $100 < p_T < 150$ MeV, and less than 2% for tracks with $p_T > 200$ MeV [92].

7.3 Corrections and unfolding

In each event the number of charged tracks passing the selection is denoted n_{sel}. However, these need to be corrected in order to know the real number of charged particles n_{ch} in that event.

Corrections are applied to each track as well as on an event per event basis to correct for detector efficiencies. The corrections are a major point of the analysis, and will be discussed separately in the following chapter.

Using MC truth distributions *closure-tests* are carried out, testing whether the used corrections actually compensate for the detector inefficiencies. The *non-closure* is a measure for how well the corrections work, with a non-closure of 0 being perfect. For the initial sample (see discussion in following section) a non-closure of less than 1 % was achieved, which is the level of accuracy that is sought for.

When the corrections have been applied, the data sample must be *unfolded*, i.e. make the data independent of detector effects. Thus relating the multiplicity of tracks selected, n_{sel}, to real number of charged particles in that event, n_{ch}. This is done using Bayesian unfolding [95], which is a way of limiting the model dependence of the unfolding procedure as much as possible. An unfolding matrix (relating the probability that a given n_{sel} is due to a certain n_{ch}), is filled initially from MC, and applied to data. The resulting distribution is used to repopulate the unfolding matrix, and the procedure is repeated until the input and unfolding distributions agree within statistical fluctuations (indicated by $\chi^2/n_{\text{dof}} < 1$).

7.4 Unforeseen challenges

Going through the analysis, it became clear that a number of errors had to be corrected, which led to the need for a reprocessing of the datasets. This meant that the anticipated collaborative paper on the Minimum Bias Analysis was not ready for publication by the deadline of this thesis. The results presented in this and the following chapter are for the first processing, but only within $|\eta| < 2.2$, in order to avoid the most problematic areas of the phase space.

Configuration differences

As will be discussed in Chapter 8, it was noticed that the tracking and vertex efficiencies were significantly lower for the new 8 TeV MC samples than they had been for the 7 TeV MC samples. This led to the discovery that the configuration for the tracking algorithms and the selection of vertices were more exclusive in the initial 8 TeV reconstruction settings than in the earlier 7 TeV studies. In short this meant that a reprocessing of the data and MC samples to re-run the tracking and vertexing algorithms became necessary, in order to be able to better compare the 8 TeV data to the 7 TeV data.

Material discussion

In the 8 TeV MC sample, a degradation of the tracking efficiency (to be discussed in Section 8.3) was observed over the full η range with respect to the 7 TeV sample. This discrepancy could be partially attributed to differences in the configuration for the tracking algorithms. However, a particularly large inconsistency was observed between data and MC for $|\eta| > 2.2$, visible on the uncorrected track distribution on Figure 7.1.

In order to find the causes for these discrepancies, further work was done on the *SCT extension efficiency*, which is the efficiency of matching a pixel tracklet (a track

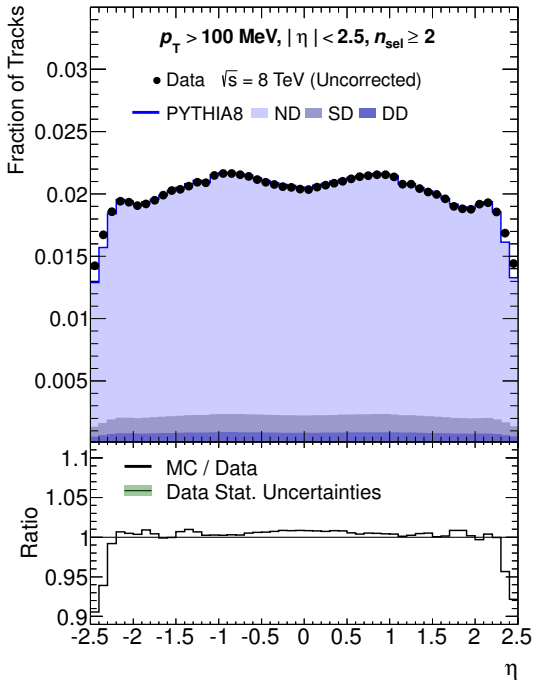

Figure 7.1: The uncorrected track distribution in η, for the minimum bias data, compared to Pythia 8 (subdivided into non-diffraction (ND), single (SD) and double diffraction (DD)), visible is the inconsistency at high η.

candidate consisting only of pixel hits) to a full reconstructed track. This method is particularly sensitive to the material between the Pixel detector and the SCT, which affects the probability that a track passing through this region interacts with the material such that it cannot be reconstructed later. The SCT extension efficiency is compared between data and MC, to see whether the material in that region has been modeled correctly [96]. Discrepancies over 6% were indeed found for $|\eta| > 2.3$ between MC and data in the 8 TeV samples.

It turned out that the GEO model, the detector description used in the simulation, was to blame. The PP0 region of the Inner Detector, which contains a relatively large amount of passive material due to e.g. support structures and cables, was not modeled well enough. The effect of this mismatch was that fewer tracks were lost going through the real detector, than expected from the simulated detector (as seen on Figure 7.1). Because of the Long Shutdown 1 (LS1) phase in the years 2013-2014, when the ATLAS detector is partially dismantled, repaired and upgraded, there was an opportunity to go into every detail of the material structure and composition. The detailed investigation by a collaboration of engineers and the Inner Detector Material Working Group revealed that Pixel support tubes and other materials were not included in the current GEO model (ATLAS-GEO-20-00-01) and some material for small objects was miscalculated. An updated GEO model with a more accurate description (ATLAS-GEO-21-01-00) was subsequently provided and validated [61]. It will be used for the reprocessing of the samples and the conclusion of the Minimum Bias analysis.

Incorrect condition tags

Shortly before deadline for this thesis, test samples with the updated GEO model were produced, and the mismatch in the high η region had indeed diminished. Though a new

issue turned up. The number of inactive pixel modules in MC, which do not contribute hits for the simulated particle tracks, was higher than observed in data. Whether this was caused by a wrongly used detector conditions tag in MC, or a different setup of the threshold on the signal in the modules, could not be resolved by the deadline of the thesis.

However, for the full simulation, digitization and reconstruction a correct GEO model and conditions tag is needed, which means that the entire MC reprocessing needs to be run again. By the deadline for this thesis, the data was successfully reprocessed, but the MC was not ready as no conclusion had been reached in the discussion.

7.5 Systematic uncertainties

For all the corrections, a systematic uncertainty is determined. In this thesis, only the details of the systematic uncertainty on the secondarily produced particles shall be discussed (see Section 8.6).

The uncertainties on the corrections are used to randomize the input distribution (add/remove events) for the unfolding procedure. The difference of the resulting distributions to the nominal distributions is used as systematic uncertainty on the unfolded nominal distributions.

The preliminary distribution of the systematic errors in η can be seen in Figure 7.2 stemming from uncertainties on the material, the fraction of secondaries, as well as some flat systematic uncertainty ascribed to the track reconstruction. Even though these might change for the reprocessed distributions, it will not change the fact that the uncertainty on the material is the largest contribution to the systematic uncertainty. Thus the systematic uncertainty on the secondaries can be set to conservative values, as the effect of optimizing would be minimal (see details in Section 8.6).

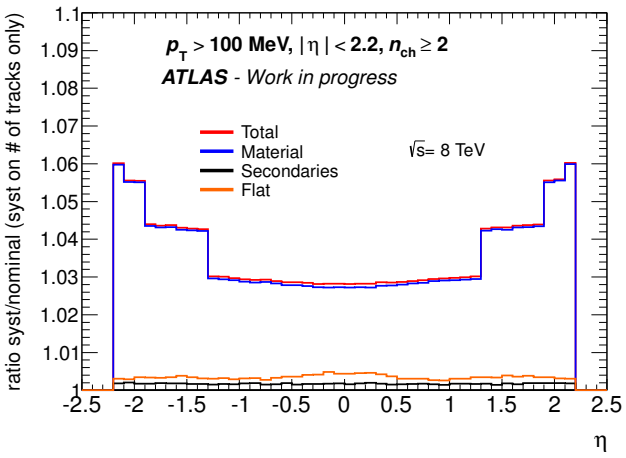

Figure 7.2: The systematic uncertainties on the final charged track multiplicity distributions in η, see details in text.

7.6 Preliminary results

As mentioned, the data and MC samples with the final configuration were not ready by the deadline of this thesis. The previously obtained samples have thus been analyzed within $|\eta| < 2.2$, in order to exclude the most problematic region. The corrections are

naturally affected by this exclusion, and as such the following results must be considered with caution.

Charged-particle multiplicity

In Figure 7.3 the charged-particle multiplicity in η for the present analysis at $\sqrt{s} = 8$ TeV is presented. Compared to the distribution obtained in $\sqrt{s} = 7$ TeV [92] presented in Figure 7.4, the biggest change comes from the slightly larger average number of tracks per event. It is seen that Pythia 8, still seem to be the MC generator capable of describing the minimum bias distributions most correctly, though information in high η is needed to assess the discrepancy to the Epos MC introduced in the study at 8 TeV. However, Pythia 8 will be used as the most promising generator, in determining the detector efficiency in the following chapter.

One can notice that distribution in 8 TeV shows a less uniform dependence on η than in 7 TeV. Moreover, the distribution of Pythia 6, does not seem to have changed. It looks most like it by mistake has been run at 7 TeV, though that issue had not been resolved by the deadline of this thesis.

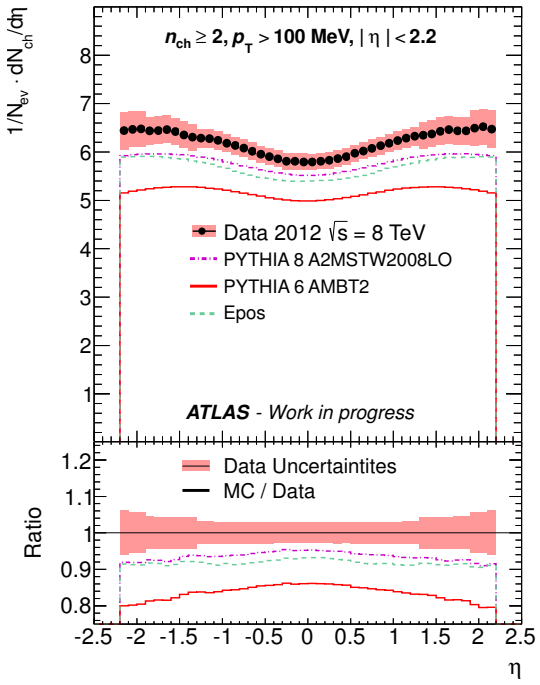

Figure 7.3: Preliminary charged-particle multiplicity in $|\eta| < 2.2$ for data taken at $\sqrt{s} = 8$ TeV. Data is shown with statistical errors.

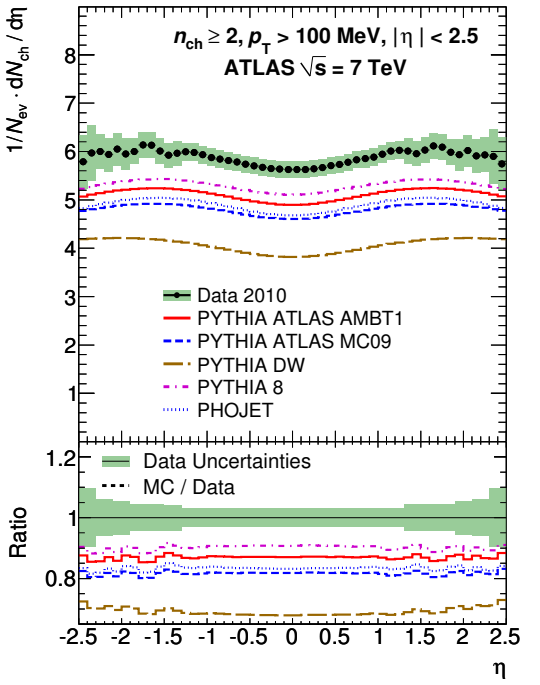

Figure 7.4: Charged-particle multiplicity in $|\eta| < 2.5$ for data taken at $\sqrt{s} = 7$ TeV [92]. Data is shown with statistical errors.

Track density at $\eta = 0$

One of the important results of the Minimum Bias Analysis is the measure of $dn_{\mathrm{ch}}/d\eta|_{\eta=0}$. As previously mentioned, the processes are expected to be evenly distributed in rapidity. Comparing just the center value, asymmetries will not affect the result to the same degree. Also in the center of the detector the material uncertainties are smallest. The center track density is thus a simple number, which is good for comparison.

In the Minimum Bias Analysis, the mean number of charged-particle tracks in the center is computed by averaging $|\eta| < 0.2$, and is at 8 TeV found to be

$$\frac{1}{N_{\text{ev}}} \frac{dN_{\text{ch}}}{d\eta}\bigg|_{\eta=0} = 5.800 \pm 0.003 \text{ (stat.)} \pm 0.165 \text{ (syst.)} \tag{7.2}$$

In Figure 7.5 it is seen how this number fits with previous measurements. Measurements in other phase spaces or other MCs has been grayed out not to obscure the picture. It is seen how the trend of a systematically higher value in data than predicted from MC, continuous, leaving room for improvement of the MCs.

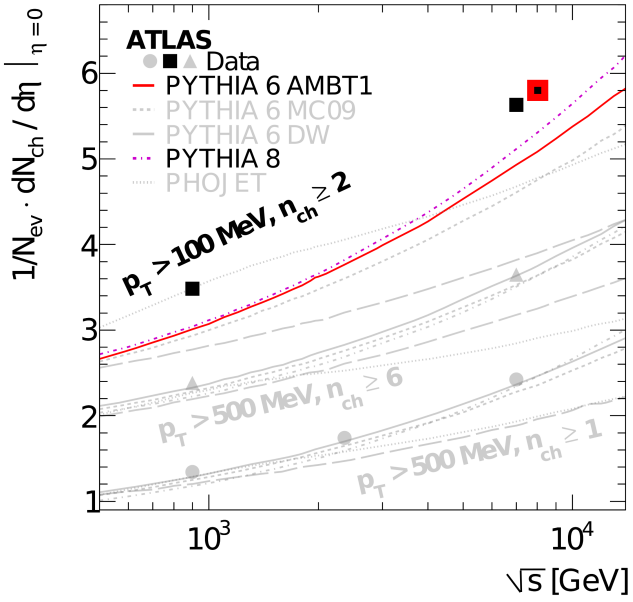

Figure 7.5: Comparing preliminary 8 TeV measurement (with red box) to previous measurements of the track density at $\eta = 0$. Edited from Ref. [92] in order to highlight the studies and MC relevant for this study.

8

Corrections to the MinBias Analysis

In order to present general observations, the data must be corrected for detector effects, model dependencies, and contributions from background and secondary particles. The corrections discussed in this chapter are incorporated into a software package developed and tested by the author. Thereby the most up-to-date corrections can be applied in other analyses as well. The package was carefully compared to the previous methods of including the corrections, and it was made sure that they are 100% compatible. It has now been implemented as the new standard for including the corrections in the Minimum Bias Analysis.

Every event is weighted due to the efficiency of the MBTS trigger ϵ_{trig} and the vertexing algorithm ϵ_{vertex}. Furthermore, MC is reweighed to data due to different distribution of the vertex position $w_{\text{reweigh MC}}$. Thus

$$w_{\text{event}}(n_{\text{sel}}) = \frac{1}{\epsilon_{\text{trig}}(n_{\text{sel}})} \cdot \frac{1}{\epsilon_{\text{vertex}}(n_{\text{sel}}, p_T^{\text{min}}, \Delta z_0^{\text{min}})} \cdot w_{\text{reweigh MC}}, \tag{8.1}$$

where n_{sel} is the number of selected tracks within an event, p_T^{min} is the minimal p_T of a selected track in the event, and Δz_0^{min} is the minimal difference of the transverse impact parameter of two tracks in the event.

Each selected track is corrected for the efficiency of the tracking algorithm ϵ_{trk}, and the additional tracks counted due to tracks migrating from outside the kinematic region considered, f_{okr}, as well as from secondaries, f_{sec}. Thus:

$$w_{\text{trk}}(p_T, \eta) = \frac{1}{\epsilon_{\text{trk}(p_T,\eta)}} \cdot (1 - f_{\text{okr}}(p_T, \eta)) \cdot (1 - f_{\text{sec}}(p_T)), \tag{8.2}$$

Each of the contributions to the weights shall be described in the following sections.

Corrections package

The software package is called `InDetTrackCorr`, and is initialized for a given $\sqrt{s}$, as it covers the corrections needed at collision energies of 0.9, 2.76, 7 and 8 TeV. Then for a given set of n_{sel}, p_T^{min} and Δz_0^{min} the event weight is calculated from histograms, according to the descriptions in the following sections. The weight for each track is calculated from information on the η and p_T of that track. The calculations include the different treatment of data and MC, as well as the systematic uncertainties estimated in the full Minimum Bias Analysis (though no details of these shall be given here).

8.1 Vertex z-position reweighing

In MC the interactions are smeared around the beam spot using a Gaussian distribution. This is seen from Figure 8.1(a), where Gaussian fits have been made to the distributions signifying the shapes. As can be seen, the z-position of the vertex in data is more narrowly distributed. This bias in the MC is corrected for by reweighing events, such that the distribution of the vertex z-position in MC corresponds to data. On Figure 8.1(b), the reweighing has been applied, which establish a clearly visible correspondence from MC to data.

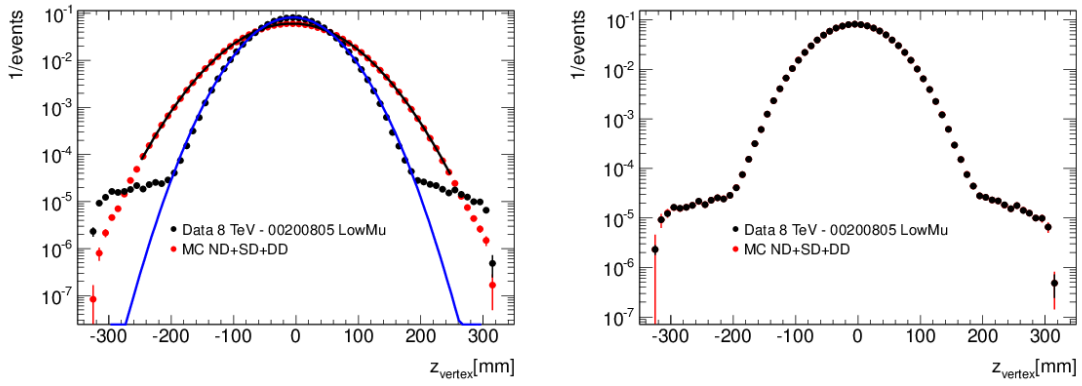

(a) **(b)**

Figure 8.1: The z-position of the vertex in data and MC **(a)** before and **(b)** after reweighing the MC distribution to fit with data.

8.2 MBTS as absolute reference

The MBTS is the most inclusive trigger, and is both fast and reliable. In order to determine how inclusive it is, it is determined how efficiently it triggers on the events of interest for the Minimum Bias Analysis. This is denoted as the trigger efficiency of the MBTS, and gives the efficiency of selecting events for study using the `L1_MBTS_1` trigger (like the discussion in Section 6.5 for the ALFA detector).

The trigger efficiency of the MBTS is determined by using a control trigger, triggering randomly on filled bunches at L1, demands two Pixel and three SCT hits at L2, and has no additional requirements at EF. The trigger efficiency, $\epsilon_{\text{trig}}(n_{\text{sel}})$, is then calculated as

$$\epsilon_{\text{trig}}(n_{\text{sel}}) = \frac{\#\text{ events triggered by control trigger passing the MBTS trigger}}{\#\text{ events triggered by control trigger}} \tag{8.3}$$

parametrized in terms of n_{sel}. In Figure 8.2, the resulting trigger efficiency for MBTS is shown. The work is presented in [97], and the author has not been involved, though it has been included here as it has been integrated into the correction package.

8.3 Tracking efficiencies

Using the MC, a qualified guess on the tracking efficiency of ATLAS is made by the number of reconstructed tracks matched to a generated particle, $N_{\text{rec}}^{\text{matched}}$, to the number

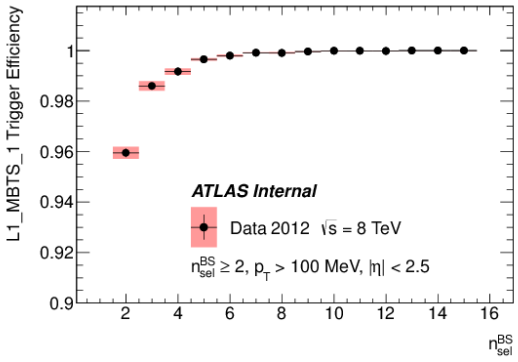

Figure 8.2: Efficiency of triggering on ≤ 1 hit in the MBTS in order to get the event sample discussed in the text, as a function of tracks selected in the analysis [97].

of generated charged particles N_{gen}, as

$$\epsilon_{\text{trk}}(p_T, \eta) = \frac{N_{\text{rec}}^{\text{matched}}(p_T, \eta)}{N_{\text{gen}}(p_T, \eta)}, \tag{8.4}$$

determined for given p_T and η bins. The matching between a generated particle and the reconstructed track is done using a cone-matching algorithm in the $(\eta - \phi)$ plane. It associates the generated particle to the track with the smallest $\Delta R = \sqrt{(\Delta\eta)^2 + (\Delta\phi)^2}$ within a cone of radius 0.15, when the particle trajectory is compatible with the position of one of the pixel hits of the track [92]. The resulting distribution for the tracking efficiency in η and p_T can be seen in Figure 8.3.

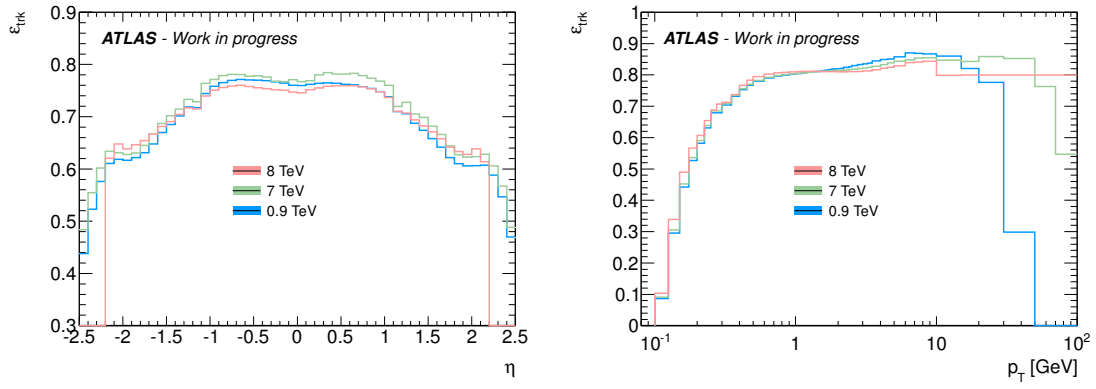

(a) **(b)**

Figure 8.3: Efficiency of the tracking reconstruction as a function of **(a)** η or **(b)** p_T of the track, compared to previously studied center of mass energies a.

Issues caused by configuration

From Figure 8.3(a) is is seen that the tracking efficiency is noticeably lower for 8 TeV than the latest analysis on 7 TeV data. Looking into the details of the reconstruction configuration, it was found that the initial configuration for the tracking algorithm was different from the configuration in the analysis done on 7 TeV data. The configuration used in exclusive high p_T analyses had erroneously been used in the initial 8 TeV configuration. This has been changed in order to have a configuration comparable to the 7 TeV analysis.

Moreover, a high tracking efficiency is favored, as it leaves less room for uncertainties on the particles that did not get reconstructed. The initial and final configuration for the tracking algorithm in the 8 TeV analysis is presented in Table 8.1 compared to the 7 TeV analysis.

A test sample of the non-diffractive MC with the final configuration was produced. It can be seen in Figure 8.4 that the effect of the changed configuration is especially significant on low p_T tracks, and the lost efficiency in the η spectrum is recovered.

Table 8.1: Configuration of the tracking algorithm for the previous and present Minimum Bias Analysis (p_T in MeV).

Type:	7 TeV	8 TeV (initial config.)	8 TeV (final config.)
InsideOut	$100 < p_T$	$400 < p_T$	$100 < p_T$
low p_T	$100 < p_T$	$100 < p_T < 400$	$100 < p_T$

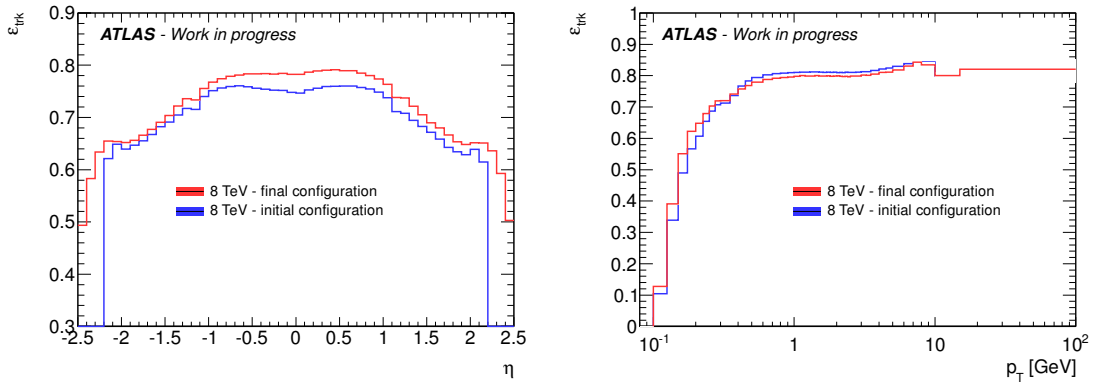

(a) **(b)**

Figure 8.4: Efficiency of the tracking reconstruction for the initial and final configuration for the 8 TeV analysis presented as a function of **(a)** η and **(b)** p_T of the track.

8.4 Vertex efficiency

When the particle hits have been tracked, the tracks are used to determine the position of the vertex. However, not all events that pass the MBTS trigger also have a reconstructed vertex. The vertexing efficiency ϵ_{vrtx} is estimated in bins of n_{sel}, as

$$\epsilon_{\text{vrtx}}(n_{\text{sel}}) = \frac{\#\text{ events with } n_{\text{sel}} \text{ passing the MBTS trigger with vertex reconstructed}}{\#\text{ events with } n_{\text{sel}} \text{ passing the MBTS trigger}} \tag{8.5}$$

and the comparison to previous studies is presented on Figure 8.6(a). In previous studies it was found that the vertexing efficiency for $n_{\text{sel}} = 2$ is dependent on Δz_0^{min}, especially for low p_T^{min}. This observation has been confirmed at 8 TeV, thus for events with $n_{\text{sel}} = 2$, a vertexing efficiency dependent on Δz_0^{min} is used (subdivided for events with $100 < p_T^{\text{min}} < 200$ MeV and for $200 < p_T^{\text{min}}$).

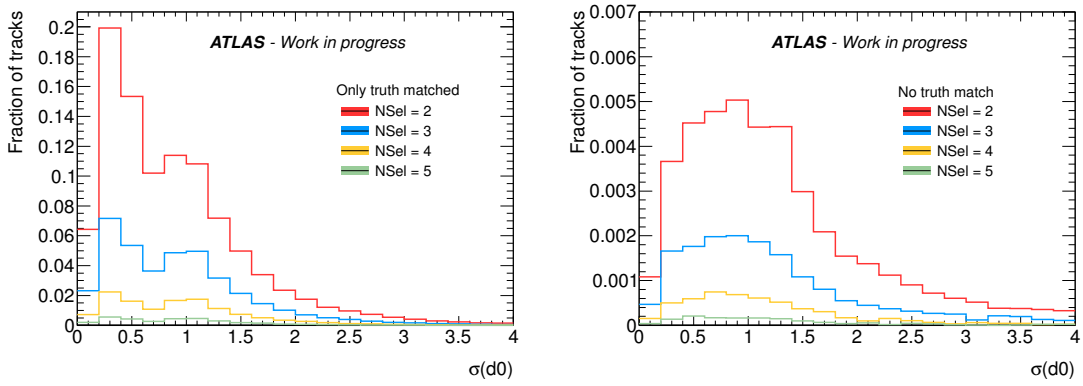

(a) **(b)**

Figure 8.5: Distribution of σ_{d0} of the tracks in MC that was **(a)** matched to truth particles **(b)** not matched to a truth particle, in events where no vertex was reconstructed.

Issue caused by configuration

As for the tracking efficiency, the vertexing efficiency is not comparable to the efficiency in previous studies. It was discovered that the initial requirement on σ_{d0} (describing the uncertainty of the transverse distance to the beam spot) was more restrictive than it had been in the 7 TeV analysis. As can be seen from Figure 8.5(a), one finds in simulation that for events where no vertex was reconstructed, the tracks have a broad distribution in σ_{d0}. This is especially important to consider for truth matched MC tracks (i.e. tracks correctly matched to generated particles).

For the initial configuration of the vertexing algorithm, only tracks with $\sigma_{d0} < 0.9$ mm were used. From Figure 8.5, it can be concluded that this is indeed too strict a cut, as this excludes a lot of correctly reconstructed tracks, i.e. not fakes. It has been observed that the low p_T tracks are more degraded than the high p_T tracks. A cut on σ_{d0} can be used to exclude fake tracks (i.e. tracks reconstructed when no particle was present), because the fakes are expected to have worse precision as they do not stem from smoothly allocated hits [93], which is visible from Figure 8.5(b). Therefore the more tight/robust cut makes sense for normal runs with high pile-up, but in the Minimum Bias Analysis, which includes the low p_T tracks, it becomes important to loosen the cut. For the final configuration, this cut was relaxed to be $\sigma_{d0} < 5$ mm, in correspondence with the 7 TeV analysis. In Figure 8.6(b), the comparison between the initial and final configurations is presented, showing a significant effect, resulting in the vertexing efficiency of the 8 TeV that is in better agreement with the 7 TeV data. Notice that full data sets are compared, but only a limited non-diffraction (ND) sample of MC with the final configuration is used.

Beam background

One might notice that the vertex efficiency in data approaches but does not reach 100 % even for vertices with a high number of tracks. This was suggested to be caused by beam background, for which the longitudinal tracks can not be tracked back to a vertex, which could give rise to events with no reconstructed vertex. An obvious test to see whether a possible vertex stems from a collision or just beam background, is to look at the time between hits in the MBTS. If the vertex is caused by the collision, one would expect to see particles arriving at the two opposite MBTS plates at roughly the same time. Whereas

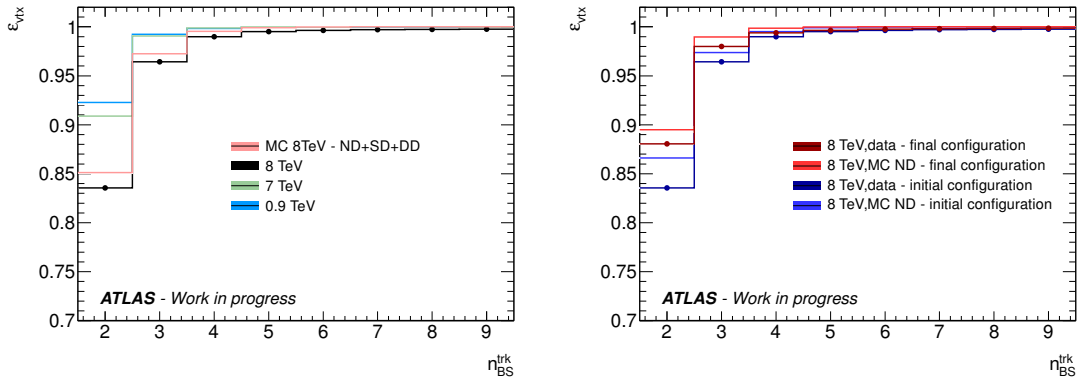

(a) **(b)**

Figure 8.6: Efficiency of the vertexing reconstruction in n_{sel} **(a)** comparing to other center mass energies **(b)** comparing the different configurations. The errors are comparable with the size of the line.

a track from beam background is expected to pass ATLAS along the z-axis, giving rise to a signal first in the MBTS on the A side, and then later a signal in the MBTS on the C side, or vice versa. Flying with the speed of light this would take approximately 7.2 m/$c \approx 24$ ns. Dividing events into those with a reconstructed vertex, and those with no reconstructed vertex, it is seen from Figure 8.7 that many events with no reconstructed vertex exhibit exactly that behavior. When removing these beam background events, by requiring $\Delta t_{\text{MBTS}} < 20$ ns, the loss in vertex efficiency is recovered, which can be seen on Figure 8.8.

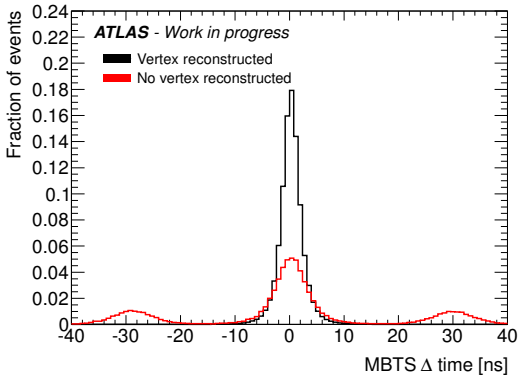

Figure 8.7: Distribution of events as a function of time difference for counts in the MBTS.

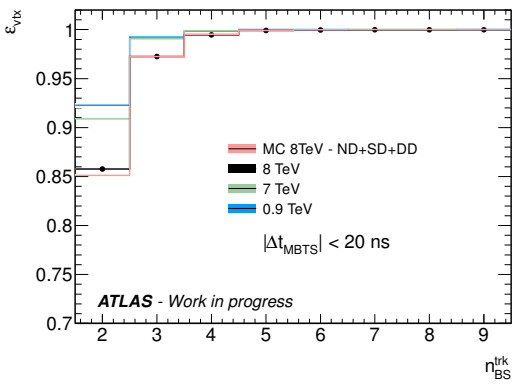

Figure 8.8: Including constraint on time difference for hits in the MBTS.

8.5 Tracks migrating from outside of kinematic range

Particles outside the kinematic region considered, may be reconstructed as a track inside the kinematic region. The fraction of tracks, for which this happens, is determined using MC, by comparing reconstructed tracks inside the kinematic region with generated particles outside the kinematic region. This is an effect caused mainly by finite resolution, and without correction, the sample may be biased by this effect. As seen from Figure 8.9

the effect is small, mostly affecting low momentum tracks, or tracks close to the edge of the η acceptance region used in the analysis.

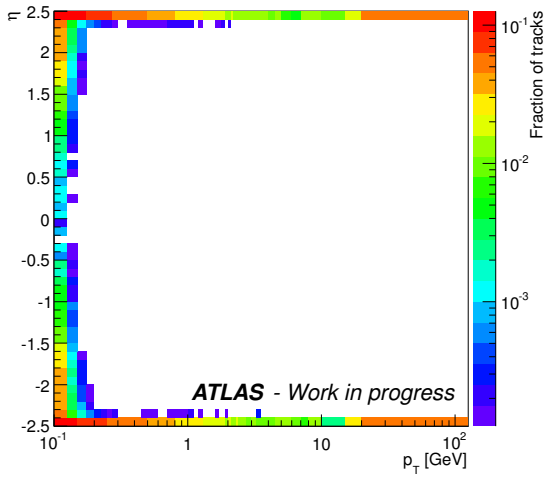

Figure 8.9: Fraction of tracks migrating from outside the kinematic range of the Minimum Bias Analysis.

8.6 Secondaries

As mentioned in the previous chapter, particles with a mean lifetime $\tau > 0.3 \cdot 10^{-10}$ s produced either at the pp interaction or by subsequent decay of particles with shorter life times are considered as primaries. Any particles produced after this time span will be considered as secondaries.

These are decay products of primary particles that were created at the collision, particles created from interactions with the material and photons pair producing an electron and a positron via interactions with nuclei or atomic electrons [63]. The fact that the electron positron pair production is possible means that the secondaries will be subdivided in electrons and non-electrons.

As the author was responsible for the work on the secondaries investigation at 8 TeV, the analysis shall here be presented in more detail.

Template fitting

From MC the d_0 distribution of primary particles, electron and non-electron secondaries from the events are extracted in 10 p_T ranges: 9 bins in the interval $[100; 550]$ MeV, and one for tracks with $p_T > 550$ MeV. These distributions are used as templates $t_i(d_0)$ each scaled with a corresponding factor f_i, to be determined. For each p_T-bin the combination of templates

$$f_{\text{fit}}(d_0) = f_{\text{prim}} \cdot t_{\text{prim}}(d_0) + f_{\text{el}} \cdot t_{\text{el}}(d_0) + f_{\text{non-el}} \cdot t_{\text{non-el}}(d_0) \tag{8.6}$$

is fitted to the d_0 distribution in data. From this one can extract the fraction of primaries and secondaries (comprised of electrons and non-electrons contributions) in data.

Using the constraint on overall normalization, i.e. that

$$\sum_{d_0\text{bins}} (t_{\text{prim}}(d_0) + t_{\text{el}}(d_0) + t_{\text{non-el}}(d_0)) = \sum_{d_0\text{bins}} f_{\text{fit}}(d_0), \tag{8.7}$$

only two of the factors need to be determined.

A χ^2-fit of f_{fit} to data is made for each factor $f_i \in [0 : 2]$. The fit is only done using tracks with $|d_0| > 1.5$ mm, which is outside the signal region of the Minimum Bias Analysis, thus giving an independent measure of the fraction of secondaries for the analysis. The fit is done for 11 different intervals of d_0 with $|d_0|_{\text{min}} \in [1.5 : 6.5]$ mm, in 0.5 mm steps. This is done in order to estimate how large a systematic error is made from choosing a certain fit range.

An example of the method can be seen on Figure 8.10 where the tracks within $|d_0| > 3$ mm are fitted for two different intervals in p_T. It shows that the method is less sensitive to the electron template at higher p_T, where the distribution is nearly flat in the fitting region.

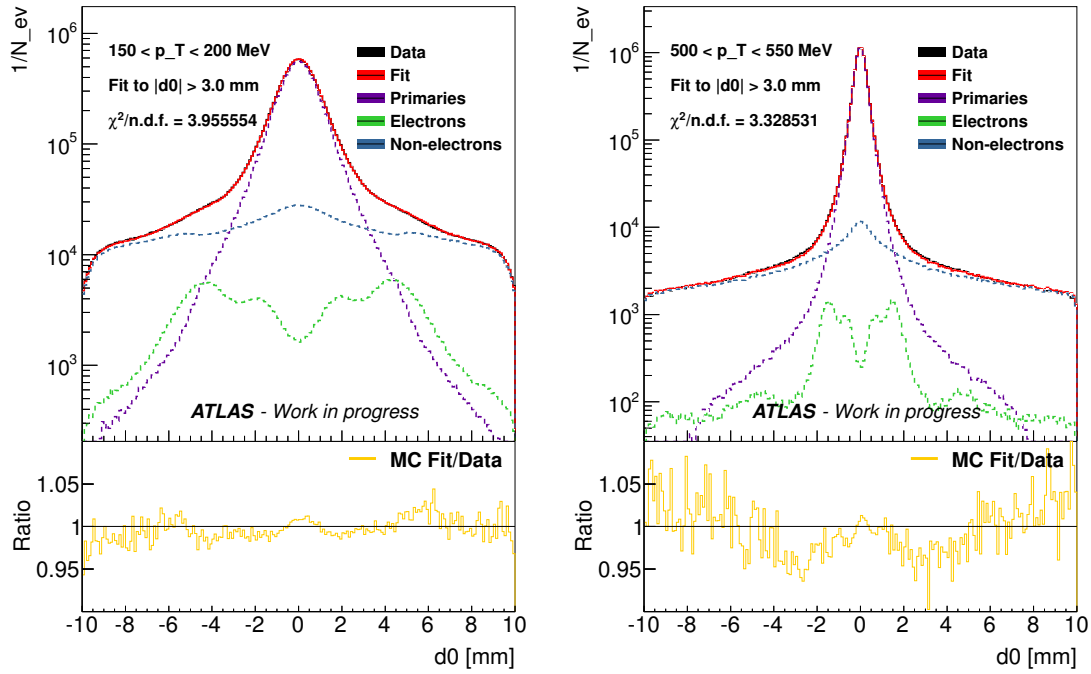

(a) **(b)**

Figure 8.10: The MC templates for primaries and electron and non-electron secondaries are fitted to data, shown here for tracks within $|d_0| > 3$ mm with **(a)** with $150 < p_T < 200$ MeV **(b)** with $500 < p_T < 550$ MeV.

Systematic errors on the secondaries

For calculating the fractions of secondaries in the data set, a couple of choices have been made. This introduces systematic uncertainties of the calculated fraction of secondaries. The four effects considered will be added in quadrature

$$\sigma_{\text{syst}} = \sqrt{\sigma^2_{\text{templates}} + \sigma^2_{\text{interval}} + \sigma^2_{\text{MC}} + \sigma^2_{\text{background}}}, \tag{8.8}$$

and the individual contributions shall be discussed in the following.

The individual systematic uncertainties were chosen to be set conservatively as the total systematic uncertainties on secondaries only play a minor role compared to the material uncertainty (as mentioned in Section 7.5).

Separate or combined template for secondaries As not all fitting ranges are sensitive to the electron template for at high p_T, one might instead use one combined template for the secondaries. On Figure 8.11, the ratio between using separate and combined templates on the resulting secondary fraction is presented. From this it is estimated that the choice of using either separate or combined templates introduces a 11% systematic uncertainty for the first p_T-bin, 8% for the last p_T bin, and 2% for the rest of the p_T-bins.

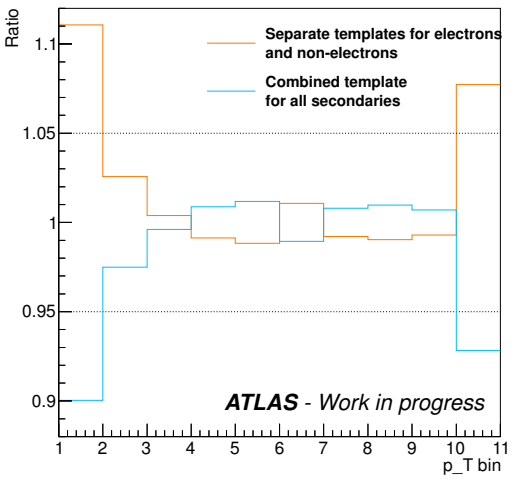

Figure 8.11: The fraction of secondaries using separate or combined templates for electron and non-electron secondaries compared to each other.

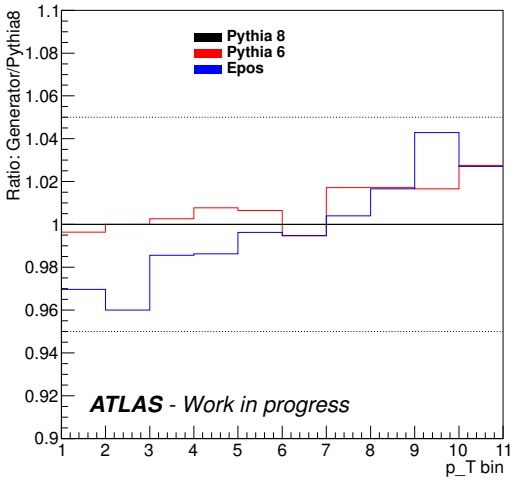

Figure 8.12: Ratio of the resulting secondary fraction to the fraction resulting from using another generator than Pythia 8.

Choice of MC generator As concluded in Section 7.6 the Pythia 8 MC generator seems to perform best at describing the minimum bias distribution in η. Therefore it was chosen to produce the templates for the secondaries analysis. In order to assess the possible systematic effects of using that specific MC, the procedure was also done with the Pythia 6 and the Epos MC generator. In Figure 8.12 the ratio to Pythia 8 is shown. From this a 5% systematic uncertainty is seen to account for using a specific MC generator.

Choosing specific $|d_0|$ intervals The fit is done in 11 different $|d_0|$ intervals, though as mentioned the fit is less sensitive to the electron template for higher p_T. Using all the $|d_0|$ intervals for the higher p_T bins would not make sense. Inspecting the templates in the different p_T bins (presented in Appendix B.7), one can set some approximate limit on $|d_0|_{\text{min}}$, presented in Table 8.2 are the limits used in this analysis.

Table 8.2: Limits on the minimal $|d_0|_{\text{min}}$, for the intervals used in fitting the secondary templates.

p_T interval	$\lvert d_0\rvert_{\text{min}}$
100-250	6.5 mm (all intervals)
250-300	5 mm
300-400	4 mm
400-550	3.5 mm
550-up	only combined templates

In order to determine the systematical uncertainty introduced by using this selection, the ratio to the average value of secondary fraction for the varies d_0 intervals is presented in

Figure 8.13. From this a 1% systematical uncertainty is ascribed to the effect of choosing specific d_0-intervals for the first three p_T bins, 5% for the next four bins, and 10% for the rest.

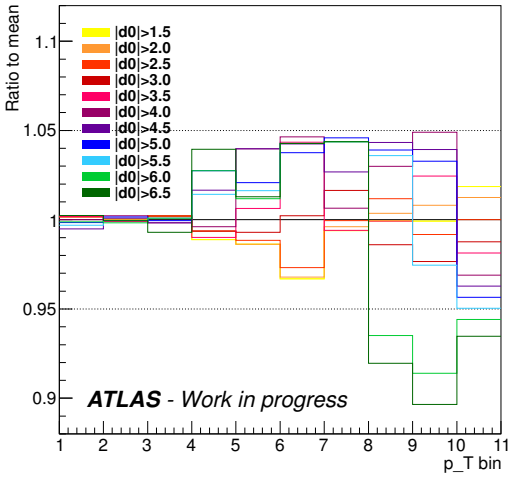

Figure 8.13: Ratio between the resulting secondary fraction to the fraction resulting from using just one $|d_0|$ interval.

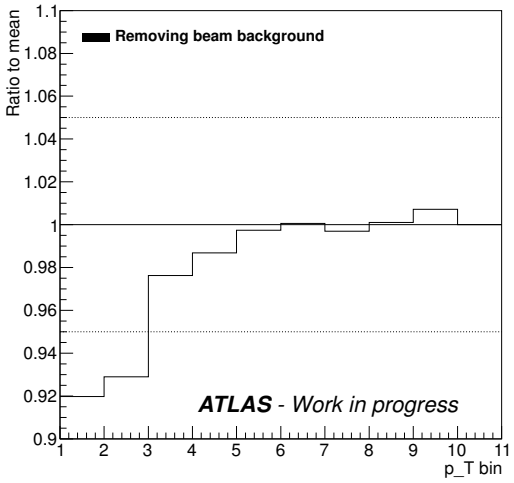

Figure 8.14: Ratio of the resulting secondary fraction to the fraction resulting from removing beam background.

Secondaries from background From studying the events in BGRP 4 (isolated unpaired bunches) it was found that the beam background track distribution is up to an order of magnitude higher than signal for tracks with $100 < p_T < 150$ MeV, comparable for tracks with $150 < p_T < 200$ MeV, and an order of magnitude lower for higher p_T tracks [98]. Furthermore, it was found that the beam background is more uniformly distributed in $|d_0|$ than signal events, thus a higher fraction of beam background is expected for high $|d_0|$.

In order to remove the background the following cuts are used:

$$\begin{aligned} N^{\text{Pixel}}_{\text{Unassociated}} &< 1000, \\ N^{\text{BLayer}}_{\text{Unassociated}} &< 300, \end{aligned} \tag{8.9}$$

which from simulation is seen to remove $\sim 90\%$ of the background and only $\sim 10^{-6}\%$ of the signal events [98].

With the cuts in (8.9) a non vanishing fraction is removed, as seen in Figure 8.15, though the beam background is as expected only an issue for low p_T events (all p_T ranges are presented in Appendix B.8).

The fraction of secondaries are calculated for the sample when the beam background is removed, and in Figure 8.14 the ratio of the resulting secondary fraction is compared to the average. From this the systematic uncertainty linked to the removing the beam background using the cuts in (8.9), can be found to be 8% for the first two bins, 3% for the next two and 1% for the rest.

Result for the secondaries

From the fitted factors f_i, the fraction of secondaries in the signal region is calculated, and the average is found. The results from the different d_0 intervals are correlated as they

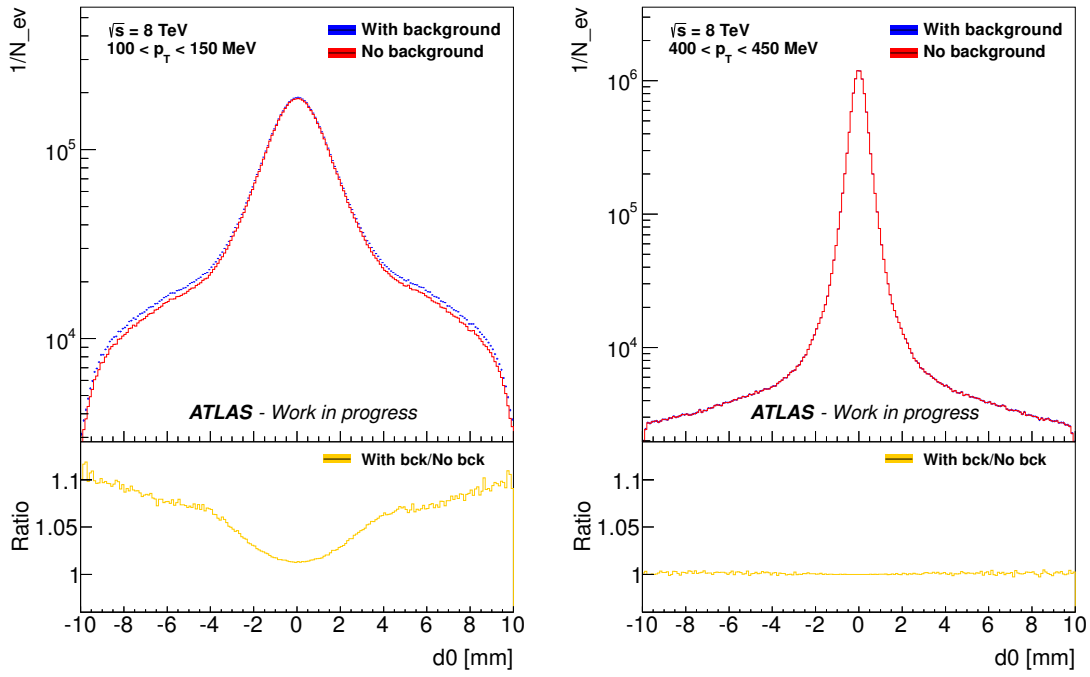

(a) **(b)**

Figure 8.15: The d_0 distribution of tracks in data with(without) the cut on supposed background mentioned in (8.9) is shown in red(blue), along with the ratio between the two distributions for **(a)** events with $100 < p_T < 150$ MeV **(b)** events with $400 < p_T < 450$ MeV.

constitute subsets of each other, thus the spread of the measurements rather indicates the range on values for the mean, than the real uncertainty.

For $100 < p_T < 550$ MeV separate templates are used, though only the fit intervals stated in Table 8.2 For $p_T > 550$ MeV, a combined template for the secondaries is used, as the electron template is not sensitive to the fit outside the signal region (as discussed above). The resulting fraction of secondaries is presented in table 8.3, with the spread (approx.) and systematical uncertainties (syst.) indicated.

Table 8.3: Fraction of secondary particles in signal region, indicated with the spread on the average and the conservative estimates of the systematic uncertainties, for tracks with $|\eta| < 2.2$.

p_T interval	fraction of data which is secondaries	electron contribution
100-150	0.1166 ± 0.01237. (approx.) ± 0.0224 (syst.)	$(8.80 \pm 0.94)\%$
150-200	0.0741 ± 0.00499. (approx.) ± 0.0346 (syst.)	$(7.97 \pm 0.54)\%$
200-250	0.0460 ± 0.00192. (approx.) ± 0.0100 (syst.)	$(8.58 \pm 0.36)\%$
250-300	0.0404 ± 0.00143. (approx.) ± 0.0224 (syst.)	$(10.30 \pm 0.37)\%$
300-350	0.0363 ± 0.00110. (approx.) ± 0.0173 (syst.)	$(11.36 \pm 0.34)\%$
350-400	0.0357 ± 0.00106. (approx.) ± 0.0173 (syst.)	$(13.36 \pm 0.40)\%$
400-450	0.0363 ± 0.00106. (approx.) ± 0.0173 (syst.)	$(12.06 \pm 0.35)\%$
450-500	0.0347 ± 0.00096. (approx.) ± 0.0283 (syst.)	$(11.34 \pm 0.32)\%$
500-550	0.0343 ± 0.00094. (approx.) ± 0.0283 (syst.)	$(12.36 \pm 0.34)\%$
550-up	0.0307 ± 0.00076. (approx.) ± 0.0141 (syst.)	-

8.7 Final weights

Having calculated every contribution to the weights introduced in the beginning of this chapter, it now serves to look at the result.

The event weight, w_{event}, introduced in (8.1) depends on n_{sel}, and it is seen from Figure 8.16 that only events with $n_{\text{sel}} < 5$ are corrected with a significant weight.

The track weight, w_{trk}, introduced in (8.2) is shown in Figure 8.17 for tracks with any set of (p_T, η). Due to the relative small variation in the track weight for $p_T > 150$ GeV compared to the lower p_T bins, the plot shows $1/w_{\text{trk}}$, in order to cover all the interesting aspect in one figure. It is basically the efficiency of the tracking algorithm that gives the distribution of Figure 8.17, as the corrections for secondaries and tracks migrating lowers the weight.

These distribution can now be used for any analysis within this kinematic region of the phase space, and that is where the focus shall be, when looking at the single diffractive sample in the next chapter.

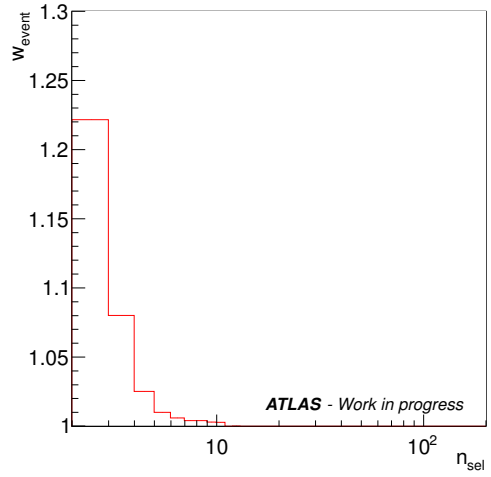

Figure 8.16: The weight applied to each event corresponding to the number of tracks passing the selection n_{sel}.

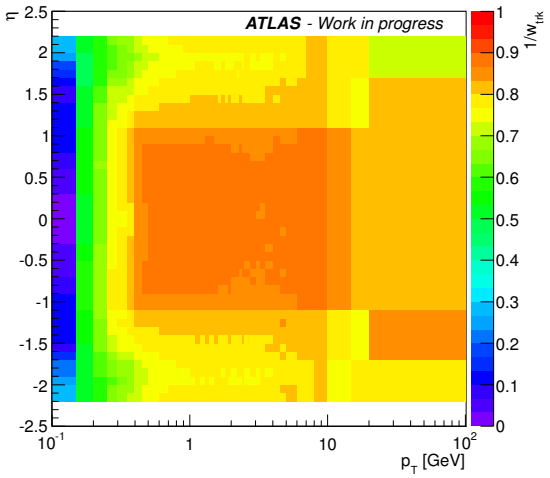

Figure 8.17: Weight applied to each track dependent on its p_T and η. On the figure $1/w_{\text{trk}}$ is plotted to make the variations most visible.

9

Studying diffraction

In this chapter the initial work on the analysis of diffractive events is presented. The complete analysis could not be completed due to amount of validation needed to be done. Furthermore, the analysis is lacking a complete MC for comparison as well as a final set of alignment parameters for the ALFA detectors.

The work in this chapter shall focus on some data preparatory tasks and the investigation of single diffraction (SD) and central diffraction (CD) with ALFA. This shall serve as part of the first results on diffractive processes using ALFA, hopefully encouraging future discussions.

9.1 Data samples

In this study, the runs 206881, 206884 and 206885 are studied. They are all from the same fill, and both ALFA and ATLAS were running. The beams were prepared in the high $\beta^* = 90$ m configuration described in Section 3.3, and running with a center of mass energy of 8 TeV. The three runs supply data of good quality corresponding to an integrated luminosity of 18.64 nb^{-1} and 6.22 nb^{-1} for run 206881 and 206885 respectively. Run 206884 is too heavily biased, as will be apparent from the discussion of the good luminosity blocks, and is therefore excluded from the analysis.

LHC fill information

Both runs 206881 and 206885 took data from LHC fill 2836, which contained 108 paired and 4 unpaired bunches in each beam. Each bunch started with $\sim 81.0 \cdot 10^9$ protons, i.e. a reduced number compared to normal runs.

Bunch group configuration In run 206881 the first part of the run was dedicated to elastic events, which meant that for LB 120-336 only 3 bunches were put in BGRP 1 (paired), whereas all 108 bunches were in BGRP1 for LB 337-647 dedicated for the diffractive events. The run 206885 had all 108 bunches in BGRP 1.

The bunch group settings for run 206881 mean triggering for only 3 bunches in the first part, and on all 108 bunches in the rest of the run, as the triggers are specific for each BGRP as mentioned. For simplicity run 206881 shall only be included with LBs ≥ 337.

Determining good luminosity blocks

For most normal runs, a data quality flag is set for each luminosity block (LB), signaling whether that block should be used for analysis. Normally this is described by a *good runs list* (GRL) covering only the LBs that can be used for physics analysis for a given run [99]. As the runs 206881, 206884 and 206885 were special, no GRL was prepared, and thus this was determined by the author.

On the ATLAS side, various flags can signal whether some LBs should be regarded bad. The most important is the ATLAS flag *ready for physics*, an overall flag signaling whether the detector was in a good enough condition for the data to be used for physics analysis. As presented in Table 9.1, the main part of the runs were by ATLAS flagged to be ready for physics. In ALFA some other problems were observed [86], summarized in Table 9.1.

Table 9.1: Luminosity block flags for the runs used in this study.

Run	ATLAS Ready for physics	ALFA issues (ALFA det. affected)
206881	125-647	631-647 (Too high voltage on (1))
206884	3-97	3-97 (PMF problems (2,3,4)) 34-44 (No trigger signal (7))
206885	3-111	3-111 (PMF19 off (3), ignored)

Some other flags were raised within the LBs ready for physics for these runs. The flags "b tagging flags" and "ZDC disabled" are tolerable as neither the ZDC nor b tagging is need in this analysis. The flag "Pixel barrel 5-7 % not ready" is tolerable [100]. The flag "Global LHC high beta flag" is perfectly fine, as this was indeed a high β^* run. The flag "Inconsistency between BGRP used for triggering and used for calculating the luminosity" was raised only for LBs 125-337, which were those chosen only to trigger on some of the filled bunches, thus the flag makes sense. It is however not relevant in this analysis, where only LBs $\geq$ 337 shall be used.

In the ALFA community the following criteria must be fulfilled for the good LBs [101]:

- Luminosity block length > 60 s;
- Dead time $< 5\%$;
- ALFA detector in final position (as noted in the ALFA runs document [102]).

Using the package TriggerRatesFromCOOL[103], the information on dead time, LB length and ALFA detector position could be extracted from the COOL database per LB. The position of the ALFA detector is read out and stored according to a LHC time, which must be converted to the LBs, such that only LBs are accepted where the ALFA detector position matches the one presented in the ALFA runs document. The resulting bad LBs are presented in Table 9.2.

Table 9.2: Luminosity block concluded bad for the runs used in this study.

Run	Bad Luminosity blocks
206881	1-125,140,141,144,145,150,151,168,170,182,334-336,340,341, 347,349,350,352,370,373,374,377,378,383-388,397,398,631-647
206884	1-97 (entire run)
206885	1-3,6,12,13,15,21,22,66,79,82,83,91,111,113-128

9.2 Monte Carlo simulations

The development of MC simulations including ALFA in a full simulation together with ATLAS was still ongoing for most of the time of the project. A lot of effort was put into testing and comparing results from MC to data. However a validated MC sample was not obtained before the deadline of this thesis.

For this study a MC sample containing events at 7 TeV with full detector simulation has been used for determining the contamination of beam background, as that sample showed the least problems (referred to as 7 TeV MC). The effects of non-diffractive (ND) events are studied with a toy MC, which uses standard Pythia 8 with no detector simulation (produced and described in Ref. [52]). The MCs are used with precaution, rather to get approximate guidelines than as a proper measure for a theoretical prediction. This also means that a lot of the selection, cleaning and correction of the sample of single diffractive events, which is the regular approach, could not be done using the available MC.

9.3 Event selection of single diffraction

The single diffractive (SD) event candidates are selected as those events in good LBs satisfying the simple criteria that there must be

- activity in the ALFA detectors of one armlet.
- some activity in ATLAS.

One forward flying proton with a low scattering angle and one proton dissociating is ATLAS is basically the signature of a single diffraction process (as argued in Section 5.6). In the following this selection shall be quantified by the cuts used in the analysis, with the short hand notation for these cuts given in parenthesis. The most loose cuts are introduced first, and then more cuts are used to tighten the selection. It is important to be able to quantify the loss of signal events with a given cut, and by specifying the cuts, the loss can be probed more easily.

Activity in ALFA

In order to read out the event, there must be triggering in ALFA (SD trigger), corresponding to a single diffractive event, therefore `L1_ALFA_SDIFF5/6/7/8` is required.

There should correspondingly be at least one track in the ALFA detectors (SD track pattern), however a track multiplicity of one (multiplicity = 1) is required. In events with multiple tracks, one must consider which track is the most likely to originate from a single diffractive process, and this was not investigated due to time constraints.

In order to suppress the contamination from elastic events, the events fulfilling the elastic back-to-back cuts discussed in Section 6.2 are excluded (No golden elastics). This cut is made more tight excluding events with tracks in an entire elastic arm (No elastic like tracks).

Finally a veto on the three other armlets is introduced, in order to distinguish the different cases of diffraction (Veto on other arms).

Activity in ATLAS

The MBTS is used to signal activity in ATLAS, and triggering in the MBTS on the opposite side of the proton tagged in ALFA is required. `L1_MBTS_1_A/C_ALFA_C/A` was unprescaled from LB 370, as the only trigger useful for reading out single diffraction. Thus it shall be used as the primary trigger requirement.

A vertex in ATLAS is also required in order to reconstruct the diffracted proton better, and to have some distribution in ATLAS to investigate.

Resulting cutflow

In Table 9.3 resulting cutflow is presented. In the given order of applying the cuts, the multiplicity cut and vetoing on other tracks in other armlets are seen to have relatively small but non-negligible effects. However, especially the removal of golden elastics and requiring some activity in ATLAS removes most events. It is a bit surprising to see that requiring some activity in the MBTS opposite the surviving proton appears to be more restrictive than requiring a reconstructed vertex in ATLAS.

Table 9.3: Cutflow for selected single diffractive events.

Cut	Run 206881	Run 206885
Total events in sample	20612504	3091165
Good Luminosity blocks	12460135	2909592
SD trigger	12417931	2893650
SD track pattern	8657120	2030193
Multiplicity = 1	8459477	1985802
No golden elastics	6602224	1581391
No elastic like tracks	6432283	1542952
Veto on other armlets	6186080	1487292
≥ 1 vertex	4812298	1149029
SD+MBTS trigger	4306239	1035955

Background contribution

The above event selection is very loose and does not ensure a clean sample of SD events. One must take into account the residual beam halo that might leave a track in one or more ALFA detectors. Combinations of beam halo, mis-triggered elastic events and a ND event in ATLAS will imitate SD events.

The background contamination as well as the loss of signal due to the cuts must be investigated before the final cross section measurement. Though as will become apparent in the following, the MC did not seem to describe data well, and thus these investigations were not pursued further.

9.4 Kinematic reconstruction

For events with a track in ALFA and a vertex in ATLAS (alternatively the beam spot), the kinematic properties (i.e. energy E and momentum p_x, p_y) can be reconstructed. This is done using the Copenhagen Reconstruction package, details on the method and precision can be found in Ref. [52].

9.5 Cross section determination

The tight selection of single diffractive events shall in this section be used for the investigations of the cross section measurement.

The distribution of the relative energy loss ξ of the surviving proton in single diffractive events is expected to fall off as $1/\xi$ (as expected from the differential cross section discussed in Section 2.7). In Figure 9.1, it is seen that this is indeed what is used in the 7 TeV MC. Though this behavior is not seen for the single diffractive like events in data. Apart from the broadening of the peak due to a finite detector resolution, a plateau like structure is seen, starting around $\xi \sim 0.05$, and falling off due to the acceptance [52] around $\xi \sim 0.15$.

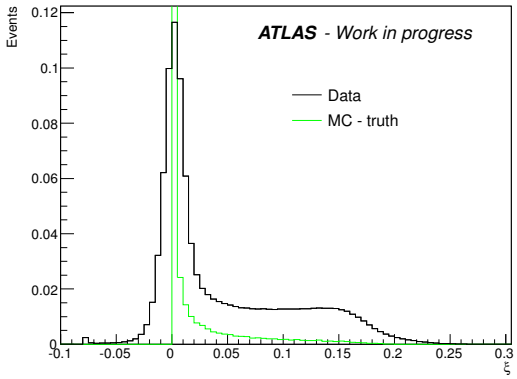

Figure 9.1: Distribution in ξ for the tight selection of single diffractive events.

In earlier experiments is has been observed that the differential cross section approximately falls off with $1/\xi$ for events with low t, but shows the same plateau like structure for events with higher t [104, 38]. As concluded in Section 2.7, the distribution is also expected to fall off exponentially with t, thus the data sample should be dominated by low t events, as no cut on t has been introduced. It has been argued that Regge theory is only applicable for 5 GeV$/s < \xi < 0.1$ [17], however the plateau is still visible within this region, and an explanation is still needed. Some of the possible effects are discussed below.

Effect from selection

Requiring activity in ATLAS corresponds to favoring events where the dissociated system is less boosted, i.e. larger ξ. In Ref. [52] it is indeed found that the vertex requirement has a significant effect. It biases the distribution towards higher ξ, since the vertex reconstruction requires multiple tracks in ATLAS.

Effect from non diffractive processes

From simulations (discussed in Ref. [105]) it is apparent that some of the plateau like structure can be due to final state particles flying all the way out to the ALFA detectors. As the cross section of ND rises with ξ this would indeed induce the plateau. This can be investigated with simulations, and as no full simulation was present, a toy Pythia MC was used in Ref. [52] to confirm the possibility. A fraction of events from ND events could indeed reach ALFA, resulting in the introduction of a plateau, though it was concluded that the ND contribution could not account for the entire plateau like structure.

Another way of determining the ND contamination is by studying rapidity gaps. As discussed in Section 2.5 the ND events are characterized by exponentially suppressed rapidity gaps, whereas diffractive events should exhibit a much flatter distribution in rapidity gaps. It has been discussed that the ND contribution should be an order of magnitude lower on events with a rapidity gap $\Delta\eta^{\mathrm{F}} \sim 3-4$ [37]. Here, $\Delta\eta^{\mathrm{F}}$ is the rapidity gap measured from the edge of the FCAL ($|\eta| = 4.9$).

For this run, problems with the calorimeters have been observed [106], therefore the same measure can not be used in this study. Instead the rapidity gap measured from the edge of the ID, $\Delta\eta_{\mathrm{ID}}$, will be used.

In Figure 9.2 it is seen that the rapidity gap measured from the same side as the proton in ALFA is non-exponentially suppressed, compared to the rapidity gaps measured from

the opposite side of the proton. Furthermore, these distributions of rapidity gaps in the 7 TeV MC are similar to the observation in data. This indicates that the rapidity gaps size may be used to suppress ND contamination.

In Figure 9.3, the distribution in ξ is presented for five intervals of rapidity gap. It is observed that none of the rapidity gap selections influence the plateau like shape. The only change is an enhancement of the low ξ peak. This can be due to the fact that the distinction between SD and ND gets smaller for higher ξ (see Section 2.6).

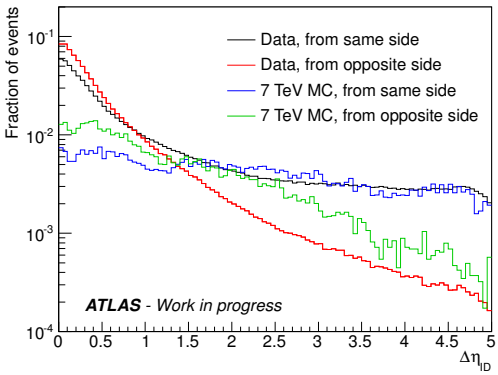

Figure 9.2: Rapidity gap size in data and in the 7 TeV MC, measured from the same side of the surviving proton, and from the opposite side of the surviving proton.

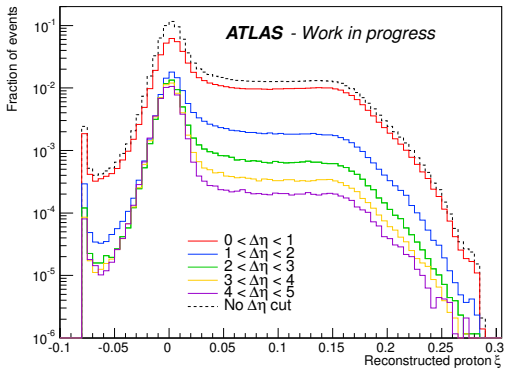

Figure 9.3: Distribution in ξ of single diffractive events with different rapidity gap.

Effects from beam background

The rate of beam halo events in ALFA has been studied both for 7 and 8 TeV and found to be significant [107]. An effort must be done in distinguishing single diffractive events from beam halo.

In order to understand the beam background contamination the unpaired bunches can be used. In these events one can be quite certain that the signal in a detector is not due to interactions in ATLAS, hence they must come from noise or beam background.

On Figure 9.4 it can be seen that there is a correlation between the x position in ALFA and θ_x, introduced in Chapter 5. It is sensible to conclude that the beam background is responsible for the additional ellipsoidal shape in data, which is not visible for single diffractive events in the 7 TeV MC. This is the only distribution where such a simple distinction could be made (other correlations of variables in ALFA can be seen in Appendix B.9).

Therefore one can cut out the ellipsoidal shape and subdivide the events in those inside (signal dominated) and outside (beam background) of the main banana shaped signature in the $(x - \theta_x)$ plane. In Figure 9.5 it is seen that the contribution of the background events in the ellipse is negligible, mostly responsible for the events in the underflow bin ($\xi < -0.05$).

Concluding remarks on the cross section measurement

The plateau like structure was persistent over a range of tests. Without the full correct MC it is too difficult to separate SD events from background, and thus a determination of the cross section can not be performed properly. Data driven methods were not approached.

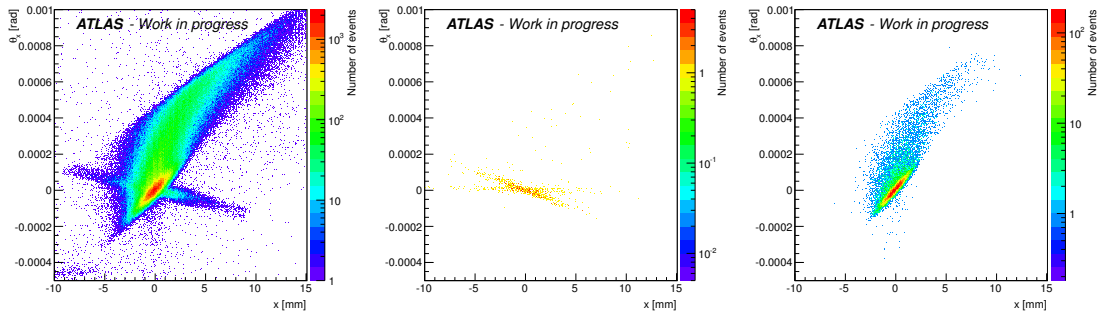

Figure 9.4: Distribution of hits in the $x-\theta_x$ plane for the ALFA detectors for **(a)** single diffractive like events in data **(b)** beam background **(c)** single diffractive events in the 7 TeV MC.

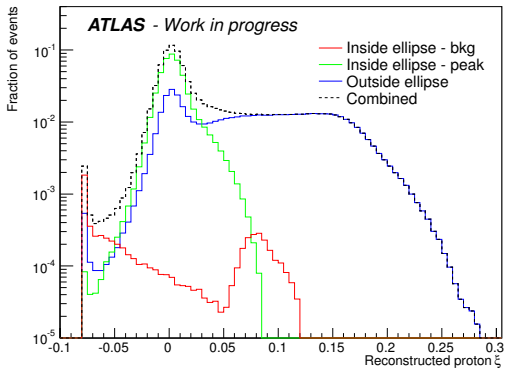

Figure 9.5: Distribution in ξ for the single diffractive sample for various $x - \theta_x$ selections.

9.6 Charged particle multiplicity analysis

Like the distributions in the Minimum Bias Analysis, the distributions of tracks in ATLAS shall here be discussed. For this analysis, the most restricted sample is used, i.e. only events passing all the cuts presented in Table 9.3.

The corrections discussed for the Minimum Bias Analysis has been applied to the distributions presented here, though no unfolding is done.

Track multiplicity distribution in η

In Figure 9.6 the charged track multiplicity distribution of all single diffractive like events as well as for one armlet only is presented. It is compared to the distribution of tracks fulfilling the selection criteria of the Minimum Bias Analysis.

Whether the diffractive like events have slightly more of the events in the high η regions can not be concluded. However, comparing to the SD like events of just one armlet, the expected asymmetry of more tracks in the opposite side of the tagged proton is apparent. The system of particles from the dissociated proton is heavily boosted, due to the low momentum transfer between the two protons, and this is exactly what is observed.

Comparing the track distribution of all SD like events to the minimum bias selection, SD like events with a tagged proton in different sides of ATLAS are expected to be symmetric in η. This can be tested, using the assumed symmetry of ATLAS to compare

the four different cases of SD like events. In Figure 9.7 the η of the tracks of all the SD like events have been multiplied with the sign on z of the surviving proton.

The distributions are identical within 1%, except at high eta, where the discrepancy could be an effect of an asymmetry in ATLAS. If this is the case, it will become apparent from the final Minimum Bias Analysis.

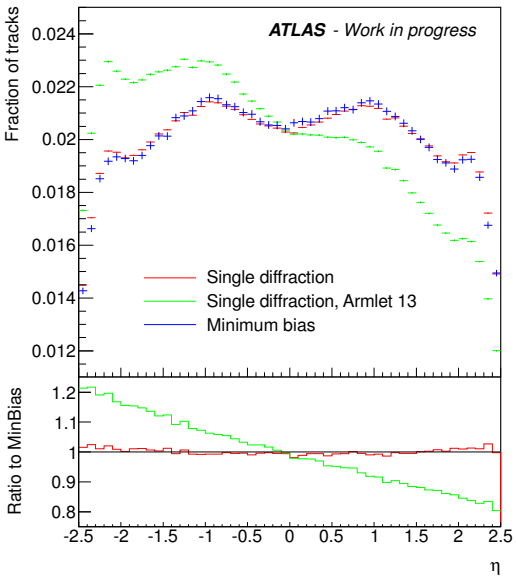

Figure 9.6: Charged track multiplicity distribution in η, comparing single diffractive events to minimum bias events.

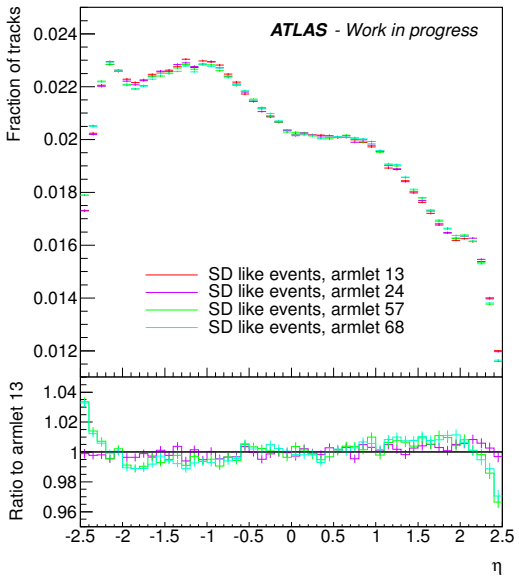

Figure 9.7: Charged track multiplicity distribution in η, for the tagged proton in either of the four armlets of ALFA, signed to the sign of z of the surviving proton (each distribution normalized to one).

Track distribution in ξ bins

Looking at the charged track multiplicities for protons in different bins of relative energy loss ξ, it is seen as expected that for low momentum transfer, the diffracted system is more boosted than for high momentum transfer events. On Figure 9.8, the comparison is made for various bins to the average distribution of the sample. Each distribution is normalized to one, in order to draw a clearer conclusion on their shapes.

The difference in the track density in ATLAS for the different selections of ξ is quantified in Table 9.4. In events where the surviving proton has lost more energy, a higher number of tracks are seen in ATLAS. This can be ascribed to two different effects. First of all, the low relative energy loss ξ of the surviving proton means that the system of particles from the dissociated proton is boosted more, and thus a larger fraction of the tracks will hit ATLAS at high η, and vice versa for high ξ events. Secondly, a high ξ means that there is more energy available in the dissociating proton, resulting in a broader rapidity plateau. Assuming that an equal amount of particles is produced in each interval of η within the rapidity plateau, the high ξ results in more particles. A MC study might indicate which effect is most significant.

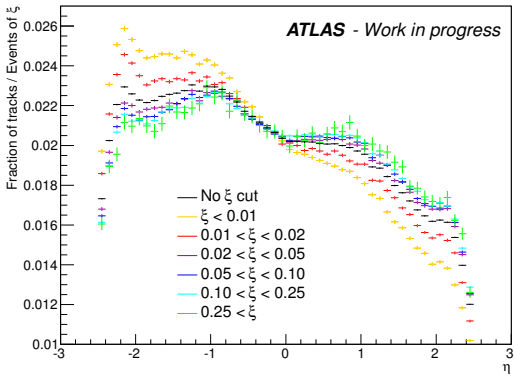

Figure 9.8: Charged track multiplicity distribution in η, for various bins of ξ (each distribution is normalized to one).

Table 9.4: Single diffractive events in each ξ bin presented on Figure 9.8.

SD armlet 13	N_{events}	N_{tracks}	Avg. number of tracks pr. event
$0 < \xi < 0.005$	210814	1581498	7.50186
$0.005 < \xi < 0.015$	245189	2121398	8.65209
$0.015 < \xi < 0.040$	143567	1782494	12.4158
$0.040 < \xi < 0.100$	163675	2263617	13.8299
$0.100 < \xi < 0.200$	197221	2911012	14.7602
$0.200 < \xi < 1$	10768	162810	15.1198
Total	973412	10849857	11.1462

Track multiplicity distribution in p_T

Looking at the charged track multiplicity distribution in p_T, the different cases of SD like events are seen to be identical. Generally producing more low p_T tracks, than in the typical minimum bias sample.

9.7 A brief look at central diffractive like events

A selection of central diffractive events was done using the same type of criteria as in the single diffractive like events (presented in Table 9.3), now demanding trigger and tracks to correspond to any of the four possibilities of detecting centrally diffracted protons. No requirement on activity in the MBTS is set, and the activity in ATLAS is ensured by demanding a reconstructed vertex. The naming scheme shall be that of Section 5.6, where e.g. CD 1357 corresponds to central diffractive events selected by having tracks in ALFA detectors 1, 3, 5, & 7.

Events recorded

In Table 9.5, the number of events corresponding to the selection is reported. The two diffracted protons must in central diffractive events be expected to exchange particles independent of each other, and thus show an equal number of events in the four possible cases. Though there are clearly more events corresponding to CD 1368 and CD 2457, the combination of detectors corresponding to an elastic like event. As only the golden elastic like events were rejected, there might still be a significant contamination of elastic events, as there will in general be many more elastic events than central diffractive events.

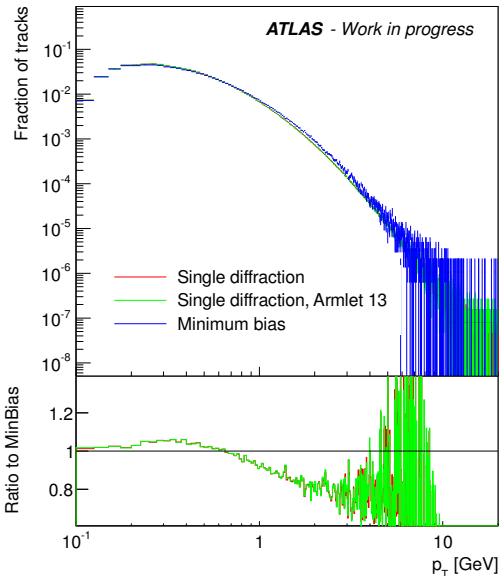

Figure 9.9: Charged track multiplicity distribution in p_T, comparing single diffractive events to minimum bias events.

Thus it does not come as a surprise to see more central diffractive like events in the arms similar to where one finds the elastic events.

Table 9.5: List over recorded CD events in the data samples.

CD arm	Run 206881	206885
CD 1357	46358	10877
CD 1368	77647	17682
CD 2457	98472	22169
CD 2468	41459	9602
Total	263936	60330

Signature in ϕ distribution of charged tracks

One feature expected to be significant in central diffractive events is the distribution of charged tracks in ϕ. From conservation of momentum, the distribution of CD 1357 and CD 2468 events are expected to be biased towards the opposite side of the direction of the diffracted protons. This means that in CD 1357 events additional tracks are expected around $\phi \sim -\pi/2$ and fewer around $\phi \sim \pi/2$ (vice versa for CD 2468). As opposed to CD 1368 and CD 2457, for which no significant bias is expected.

As seen on Figure 9.10 this is exactly the signature present in data. While the difference is not large within errors, it is evident that there is a discrepancy between the different arms.

As for the single diffractive events, one could exploit the symmetry of ATLAS to mirror the distribution for e.g. CD 2468 in ϕ, to compare the two cases better. However, it can be seen from both Figure 9.10(a) and Figure 9.10(b) that the there is some asymmetry in ϕ for ATLAS, and the comparison does not give any new information (see Appendix B.10).

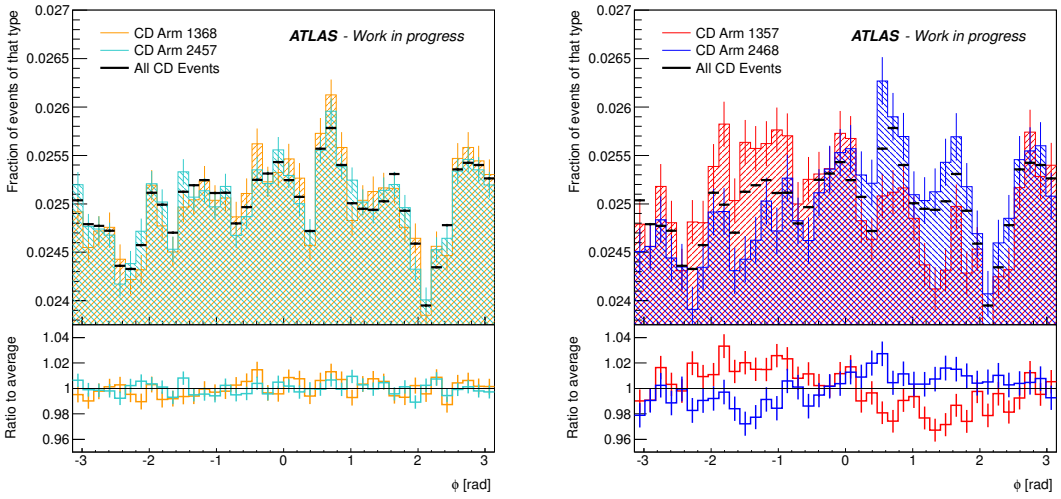

(a) **(b)**

Figure 9.10: Distribution in ϕ for the charged tracks in central diffractive like events comparing **(a)** CD 1368 and CD 2457 or **(b)** CD 1357 and CD 2468, to the average distribution of selected central diffractive events.

10

Conclusion

In this thesis the focus has been on diffractive processes in proton-proton collisions. Understanding that the foundation for theoretical predictions in QCD, the factorization theorem, only is a good approximation at high energies, motivated the discussions of the Regge formalism. As this is still the dominant theoretical description of soft processes, an understanding of the framework is a natural part of studying diffraction. Regge theories can account for the behavior of the total cross section by introducing the pomeron. However, the Regge theories still lack a proper prediction of the cross sections for diffractive processes.

When measuring diffraction, one has typically been characterizing the events by the size of the rapidity gap. Though using detectors installed in Roman Pots, ALFA makes it possible to tag the protons from diffractive events in collisions at higher energies than ever before.

The performance of the ALFA trigger system has been investigated. It was concluded to perform very well, with an efficiency of more than 99.4% for diffractive like events, and even higher for elastic like events. Furthermore, the tracking efficiency of protons in ALFA, originating from diffractive like events, has been investigated. An investigation of showering in ALFA using MC could help reaching a deeper understanding of the results presented on this matter.

The Minimum Bias Analysis is one of the main studies of soft processes in ATLAS. The contributions to the analysis was presented, with focus on the detector response, also important for the charged track multiplicities in diffractive events. Due to unforeseen difficulties, the Minimum Bias analysis could not be concluded within the timescale of the thesis.

The data recorded with ATLAS and ALFA at $\sqrt{s} = 8$ TeV has been prepared and was used to make a very tight selection of single diffractive candidate events. These were used to show that the charged track multiplicities of in ATLAS, are clearly biased towards the opposite side of the surviving proton. A lot of effort was put into validating a MC for describing diffraction in ATLAS at 8 TeV, though the development did not reach a conclusion. As such no detailed event selection was done, and the characteristic plateau in the presented ξ distribution could not be explained. The brief look at central diffractive like events demonstrated that they exhibit the characteristics expected from momentum consideration.

This thesis represents a first approach at measuring diffraction with ATLAS and ALFA. Further investigations must be done in understanding some of the unresolved issues, and to make the results more conclusive. For this it would be ideal to reach a validated MC resembling data to a degree where it can be used for further comparison and a better event selection.

ALFA provides a great opportunity to investigate diffraction. The work presented in this thesis has demonstrated, that there are many interesting phenomena which need to

be further investigated. Let this be the first step towards rediscovering the rich field of proton proton diffraction, still not understood.

Appendices

A

Derivations

A.1 Rapidity of high energetic particle

Approximating for $p_z \to \infty$

$$E = \sqrt{\mathbf{p}^2 + m^2} = \sqrt{\mathbf{p}_\perp^2 + p_z^2 + m^2} \simeq p_z + \frac{1}{2}\frac{\mathbf{p}_\perp^2}{p_z} + \frac{1}{2}\frac{m^2}{p_z} \tag{A.1}$$

Then it can be found that in that approximation that the rapidity for the particle is

$$\begin{aligned} y &= \frac{1}{2}\ln\frac{E + p_z}{E - p_z} \\ &\simeq \frac{1}{2}\ln\frac{2p_z + \frac{1}{2}\frac{\mathbf{p}_\perp^2}{p_z} + \frac{1}{2}\frac{m^2}{p_z}}{\frac{1}{2}\frac{\mathbf{p}_\perp^2}{p_z} + \frac{1}{2}\frac{m^2}{p_z}} \\ &= \frac{1}{2}\ln\frac{4p_z^2 + \mathbf{p}_\perp^2 + m^2}{\mathbf{p}_\perp^2 + m^2} \\ &\simeq \frac{1}{2}\ln\frac{4p_z^2}{\mathbf{p}_\perp^2 + m^2} \\ &\simeq \ln\frac{2p_z}{\sqrt{\mathbf{p}_\perp^2 + m^2}} \end{aligned} \tag{A.2}$$

A.2 The S-matrix formalism

The scattering (or simply S) matrix is the linear operator which takes the initial state $|i\rangle$ to the final state $|f\rangle$ of a scattering process:

$$S|i\rangle = |f\rangle \tag{A.3}$$

Thereby the probability for the process to occur is

$$P_{i\to f} = |\langle f|S|i\rangle|^2 \tag{A.4}$$

It is customary to write the S-matrix elements in terms of the transistion matrix T or the scattering amplitude A:

$$S_{if} \equiv \langle f|S|i\rangle = \delta_{if} + i\langle f|T|i\rangle = \delta_{if} + iT_{if} \tag{A.5}$$

$$= \delta_{if} + i(2\pi)^4\delta^4(p_f - p_i)A(i \to f) \tag{A.6}$$

where $A(i \to f)$ is the relativistic scattering amplitude.

Looking into the cross section of the scattering process of $1 + 2 \to n$ particles. The differential cross section is given as [10]:

$$d\sigma = \frac{1}{\Phi}|A(i \to f_n)|^2 d\Pi_n, \tag{A.7}$$

which summed over all final states integrated over the phase space gives the total cross section

$$\sigma_{\text{tot}} = \sum_n \int d\Pi_n \frac{1}{\Phi}|A(i \to f_n)|^2, \tag{A.8}$$

where f_n is denoting the n-particle final state, Φ is the incident flux and $d\Pi_n$ is the Lorentz invariant phase space for n particles in the final state given explicitly as:

$$d\Pi_n = \prod_{j=1}^{n} \frac{d^4 p'_j}{(2\pi)^3} \delta(p'^2_j - m_j^2)(2\pi)^4 \delta^4 \left(p_1 + p_2 - \sum_{j=1}^{n} p'_j \right) \tag{A.9}$$

And the incident flux is

$$\begin{aligned}
\Phi &= 2E_1 2E_2 |\mathbf{v}^1 - \mathbf{v}^2| \\
&= 4E_1 E_2 \left| \frac{\mathbf{p}_1}{E_1} - \frac{\mathbf{p}_2}{E_2} \right| \\
&= 4|E_2 \mathbf{p}_1 - E_1 \mathbf{p}_2| \\
&= 4\left[E_2^2 \mathbf{p}_1^2 + E_1^2 \mathbf{p}_2^2 - 2E_1 E_2 |\mathbf{p}_1||\mathbf{p}_2| \right]^{\frac{1}{2}} \\
&= 4\left[(\mathbf{p}_2^2 + m_2^2)\mathbf{p}_1^2 + (\mathbf{p}_1^2 + m_1^2)\mathbf{p}_2^2 - 2E_1 E_2 |\mathbf{p}_1||\mathbf{p}_2| \right]^{\frac{1}{2}} \\
&= 4\left[(\mathbf{p}_2^2 + m_2^2)(\mathbf{p}_1^2 + m_1^2) + \mathbf{p}_1^2 \mathbf{p}_2^2 - m_1^2 m_2^2 - 2E_1 E_2 |\mathbf{p}_1||\mathbf{p}_2| \right]^{\frac{1}{2}} \\
&= 4\left[E_1^2 E_2^2 + \mathbf{p}_2^2 \mathbf{p}_1^2 - m_1^2 m_2^2 - 2E_1 E_2 |\mathbf{p}_1||\mathbf{p}_2| \right]^{\frac{1}{2}} \\
&= 4\left[(E_1 E_2 - |\mathbf{p}_1||\mathbf{p}_2|)^2 - m_1^2 m_2^2 \right]^{\frac{1}{2}} \\
&= 4\left[(p_1 \cdot p_2)^2 - m_1^2 m_2^2 \right]^{\frac{1}{2}} && \text{(A.10)} \\
&= 4\left[\left(\frac{s - m_1^2 - m_2^2}{2} \right)^2 - m_1^2 m_2^2 \right]^{\frac{1}{2}} \\
&= 2\left[\left(s - 2m^2 \right)^2 - 4m^4 \right]^{\frac{1}{2}} \qquad \text{for equal masses} \\
&= 2\left[s^2 - 4sm^2 \right]^{\frac{1}{2}} && \text{(A.11)} \\
&\xrightarrow{s \to \infty} 2s && \text{(A.12)}
\end{aligned}$$

(A.10) holds for $\mathbf{p}_1$ parallel to $\mathbf{p}_2$, and (A.11) is a special case for later use.

Unitarity

Demanding conservation of probability, one arrives at the unitariry of the S-matrix:

$$S^\dagger S = S S^\dagger = \mathbf{1} \tag{A.13}$$

Rewriting the unitarity condition (A.13) in terms of the transision matrix T

$$(\mathbf{1} - iT^\dagger)(\mathbf{1} + iT) = \mathbf{1} \tag{A.14}$$

Meaning that

$$i(T^\dagger - T) = T^\dagger T \tag{A.15}$$

Sandwiching (A.15) between the initial and final state:

$$i\langle f|T^\dagger - T|i\rangle = \sum_n \langle f|T^\dagger|n\rangle\langle n|T|i\rangle, \tag{A.16}$$

meaning

$$2\mathrm{Im}T_{if} = \sum_n T^*_{fn}T_{in} \tag{A.17}$$

Written in terms of the scattering amplitudes one find

$$2\mathrm{Im}A(i \to f) = \sum_n \int d\Pi_n A^*(f \to n)A(i \to n) \tag{A.18}$$

Optical theorem

If the initial and final states are equal, i.e. for the elastic scattering of $(t = 0)$, one gets from (A.18)

$$2\mathrm{Im}A_{\mathrm{el}}(s, t = 0) = \sum_n \int d\Pi_n |A(i \to n)|^2 \tag{A.19}$$

Now comparing (A.19) with (A.8) the optical theroem is found

$$\sigma_{\mathrm{tot}} = \frac{2}{\Phi}\mathrm{Im}A_{\mathrm{el}}(s, t = 0) \xrightarrow{s\to\infty} \frac{1}{s}\mathrm{Im}A_{\mathrm{el}}(s, t = 0) \tag{A.20}$$

Differential cross section of elastic events

One can use (A.7) to determine the differential cross section for elastic process of $1 + 2 \to 3 + 4$. First it can be fruitful to elaborate a bit on (A.9).

$$\begin{aligned} d\Pi_2 &= \frac{d^4p_3 d^4p_4}{(2\pi)^3(2\pi)^3}\delta(p_3^2 - m_3^2)(2\pi)^4\delta(p_4^2 - m_4^2)\delta^4\left(p_1 + p_2 - p_3 - p_4\right) \\ &= \frac{d^3\mathbf{p}^3 d^3\mathbf{p}^4}{(2\pi)^2 2E_3 2E_4}\delta^4\left(p_1 + p_2 - p_3 - p_4\right), \end{aligned} \tag{A.21}$$

using the two first dirac delta function, applying that $\delta(f(x)) = \sum_i \delta(x_i)/f'(x_i)$, for $f(x_i) = 0$. From now on the the derivation will continue for the equal mass case, which is the elastic scattering. Using $\delta^3(\mathbf{p}_1 + \mathbf{p}_2 - \mathbf{p}_3 - \mathbf{p}_4)$ the integration over $d^3\mathbf{p}_4$ can be performed, and the remaining volume element can be written as $d^3\mathbf{p}_3 = |\mathbf{p}_3|^2 d|\mathbf{p}_3| d\cos\theta d\phi$, such that

$$\begin{aligned} d\Pi_2 &= \frac{|\mathbf{p}_3|^2 d|\mathbf{p}_3| d\cos\theta d\phi}{16\pi^2 E_3 E_4}\delta\left(E_1 + E_2 - E_3 - E_4\right) \\ &= \frac{1}{16\pi^2}\frac{|\mathbf{p}_3|^2}{|\mathbf{p}_3|^2 + m^2}\delta\left(\sqrt{s} - 2\sqrt{|\mathbf{p}_3|^2 + m^2}\right) d|\mathbf{p}_3| d\cos\theta d\phi, \end{aligned} \tag{A.22}$$

where the second equal sign used the CM frame. Using again that $\delta(f(x)) = \sum_i \delta(x_i)/f'(x_i)$, for $f(x_i) = 0$ one can write

$$\begin{aligned} d\Pi_2 &= \frac{1}{16\pi^2}\frac{|\mathbf{p}_3|}{2\sqrt{\mathbf{p}_3|^2+m^2}}\delta\left(|\mathbf{p}_3| - \sqrt{\frac{s}{4}-m^2}\right) d|\mathbf{p}_3| d\cos\theta d\phi \\ &= \frac{1}{32\pi^2}\frac{\sqrt{\frac{s}{4}-m^2}}{\sqrt{s/4}} d\cos\theta d\phi \\ &= \frac{1}{32\pi^2}\frac{\sqrt{s^2-4sm^2}}{s} d\cos\theta d\phi. \end{aligned} \tag{A.23}$$

Now using (A.23) and (A.11) in (A.7) we can write up the differential cross section for the exclusive reaction of $1+2 \to 3+4$ of equal masses as

$$\begin{aligned} d\sigma &= \frac{1}{32\pi^2 2\sqrt{s^2-4sm^2}}\frac{\sqrt{s^2-4sm^2}}{s}|A_{\text{el}}(s,t)|^2 d\Pi_n \\ &= \frac{1}{64\pi^2 s}|A_{\text{el}}(s,t)|^2 d\cos\theta d\phi. \end{aligned} \tag{A.24}$$

Now turning to $d\cos\theta$, it can be good to write out t in terms of the scattering angle $\cos\theta$

$$\begin{aligned} t &= (p_1 - p_3)^2 \\ &= m_1^2 + m_2^2 - 2E_1E_2 + 2|\mathbf{p}_1||\mathbf{p}_2|\cos\theta. \end{aligned} \tag{A.25}$$

For equal masses $E_1 = E_2 = \sqrt{s}/2$, and $|\mathbf{p}| = |\mathbf{p}'| = \sqrt{s-4m^2}/2$, as can be seen from (2.28) and (2.29). Isolating $\cos\theta$ in (A.25) gives

$$\cos\theta = 1 - \frac{2t}{s-4m^2}. \tag{A.26}$$

From which we can infer

$$d\cos\theta = \frac{2}{s-4m^2}dt \tag{A.27}$$

Using (A.27) and assuming the differential cross section to be independent of ϕ it is seen that

$$\begin{aligned} \frac{d\sigma}{dt} &= \frac{1}{16\pi s(s-4m^2)}|A_{\text{el}}(s,t)|^2 \\ &\xrightarrow{s\to\infty} \frac{1}{16\pi s^2}|A_{\text{el}}(s,t)|^2 \end{aligned} \tag{A.28}$$

A.3 Expected resolution of ALFA

The resolution on the x-position of a particle hitting the square of width w, can be calculated statiscally assuming a flat distribution over x, as the standard deviation. If we want to say that the particle hit in the center of the square:

$$\sigma_y = \sigma_x = \sqrt{\langle x^2\rangle - \langle x\rangle^2} = \sqrt{\langle x^2\rangle} = \frac{d}{\sqrt{12}} \tag{A.29}$$

since we must have that:

$$\langle x^2\rangle = \frac{1}{d}\int_{-\frac{d}{2}}^{\frac{d}{2}} x^2 dx = \frac{d^2}{12} \tag{A.30}$$

Rotating the square, we find the same resolution as, per error propagation, we find that the error on $x' = \sqrt{x^2 + y^2}$, is given as:

$$\sigma_{x'} = \sqrt{\left(\frac{dx'}{dx}\right)^2 \sigma_x^2 + \left(\frac{dx'}{dy}\right)^2 \sigma_y^2} = \sqrt{\frac{x^2}{x^2+y^2}\sigma_x^2 + \frac{y^2}{x^2+y^2}\sigma_x^2} = \sigma_x \tag{A.31}$$

So for the fibers used, with a width of $w = 500\mu$m, one could expect a uncertainty of 144μm, which is increased to 14.4μm, when using all 10 layers in the MD.

B

Distributions

B.1 Distribution of trigger signals

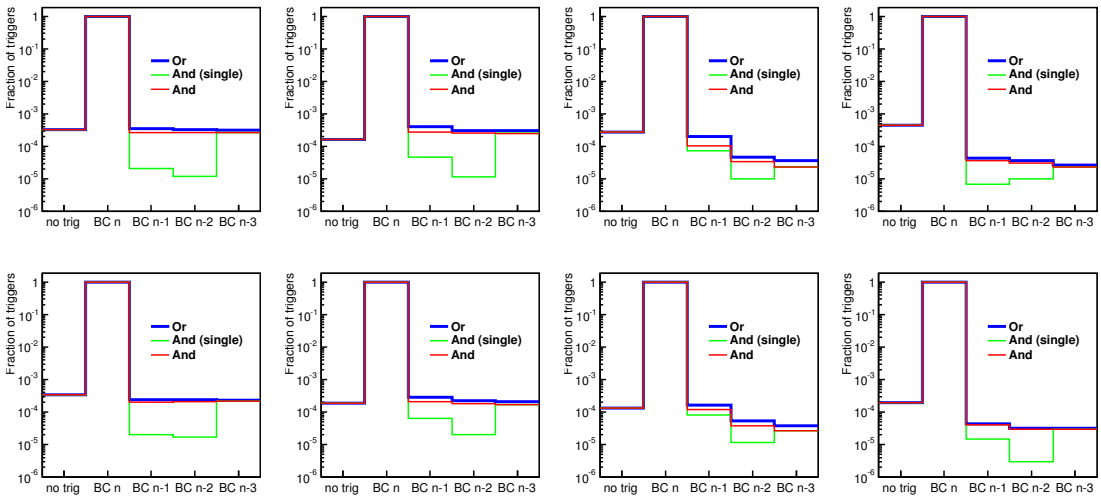

(a)

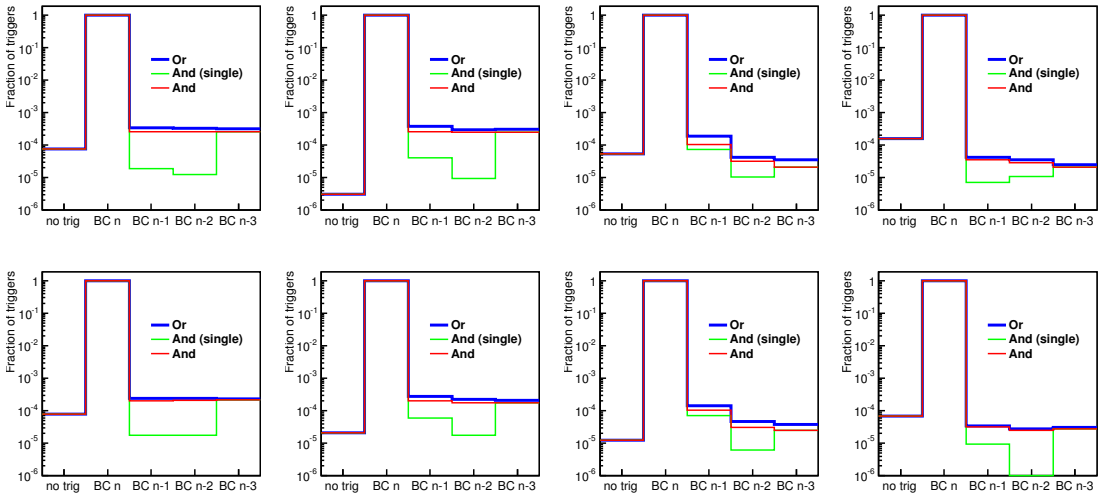

(b)

Figure B.1: The distribution of trigger signal in the 8 ALFA detectors when applying **(a)** no cuts or **(b)** all cuts, for elastic like events.

B.2 Hitmap comparison

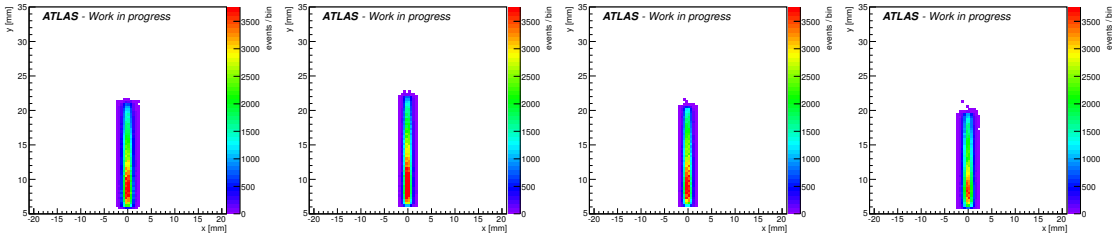

(a) Detector 1 **(b)** Detector 3 **(c)** Detector 5 **(d)** Detector 7

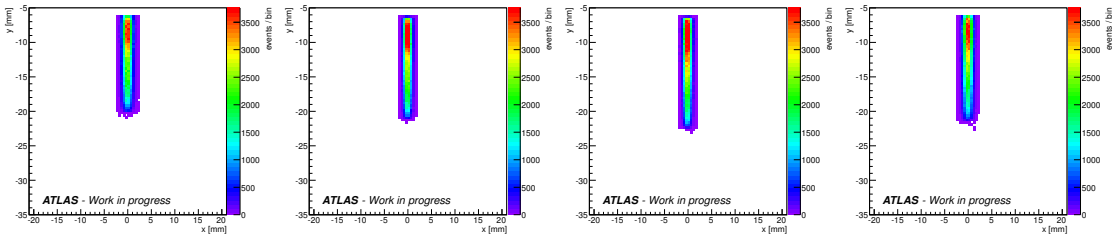

(e) Detector 2 **(f)** Detector 4 **(g)** Detector 6 **(h)** Detector 8

Figure B.2: Hitmap showing the geometrical distribution of elastic events.

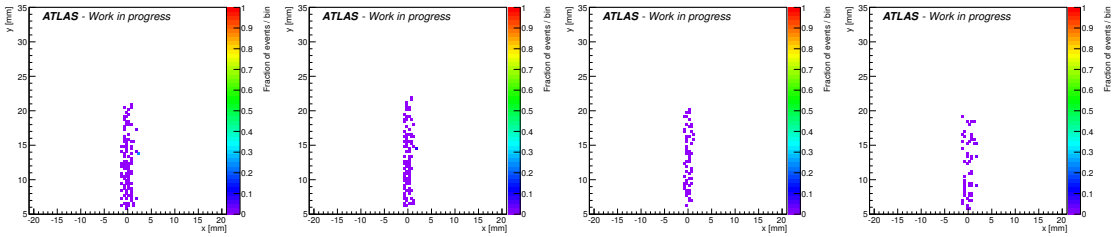

(a) Detector 1 **(b)** Detector 3 **(c)** Detector 5 **(d)** Detector 7

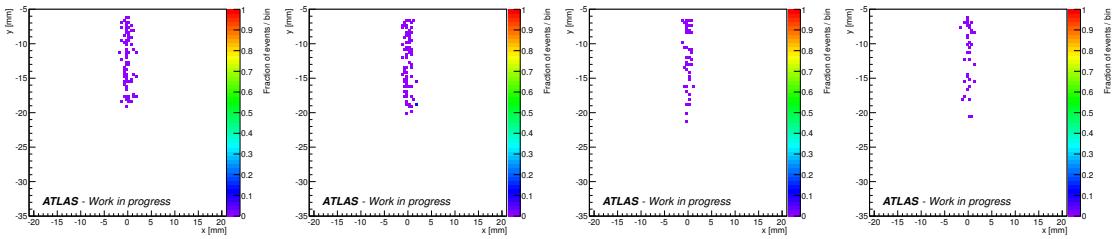

(e) Detector 2 **(f)** Detector 4 **(g)** Detector 6 **(h)** Detector 8

Figure B.3: Hitmap showing the geometrical distribution of the fraction of wrongly triggered elastic events.

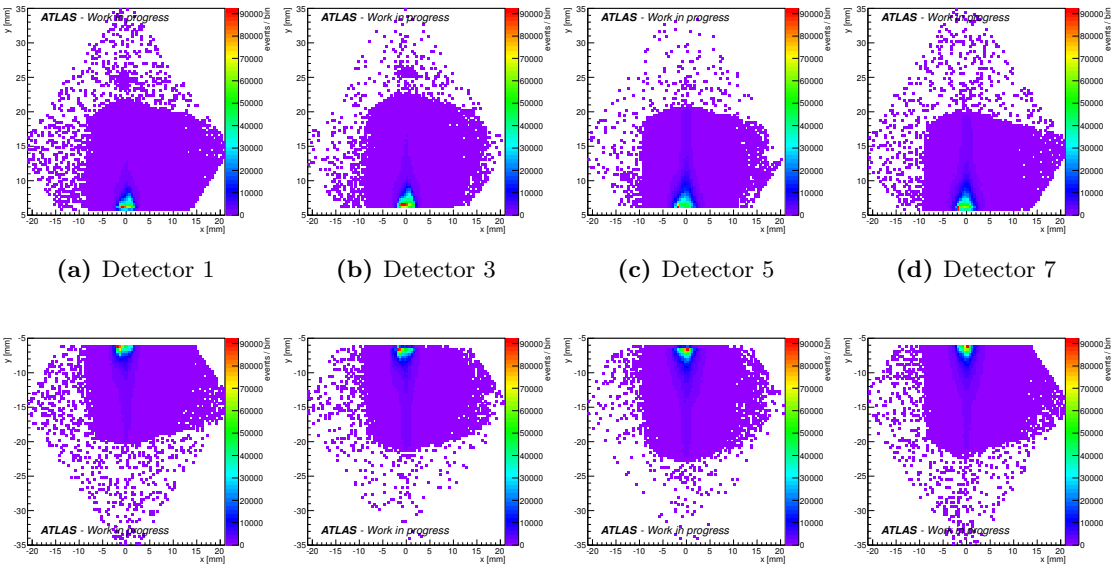

(a) Detector 1 **(b)** Detector 3 **(c)** Detector 5 **(d)** Detector 7

(e) Detector 2 **(f)** Detector 4 **(g)** Detector 6 **(h)** Detector 8

Figure B.4: Hitmap showing the geometrical distribution of diffractive events (no MBTS selection).

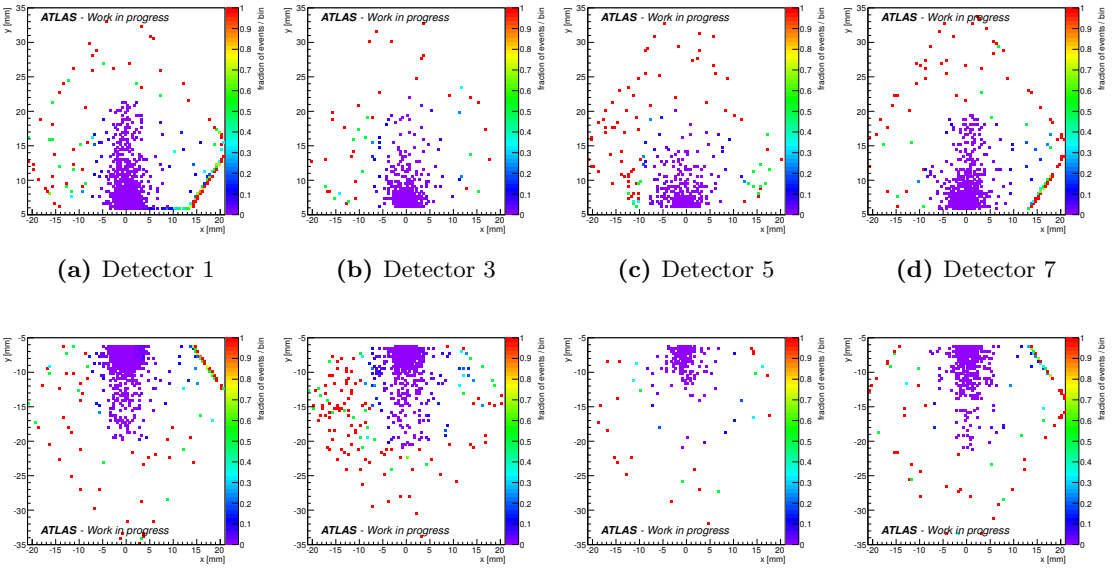

(a) Detector 1 **(b)** Detector 3 **(c)** Detector 5 **(d)** Detector 7

(e) Detector 2 **(f)** Detector 4 **(g)** Detector 6 **(h)** Detector 8

Figure B.5: Hitmap showing the geometrical distribution of the fraction of wrongly triggered diffractive events (no MBTS selection).

B.3 Number of missed triggers

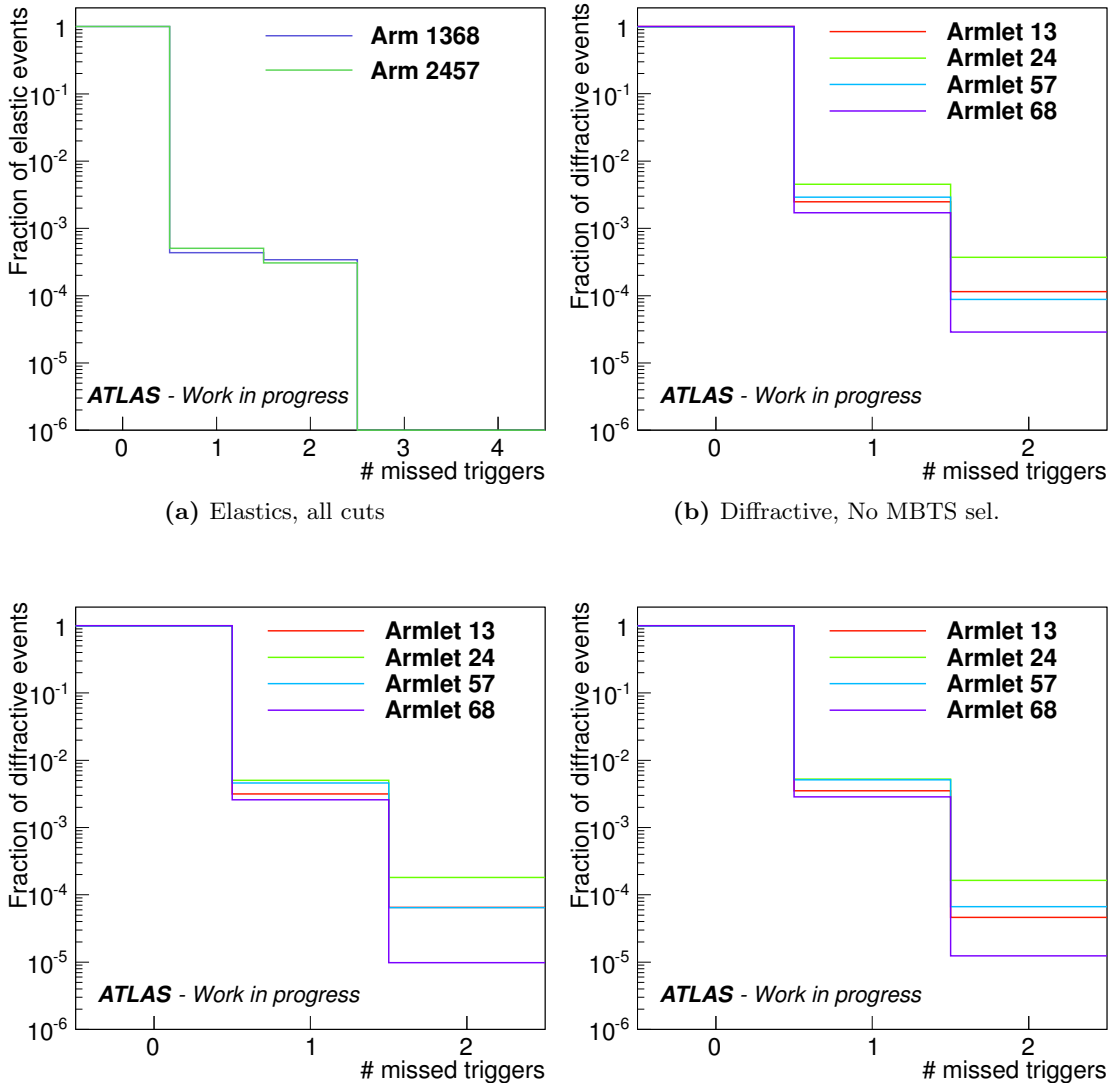

(a) Elastics, all cuts

(b) Diffractive, No MBTS sel.

(c) Diffractive, MBTS1

(d) Diffractice, MBTS2

Figure B.6: Distributions showing the number of missed triggers per events

B.4 Detector trigger efficiency

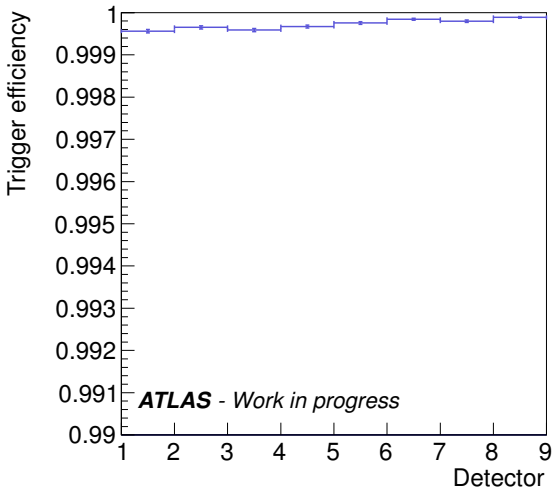

(a) Elastics

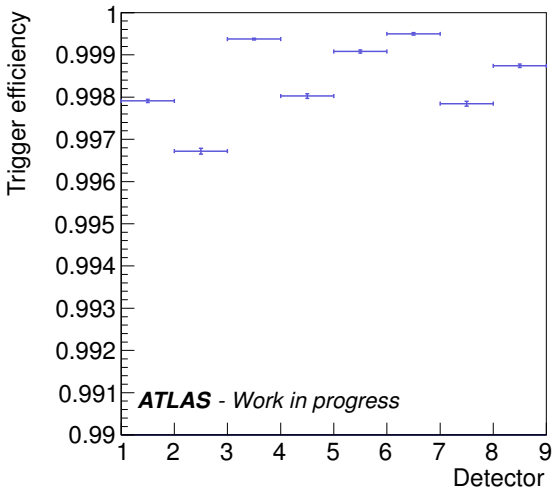

(b) Diffractive, No MBTS sel.

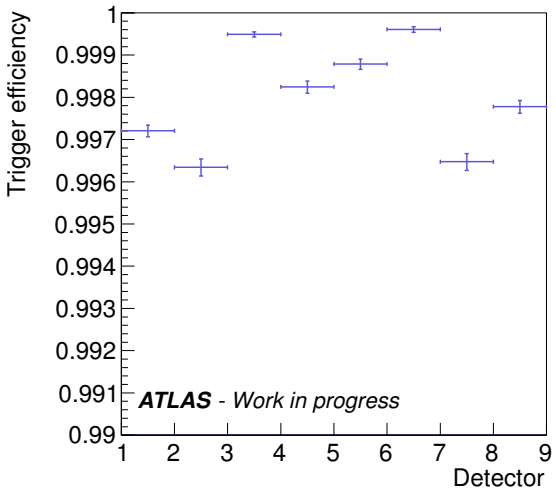

(c) Diffractive, MBTS1

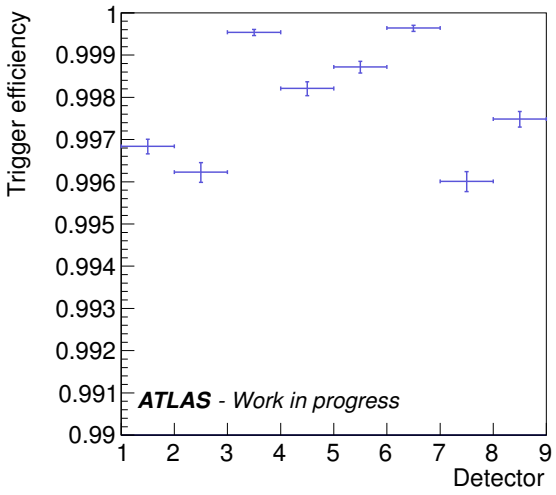

(d) Diffractice, MBTS2

Figure B.7: Efficiency of the triggering for diffractive like events, with binomial errors (everything is after all cuts)

B.5 Fiber hit multiplicity for one trigger only

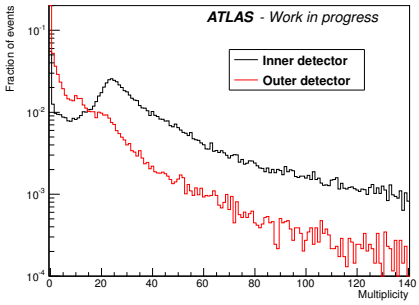

(a) Armlet 13

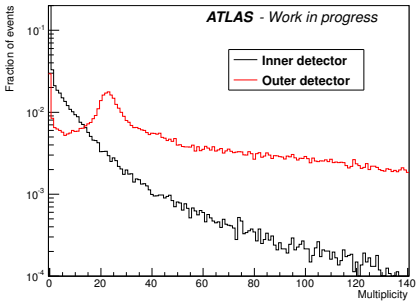

(b) Armlet 13

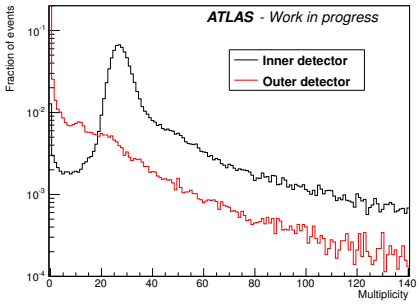

(c) Armlet 24

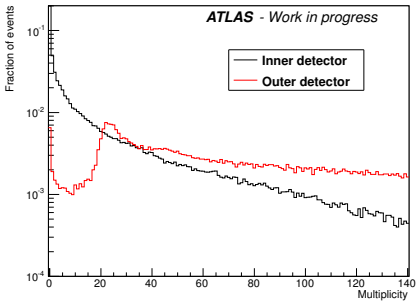

(d) Armlet 24

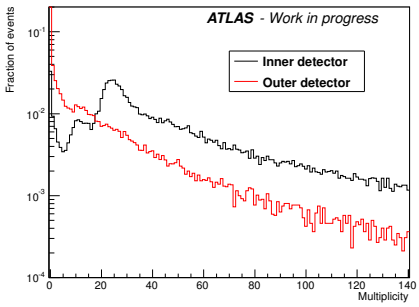

(e) Armlet 57

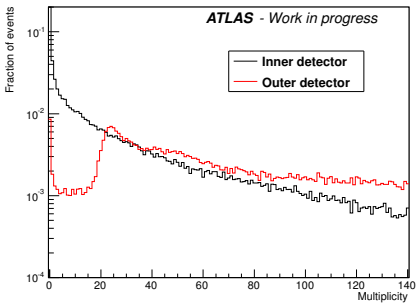

(f) Armlet 57

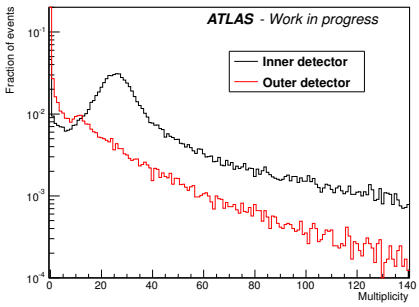

(g) Armlet 68

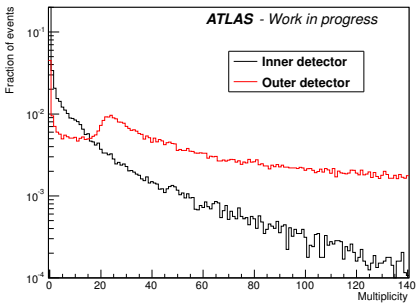

(h) Armlet 68

Figure B.8: Fiber hit multiplicities presented for the inner and outer detector with (left) trigger in inner, and no trigger in outer detector and (right) vice versa.

B.6 Hit multiplicity for a good track in the corresponding detector

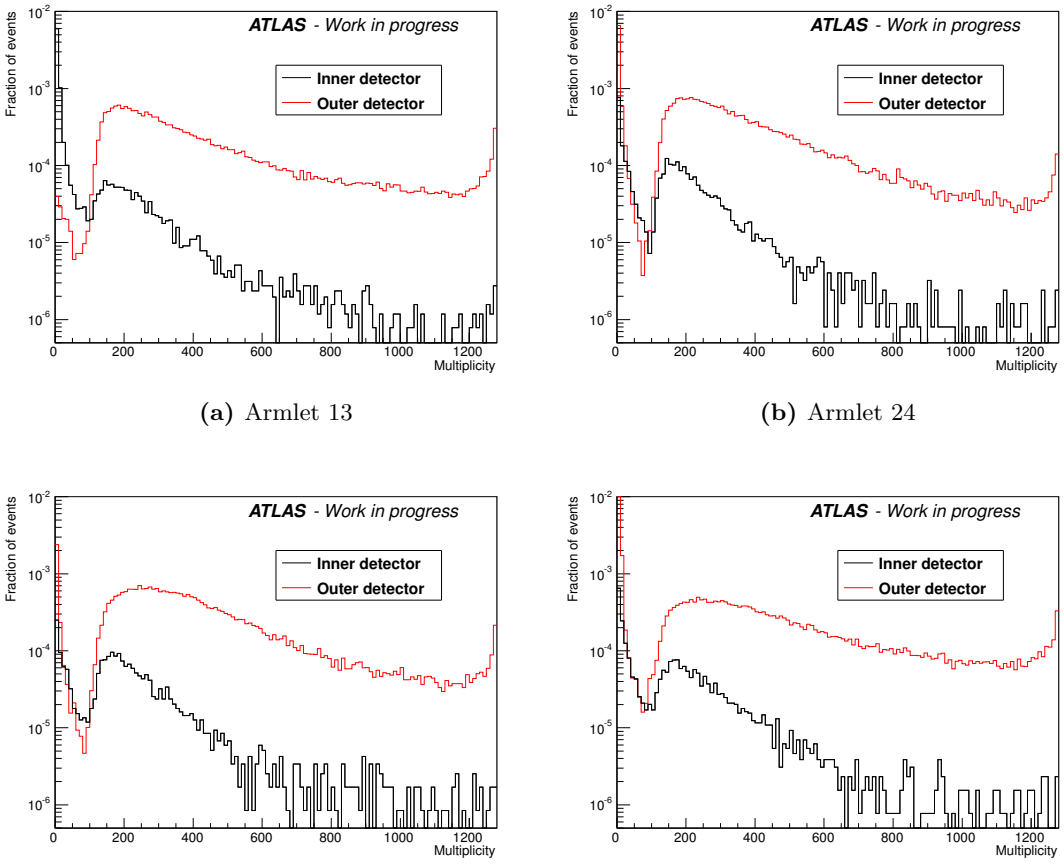

(a) Armlet 13

(b) Armlet 24

(c) Armlet 57

(d) Armlet 68

Figure B.9: Fiber hit multiplicity for the outer detector, when there was one well reconstructed track in the inner detector and vice versa.

B.7 Fits of secondaries

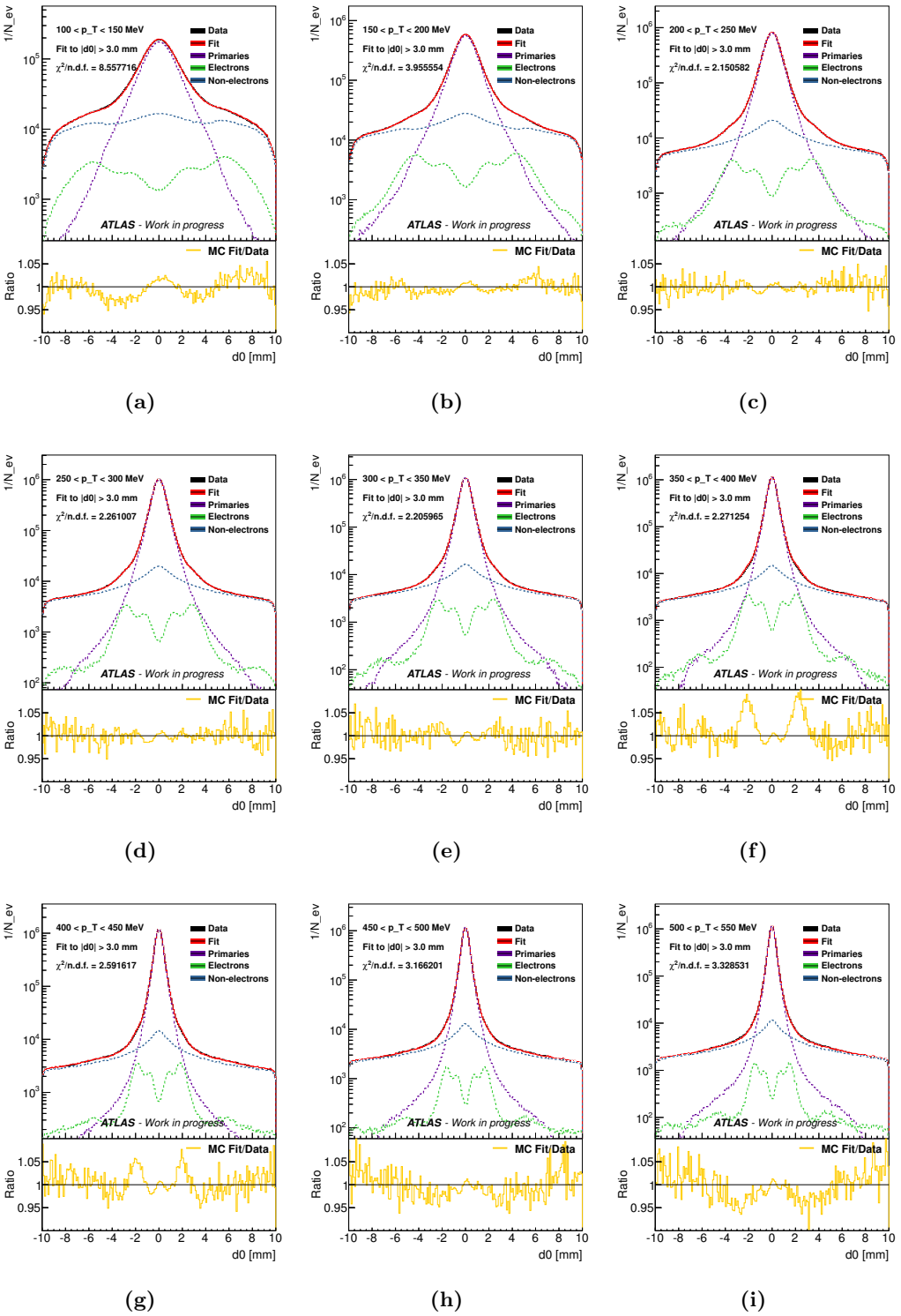

Figure B.10: Distributions in d_0 for various intervals of p_T.

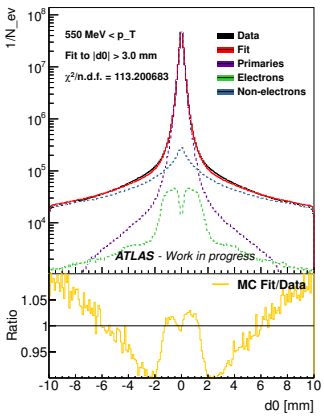

(a)

Figure B.11: Distributions in d_0 for various intervals of p_T.

B.8 Influence of beam background on secondaries

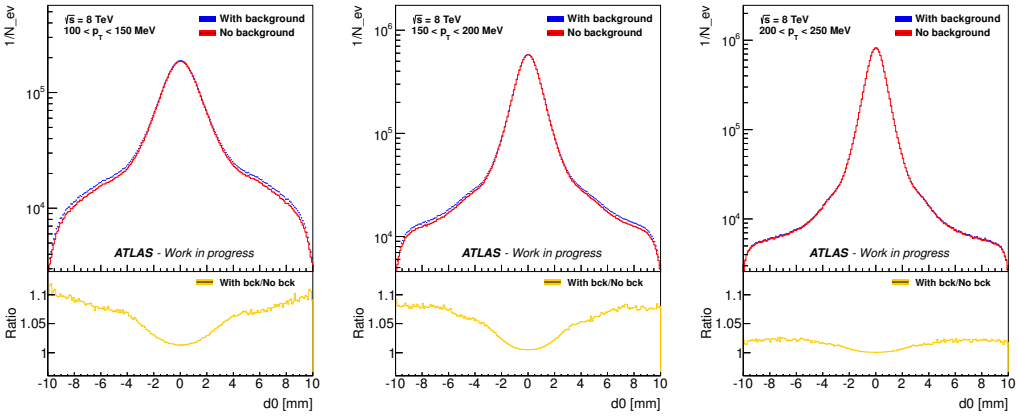

(a)

(b)

(c)

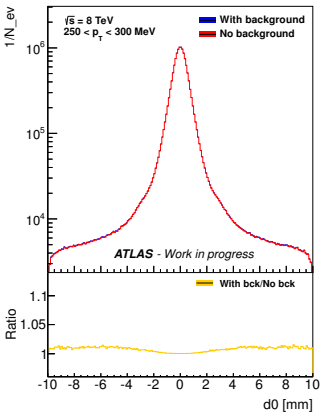

(d)

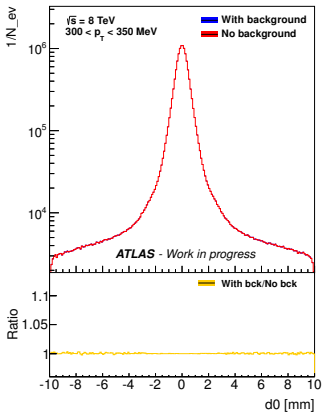

(e)

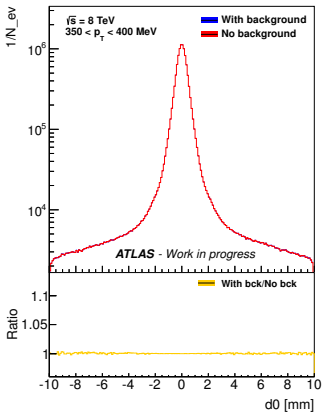

(f)

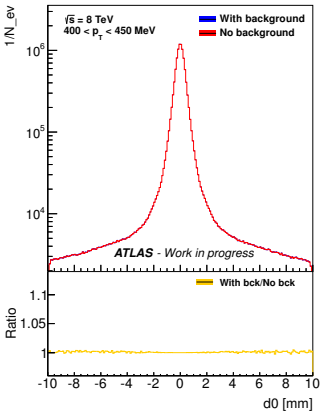

(g)

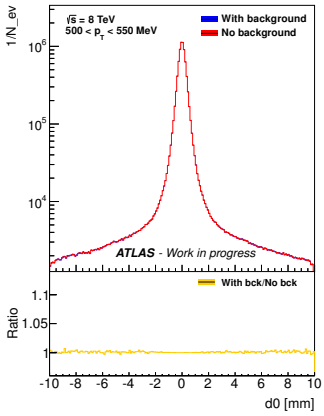

(h)

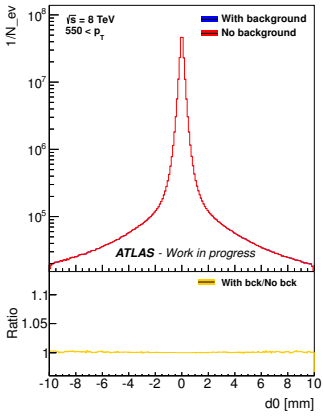

(i)

Figure B.12: Distributions in d_0 for various intervals of p_T.

B.9 Looking for correlations in background events

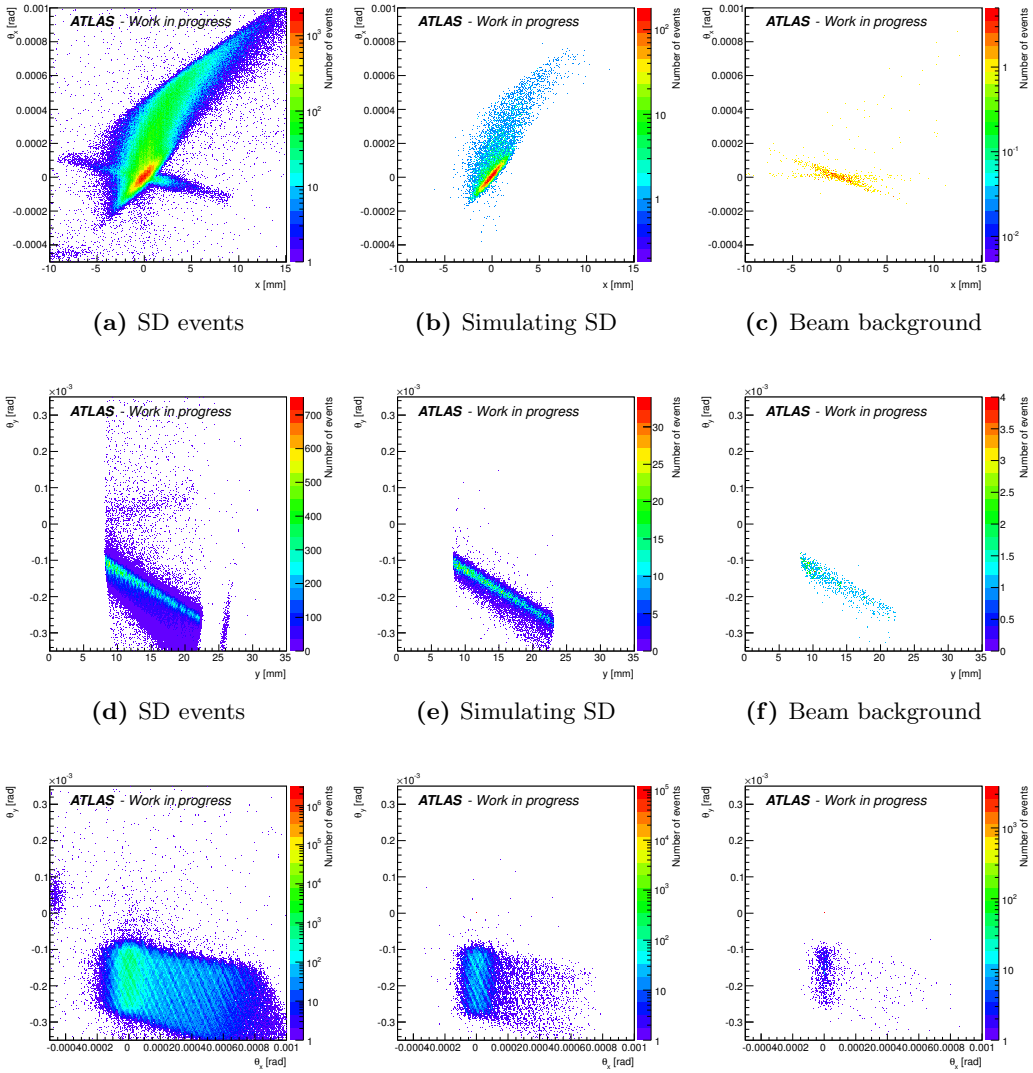

(a) SD events (b) Simulating SD (c) Beam background

(d) SD events (e) Simulating SD (f) Beam background

(g) SD events (h) Simulating SD (i) Beam background

Figure B.13: Different distributions plotted in search for corellations.

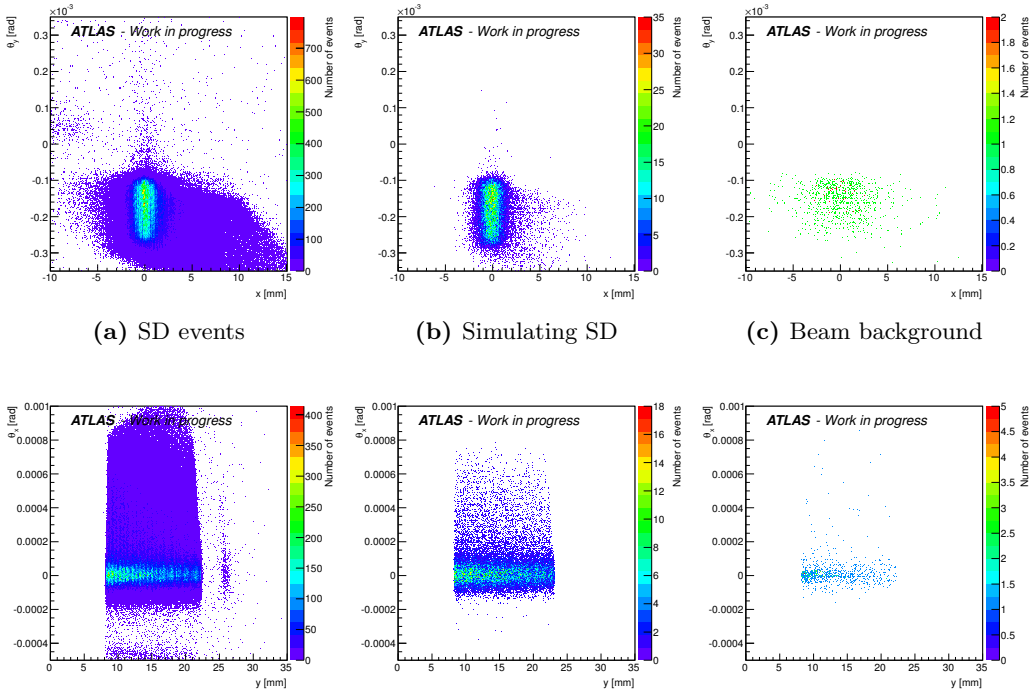

(a) SD events **(b)** Simulating SD **(c)** Beam background

(d) SD events **(e)** Simulating SD **(f)** Beam background

Figure B.14: Different distributions plotted in search for corellations.

B.10 Signed distribution of central diffractive events

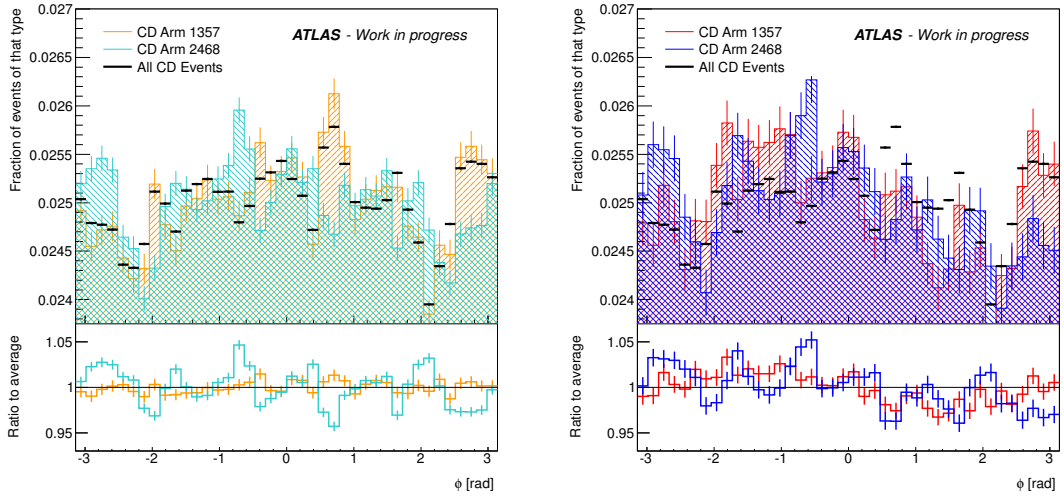

(a) **(b)**

Figure B.15: Distribution in ϕ for the charged tracks in central diffractive like events comparing **(a)** CD 1368 and CD 2457 or **(b)** CD 1357 and CD 2468, to the average distribution of selected central diffractive events, where the distributions has been multiplied with the sign on z of the surviving proton.

C

Datasets

ALFA performance studies

Private ALFA Ntuples derived from the RAW datasets ($< \mu > \sim 0.03$):
`data11_7TeV.00191373.calibration_ALFACalib.daq.RAW`
`data11_7TeV.00191373.physics_ALFA.merge.RAW`

Diffraction analysis

Respectively $\langle\mu\rangle \sim 0.072$ (< 0.0861), 0.065 (< 0.067) and 0.062 (< 0.0641):
`data12_8TeV.00206881.physics_ALFA.NTUP_MINBIAS_BS`
`data12_8TeV.00206884.physics_ALFA.NTUP_MINBIAS_BS`
`data12_8TeV.00206885.physics_ALFA.NTUP_MINBIAS_BS`

Minimum Bias Analysis

8 TeV dataset with low $\langle\mu\rangle \sim 0.035$ (< 0.040):
Initial configuration: `data12_8TeV.00200805.physics_MinBias.merge.NTUP_MINBIAS.f432_m1109`
Final configuration: `data12_8TeV.00200805.physics_MinBias.merge.NTUP_MINBIAS.r4768`

8 TeV MC samples for comparison (with initial confugration):
`mc12_8TeV.119997.Pythia8_A2MSTW2008LO_minbias_ND.recon.NTUP_MINBIAS.e1119_s1468_s1470_r3713`
`mc12_8TeV.119998.Pythia8_A2MSTW2008LO_minbias_SD.recon.NTUP_MINBIAS.e1119_s1468_s1470_r3713`
`mc12_8TeV.119999.Pythia8_A2MSTW2008LO_minbias_DD.recon.NTUP_MINBIAS.e1119_s1468_s1470_r3713`
`mc12_8TeV.129073.Pythia_AMBT2BCTEQ6L1_minbias_ND.recon.NTUP_MINBIAS.e1122_s1468_s1470_r3713`
`mc12_8TeV.129074.Pythia_AMBT2BCTEQ6L1_minbias_SD.recon.NTUP_MINBIAS.e1122_s1468_s1470_r3713`
`mc12_8TeV.129075.Pythia_AMBT2BCTEQ6L1_minbias_DD.recon.NTUP_MINBIAS.e1122_s1468_s1470_r3713`
`mc12_8TeV.129080.Epos_minbias_inelastic.recon.NTUP_MINBIAS.e1256_s1469_s1470_r3713`

8 TeV MC test sample for comparison (changed geometry):
`mc12_valid.119997.Pythia8_A2MSTW2008LO_minbias_ND.recon.NTUP_MINBIAS.e1119_s1725_s1732_r4780`

List of Figures

List of Tables

Bibliography

[1] David Griffiths. *Introduction to Elementary Particles*. Wiley-VCH Verlag GmbH & Co., 2008.

[2] An update of combined measurements of the new higgs-like boson with high mass resolution channels. Technical Report ATLAS-CONF-2012-170, CERN, Geneva, Dec 2012.

[3] Wikipedia, Visited 2013.

[4] Michael E. Peskin and Daniel V. Schroeder. *An Introduction to Quantum Field Theory*. Westview Press, 1951.

[5] Jens Lyng Petersen. *Elementarpartikelfysik*. Niels Bohr Institutet, 1994.

[6] Mark Srednicki. *Quantum Field Theory*. Cambridge University Press, 2010.

[7] Jan Ambjørn and Jens Lyng Petersen. *Quantum Field Theory*. The Niels Bohr Institute, 1999.

[8] B. R. Martin and G. Shaw. *Particle Physics*. John Wiley and Sons, Ltd, third edition, 2009.

[9] John C. Collins, Davison E. Soper, and George F. Sterman. Factorization of Hard Processes in QCD. *Adv.Ser.Direct.High Energy Phys.*, 5:1–91, 1988.

[10] Vincenzo Barone and Enrico Predazzi. *High Energy Particle Diffraction*. Springer-Verlag Berlin Heidelberg New York, 2002.

[11] J. R. Cudell, V. V. Ezhela, P. Gauron, K. Kang, Yu. V. Kuyanov, S. B. Lugovsky, E. Martynov, B. Nicolescu, E. A. Razuvaev, and N. P. Tkachenko. Benchmarks for the Forward Observables at RHIC, the Tevatron-Run II, and the LHC. *Phys. Rev. Lett.*, 89:201801, Oct 2002.

[12] ALFA Group. Measurement of the total cross section in pp collisions at $\sqrt{s} = 7$ TeV from elastic scattering with the ATLAS detector (Work in progress). *ATLAS Unpublished document*, 2013.

[13] The TOTEM Collaboration. First measurement of the total proton-proton cross-section at the LHC energy of $\sqrt{s} = 7$ TeV. *EPL (Europhysics Letters)*, 96(2):21002, 2011.

[14] G et. al. Antchev. Measurement of proton-proton elastic scattering and total cross-section at $\sqrt{s} = 7$ TeV. Technical Report TOTEM-2012-002. CERN-PH-EP-2012-239, CERN, Geneva, Aug 2012.

[15] G et. al. Antchev. Luminosity-independent measurements of total, elastic and inelastic cross-sections at $\sqrt{s} = 7$ TeV. Technical Report TOTEM-2012-004. CERN-PH-EP-2012-353, CERN, Geneva, Nov 2012.

[16] P. D. B. Collins. *An Introduction to Regge Theory & High Energy Physics*. Cambridge University Press, 1977.

[17] Sandy Donnachie, Gunter Dosch, Peter Landshoff, and Otto Nachtmnn. *Pomeron Physics and QCD*. Cambridge University Press, 2002.

[18] Ken F. Riley, Michael P. Hobson, and Stephen J. Bence. *Mathematical Methods for physics and Engineering*. Cambridge University Press, 2007.

[19] V.A. Petrov. Nonlinear Regge Trajectories in Theory and Practice. *AIP Conf.Proc.*, 1105:266–269, 2009.

[20] P. V. R. G. Silva and M. J. Menon. An updated analysis on the rise of the hadronic total cross-section at the lhc energy region. *International Journal of Modern Physics A*, 28(20):1350099, 2013.

[21] A. Donnachie and P.V. Landshoff. Total cross sections. *Physics Letters B*, 296(1-2):227 – 232, 1992.

[22] K. Kang, J.R. Cudell, V.V. Ezhela, S.B. Lugovsky, and N.P. Tkachenko. Soft pomeron and lower trajectory intercepts. pages 62–75, 1998.

[23] R.J.M. Covolan, J. Montanha, and K. Goulianos. A new determination of the soft pomeron intercept. *Physics Letters B*, 389(1):176 – 180, 1996.

[24] K.A. Ter-Martirosian. Froissart Type Rise of Cross-Sections and Predictions for Spectra and Multiplicities of Hadrons at Future Accelerators. *Sov.J.Nucl.Phys.*, 44:817, 1986.

[25] Christoffer Flensburg and Gösta Gustafson. Fluctuations, saturation, and diffractive excitation in high energy collisions. *Journal of High Energy Physics*, 2010(10):1–23, 2010.

[26] E. Gotsman, E. Levin, U. Maor, and J.S. Miller. A QCD motivated model for soft interactions at high energies. *The European Physical Journal C*, 57(4):689–709, 2008.

[27] F. E. Low. Model of the bare Pomeron. *Phys. Rev. D*, 12:163–173, Jul 1975.

[28] S. Nussinov. Colored-Quark Version of Some Hadronic Puzzles. *Phys. Rev. Lett.*, 34:1286–1289, May 1975.

[29] V.S. Fadin, E.A. Kuraev, and L.N. Lipatov. On the pomeranchuk singularity in asymptotically free theories. *Physics Letters B*, 60(1):50 – 52, 1975.

[30] Gordon Fraser. Roman pots for the LHC. *CERN Courier*, 238(3), 1999.

[31] S. Abatzis et. al. Observation of a narrow scalar meson at 1450 MeV in the reaction $pp \to p\, f(\pi^+\pi^-\pi^+\pi^-)p$ at 450 GeV/c using the CERN Omega spectrometer. *Physics Letters B*, 324(3-4):509 – 514, 1994.

[32] P.V. Landshoff. The Two Pomerons. 1994.

[33] Alexander Austregesilo and Tobias Schlueter. Partial-Wave Analysis of the Centrally Produced $\pi^+\pi^-$ System in pp Reactions at COMPASS. *PoS*, QNP2012:098, 2012.

[34] Fermilab. Found on their homepage. Exact location could not be restored., Visited 2013.

[35] M. L. Good and W. D. Walker. Diffraction Dissociation of Beam Particles. *Phys. Rev.*, 120:1857–1860, Dec 1960.

[36] W.-M. et.al Yao. Review of Particle Physics. *Journal of Physics G*, 33:1+, 2006.

[37] G. Aad and other. Rapidity gap cross sections measured with the ATLAS detector in pp collisions at $\sqrt{s} = 7$ TeV. *The European Physical Journal C*, 72(3), 2012.

[38] M.G. Albrow, A. Bagchus, D.P. Barber, P. Benz, A. Bogaerts, B. Bŏsnjaković, J.R. Brooks, C.Y. Chang, A.B. Clegg, F.C. Erné, C.N.P. Gee, P. Kooijman, D.H. Locke, F.K. Loebinger, N.A. McCubbin, P.G. Murphy, D. Radojičić, A. Rudge, J.C. Sens, A.L. Sessoms, J. Singh, D. Stork, and J. Timmer. Inelastic diffractive scattering at the CERN ISR . *Nuclear Physics B*, 108(1):1 – 29, 1976.

[39] W Kienzle, M Bozzo, M Buénerd, Y Muraki, J Bourotte, Maurice Haguenauer, G Sanguinetti, Giorgio Matthiae, A Faus-Golfe, and J Velasco. *Total cross section: elastic scattering and diffraction dissociation at the LHC*. Letter of Intent. CERN, Geneva, 1997.

[40] F. et. al. Abe. Measurement of pp single diffraction dissociation at $\sqrt{s} = 546$ and 1800 GeV. *Phys. Rev. D*, 50:5535–5549, Nov 1994.

[41] D. Bernard, M. Bozzo, P.L. Braccini, F. Carbonara, R. Castaldi, F. Cervelli, G. Chiefari, E. Drago, M. Haguenauer, V. Innocente, P. Kluit, B. Koene, S. Lanzano, G. Matthiae, L. Merola, M. Napolitano, V. Palladino, G. Sanguinetti, P. Scampoli, S. Scapellato, G. Sciacca, G. Sette, R. Van Swol, J. Timmermans, C. Vannini, J. Velasco, P.G. Verdini, and F. Visco. The cross section of diffraction dissociation at the cern SPS collider. *Physics Letters B*, 186(2):227 – 232, 1987.

[42] K. Goulianos. Renormalization of hadronic diffraction and the structure of the pomeron. *Physics Letters B*, 358(3-4):379 – 388, 1995.

[43] A. Brandt, S. Erhan, A. Kuzucu, D. Lynn, M. Medinnis, N. Ozdes, P.E. Schlein, M.T. Zeyrek, J.G. Zweizig, J.B. Cheze, and J. Zsembery. Measurements of single diffraction at âĹŽs = 630 GeV; Evidence for a non-linear $\alpha(t)$ of the pomeron. *Nuclear Physics B*, 514(1-2):3 – 44, 1998.

[44] Torbjörn Sjöstrand and Stephen Mrenna and Peter Skands. PYTHIA 6.4 physics and manual. *Journal of High Energy Physics*, 2006(05):026, 2006.

[45] Torbjörn Sjöstrand, Stephen Mrenna, and Peter Skands. A brief introduction to {PYTHIA} 8.1 . *Computer Physics Communications*, 178(11):852 – 867, 2008.

[46] Oliver Sim Brüning, Paul Collier, P Lebrun, Stephen Myers, Ranko Ostojic, John Poole, and Paul Proudlock. *LHC Design Report*. CERN, Geneva, 2004.

[47] Xabier Cid Vidal and Ramon Cid. Taking a closer look at LHC. `http://www.lhc-closer.es`, Visited 2013.

[48] The CMS Collaboration, S Chatrchyan, and et. al. The CMS experiment at the CERN LHC. *Journal of Instrumentation*, 3(08):S08004, 2008.

[49] Jiri Chyla. Edited from version on homepage., Published 2010.

[50] C Lefevre. LHC: the guide (English version). Guide du LHC (version anglaise). Feb 2009.

[51] J Rossbach and P Schmüser. Basic course on accelerator optics. `http://adweb.desy.de/~rossbach/uni/Cern.pdf`.

[52] Simon Stark Mortensen. Kinematic reconstruction of diffractive processes. Master thesis, University of Copenhagen, August 2013.

[53] H Burkhardt and P Grafström. Absolute Luminosity from Machine Parameters. Technical Report LHC-PROJECT-Report-1019. CERN-LHC-PROJECT-Report-1019, 2007.

[54] ATLAS Collaboration. Improved luminosity determination in pp collisions at $\sqrt{s} =$ 7 TeV using the ATLAS detector at the LHC. *ArXiv e-prints*, February 2013.

[55] C Barschel, M Ferro-Luzzi, J-J Gras, M Ludwig, P Odier, and S Thoulet. Results of the LHC DCCT Calibration Studies. Feb 2012.

[56] S van der Meer. Calibration of the effective beam height in the ISR. Technical Report CERN-ISR-PO-68-31. ISR-PO-68-31, CERN, Geneva, 1968.

[57] Georges Aad et al. Luminosity Determination in *pp* Collisions at $\sqrt{s} = 7$ TeV Using the ATLAS Detector at the LHC. *Eur.Phys.J.*, C71:1630, 2011.

[58] ATLAS Collaboration. Twiki page on ATLAS Public Luminosity results. `twiki.cern.ch/twiki/bin/view/AtlasPublic/LuminosityPublicResults`, Visited 2013.

[59] The ATLAS Collaboration and G Aad and et. al. The ATLAS Experiment at the CERN Large Hadron Collider. *Journal of Instrumentation*, 3(08):S08003, 2008.

[60] Dan Green. *High p_T physics at hadron colliders*. Cambridge University Press, 2004.

[61] Sabine Elles. New geometry description of Inner PP0 region. Inner Detector Material Working Group Internal meeting, May 31st 2013. `https://indico.cern.ch/conferenceDisplay.py?confId=254576`.

[62] Claus Grupen and Boris Shwartz. *Particle Detectors*. Cambridge University Press, 2008.

[63] Richard Fernow. *Introduction to exprimental particle physics*. Cambridge University Press, 1986.

[64] Stefaan Tavernier. *Experiemental Techniques in Nuclear and Particle physics*. Springer, 2010.

[65] Walter Heitler. *The Quantum Theory of Radiation*. Dover, 1954.

[66] T.A. Gabriel and W. Schmidt. Calculated performance of iron-argon and iron-plastic calorimeters for incident hadrons with energies of 5 to 75 GeV . *Nuclear Instruments and Methods*, 134(2):271 – 283, 1976.

[67] H. Stenzel. The ATLAS Forward Detectors Past, Present and Future. Presented at Vienna Conference on Instrumentation, February 13th 2013. `https://indico.cern.ch/conferenceDisplay.py?confId=186337`.

[68] Sune Jakobsen. Private communication with ALFA Run Coordinator. Can be presented upon request., 2013.

[69] E Feng and J E Pilcher. Triggering ATLAS with Minimum Bias Trigger Scintillators. Technical Report ATL-TILECAL-INT-2007-004. ATL-COM-TILECAL-2007-013, CERN, Geneva, May 2007.

[70] Regina Esther Kwee, N Ellis, and H Kolanoski. *Development and Deployment of an Inner Detector Minimum Bias Trigger and Analysis of Minimum Bias Data of the ATLAS Experiment at the Large Hadron Collider*. PhD thesis, Humboldt U., Berlin, Sep 2011. Presented 13 Jan 2012.

[71] Klaus Werner, Fu-Ming Liu, and Tanguy Pierog. Parton ladder splitting and the rapidity dependence of transverse momentum spectra in deuteron-gold collisions at RHIC. *Phys.Rev.*, C74:044902, 2006.

[72] S. Agostinelli et. al. Geant4 - a simulation toolkit . *Nuclear Instruments and Methods in Physics Research Section A: Accelerators, Spectrometers, Detectors and Associated Equipment*, 506(3):250 – 303, 2003.

[73] Peter Jenni and et. al. *ATLAS Forward Detectors for Measurement of Elastic Scattering and Luminosity*. Technical Design Report. CERN, Geneva, 2008.

[74] Various speakers. ALFA readiness review. Internal meeting, August 13th 2009. `https://indico.cern.ch/conferenceDisplay.py?confId=62776`.

[75] S. Ask and et. al. Luminosity measurement at ATLAS - Development, construction and test of scintillating fibre prototype detectors. *Nuclear Instruments and Methods in Physics Research Section A: Accelerators, Spectrometers, Detectors and Associated Equipment*, 568(2):588 – 600, 2006.

[76] F. Anghinolfi and et. al. Hadron beam test of a scintillating fibre tracker system for elastic scattering and luminosity measurement in ATLAS. *Journal of Instrumentation*, 2(07):P07004, 2007.

[77] Allongue B. and et. at. Test Beam 2008: First Measurements with an ALFA Roman Pot Prototype. Technical Report ATL-LUM-INT-2010-001, CERN, Geneva, Jan 2010.

[78] Sune Jakobsen. Performance evaluation and optimization of the luminosity detector ALFA. master thesis, University of Copenhagen, 2010. On CDS.

[79] Sune Jakobsen. *(Work in progress)*. Doctoral thesis, CERN, 2013.

[80] R. Battiston and et. al. The "Roman pot" spectrometer and the vertex detector of experiment UA4 at the CERN SPS collider. *Nuclear Inst. and Methods in Physics Research, A*, 238(1):35–44, 1985.

[81] U. Amaldi and et. al. The real part of the forward proton proton scattering amplitude measured at the CERN intersecting storage rings. *Physics Letters B*, 66(4):390 – 394, 1977.

[82] C. Joram, H. Stenzel, and Andre Braem. Basic Considerations on the Overlap Detectors of the ATLAS ALFA system. Technical Report ATL-LUM-PUB-2007-002. ATL-COM-LUM-2006-009. CERN-ATL-LUM-PUB-2007-002, CERN, Geneva, Jun 2006.

[83] Andre Braem and et. al. Trigger counter studies for the ALFA detector. Technical Report ATL-LUM-PUB-2009-001. ATL-COM-LUM-2009-005, CERN, Geneva, March 2009.

[84] Sune Jakobsen. ALFA trigger in 2011. Technical Report ATL-COM-LUM-2012-016, CERN, Geneva, Dec 2012.

[85] Sune Jakobsen. ALFA technical activity in LS1. Presented at internal NBI group meeting, August 20th 2013. `https://indico.cern.ch/conferenceDisplay.py?confId=266041`.

[86] ATLAS Run Queries. `http://atlas-runquery.cern.ch`, Visited 2012-13.

[87] P. Hamal. Events losses in 191373. Presented at internal ALFA Physics meeting, June 19th 2013. `https://indico.cern.ch/conferenceDisplay.py?confId=250998`.

[88] Kristof Kreutzfeldt. Elastic reconstruction efficiency in ALFA. Presented at internal Soft-QCD group meeting, June 24th 2013. `https://indico.cern.ch/conferenceDisplay.py?confId=254353`.

[89] K.-H. Hiller. An attempt to understand the rates of losses and backgrounds. Presented at internal ALFA Physics meeting, May 16th 2012. `https://indico.cern.ch/conferenceDisplay.py?confId=169950`.

[90] PDG Homepage on material properties. `http://pdg.lbl.gov/2010/AtomicNuclearProperties/`, Visited 2013.

[91] Kuraray official specifications of plastic scintillators. `http://kuraraypsf.jp/psf/index.html`, Visited 2013.

[92] The ATLAS Collaboration. Charged-particle multiplicities in pp interactions measured with the ATLAS detector at the LHC. *New Journal of Physics*, 13(5):053033, 2011.

[93] Simone Pagan Griso. Private communication with minimum bias working group vertex expert, 2013. Can be presented upon request.

[94] G Aad, P Behera, W H Bell, U Bitenc, G Brandt, T Eifert, H M Gray, J Katzy, A Kastanas, M Kayl, O Kepka, T Kuhl, R Kwee, M Leyton, M Limper, A Lister, R Meera-Lebbai, S Nektarijevi, E Nurse, K Rosbach, A Salzburger, M Warsinsky, and R Zaidan. Track Reconstruction Efficiency in sqrt(s)=7 TeV Data for Tracks with $p_T > 100$ MeV. Technical Report ATL-PHYS-INT-2011-001, CERN, Geneva, Jan 2011.

[95] G. D'Agostini. A multidimensional unfolding method based on Bayes' theorem . *Nuclear Instruments and Methods in Physics Research Section A: Accelerators, Spectrometers, Detectors and Associated Equipment*, 362(2-3):487 – 498, 1995.

[96] HM Gray, G Gorfine, M Limper, and A Salzburger. Using the SCT Extension Efficiency to Probe Material between the Pixel Detector and the SCT. Technical Report ATL-COM-PHYS-2010-100, CERN, Geneva, Feb 2010. this is a backup note for the published MB 1.0 analysis.

[97] A Andreazza, J Boyd, G Brandt, K Grimm, D Kar, O Kepka, P Loch, W Lukas, J Monk, S Pagan Griso, A Pilkington, A Salzburger, E Sarkisyan-Grinbaum, and K Wozniak. Validation of MBTS trigger performance and low-pT tracking performance in low-luminosity 8 TeV data. Technical Report ATL-COM-INDET-2012-052, CERN, Geneva, Jul 2012.

[98] S. P. Griso. Beam background studies. Presented at internal Minimum Bias Analysis meeting, February 8th 2013. `https://indico.cern.ch/conferenceDisplay.py?confId=227319`.

[99] Max Baak. Good run lists, what about them? *ATLAS e-News*, 2010.

[100] ALTAS DQ experts. Private communication with atlas dq experts, 2013. Can be presented upon request.

[101] Hasko Stenzel. Private communication with alfa luminosity block expert, 2013. Can be presented upon request.

[102] ALFA Data runs, internal document, available request. `https://twiki.cern.ch/twiki/bin/viewauth/Atlas/AlfaDataRuns`, Updated regularly, used 2013.

[103] TriggerRatesFromCool, Twiki pages, Visited 2013.

[104] M. Bozzo, P.L. Braccini, F. Carbonara, R. Carrara, R. Castaldi, F. Cervelli, G. Chiefari, E. Drago, M. Haguenauer, B. Koene, G. Matthiae, L. Merola, M. Napolitano, V. Palladino, G. Sanguinetti, G. Sciacca, G. Sette, R. van Swol, J. Timmermans, C. Vannini, J. Velasco, and F. Visco. Single diffraction dissociation at the CERN SPS collider. *Physics Letters B*, 136(3):217 – 220, 1984.

[105] O Kepka, C Royon, M Saimpert, and R Zlebcik. Multiple proton-proton interactions in Atlas Forward Detector pp at $\sqrt{s} = 14$ TeV. Technical Report ATL-COM-PHYS-2013-847, CERN, Geneva, Jun 2013.

[106] Skaarup, Mikkel. Diffractive analysis with 8TeV - short update. ATLAS Diffraction analysis meeting, 1 July 2013. `https://indico.cern.ch/conferenceDisplay.py?confId=260306`.

[107] H. Stenzel. Beam Background. Presented at internal AFP Collaoration meeting, June 18th 2013. `https://indico.cern.ch/conferenceDisplay.py?confId=254488`.